Title

Deep Learning Image Synthesis for MRI: From Super-Resolution to Cardiovascular Biomechanics

Author

Masutani, Evan Masataka

Publication Date

2022

UNIVERSITY OF CALIFORNIA SAN DIEGO

Deep Learning Image Synthesis for MRI: From Super-Resolution to Cardiovascular Biomechanics

A dissertation submitted in partial satisfaction of the
requirements for the degree
Doctor of Philosophy

in

Bioengineering

by

Evan Masataka Masutani

Committee in charge:

Professor Albert Hsiao, Chair
Professor Adam Engler, Co-Chair
Professor Francisco Contijoch
Professor Thomas Liu
Professor Andrew McCulloch

2022

The dissertation of Evan Masataka Masutani is approved, and it is acceptable in quality and form for publication on microfilm and electronically.

University of California San Diego
2022

DEDICATION

I dedicate this dissertation to my family, friends, and mentors who have all graciously supported me throughout this journey.

Mom and Dad, thank you for raising me and making this all possible. I will dedicate myself to improving the health and happiness of our society.

Dad, it's been a long, tough road—but we made it! Thank you for holding on for this long. I hope I'll continue to make you proud.

Hana, my love and my life, my future wife, thank you for loving me throughout this turbulent time. I love you.

TABLE OF CONTENTS

LIST OF FIGURES

LIST OF TABLES

LIST OF SUPPLEMENTAL VIDEOS

Supplemental Video 1: Multi-chamber Segmentation Over the Cardiac Cycle

Supplemental Video 2: Intracardiac Blood Flow Field Synthesis in a Morphologically-Normal Patient

Supplemental Video 3: Intracardiac Blood Flow Field Synthesis in a Patient with Hypertrophic Obstructive Cardiomyopathy

Supplemental Video 4: Overview of the deep learning synthetic strain (DLSS) approach

Supplemental Video 5: Exemplar case of a patient with catheter angiogram-proven LAD occlusion

Supplemental Video 6: Patient with cardiac arrest 4 months prior with viral prodrome and presumed myocarditis with negative myocardial biopsy

Supplemental Video 7: Ventricular dyssynchrony with dissociation of contraction of the septal and lateral walls due to left bundle branch block, visualized and quantified with DLSS

ACKNOWLEDGEMENTS

I would like to acknowledge my truly wonderful mentors and co-authors, without whom none of this work would be possible. Thank you, Dr. Albert Hsiao and Dr. Adam Engler, for being exceptional co-mentors throughout this learning process. Thank you, Dr. Tara Retson, Dr. Brian Hurt, Dr. Kevin Blansit, and Dr. Naeim Bahrami for being wonderful people, insightful lab-mates, and good friends.

I would also like to gratefully thank the NVIDIA Corporation for graciously donating a Titan Xp GPU, which enabled me to build the technical foundation necessary to pursue this project. I am also deeply grateful to the San Diego Supercomputer Center, Microsoft, and Oracle for providing me with invaluable GPU-accelerated compute credits. I would also like to thank the National Institute of General Medical Sciences, the National Heart, Lung, and Blood Institute, the American Heart Association, and the Radiological Society of North America for their very generous grant support. Finally, I would like to acknowledge the UC San Diego Medical Scientist Training Program, the UC San Diego Department of Bioengineering, the UC San Diego Department of Radiology, and the UC San Diego School of Medicine for their unwavering support. Thank you all!

Chapter 2, in part, is a reprint as it appears in Radiology (2020). The author list is: Masutani, Evan; Bahrami, Naeim; Hsiao, Albert. The dissertation author was the primary investigator and author of this paper.

Chapter 3, in part, is a reprint as it appears in Radiology (2021). The author list is: You, Sophie*; Masutani, Evan*; Alley, Marcus; Vasanawala, Shreyas; Taub, Pam; Liau, Joy; Roberts, Anne; Hsiao, Albert. *Denotes co-first authorship. The dissertation author was the co-first investigator and co-first author of this paper.

Chapter 4, in part, is in preparation for submission to Radiology: Artificial Intelligence. The author list is: Masutani, Evan; Retson, Tara; Hurt, Brian; Blansit, Kevin; Hsiao, Albert. The dissertation author was the primary investigator and author of this manuscript.

Chapter 5, in part, is in preparation for submission to Radiology. The author list is: Masutani, Evan; Chandrupatla, Rahul; Hahn, Lewis; Horowitz, Misha; Jacobs, Kathleen; Kligerman, Seth; Hsiao, Albert. The dissertation author was the primary investigator and author of this manuscript.

VITA

2014 — Stanford University
Bachelor of Science, Engineering: Bioengineering

2022 — University of California San Diego
Doctor of Philosophy, Bioengineering

ABSTRACT OF THE DISSERTATION

Deep Learning Image Synthesis for MRI:
From Super-Resolution to Cardiovascular Biomechanics

By

Evan Masataka Masutani

Doctor of Philosophy in Bioengineering

University of California San Diego, 2022

Professor Albert Hsiao, Chair

Professor Adam Engler, Co-Chair

Since its invention in the 1970s, magnetic resonance imaging (MRI) has contributed greatly to our understanding of the human body in health and disease. MRI images anatomy and physiology with high spatiotemporal resolution and without ionizing radiation. Due to these factors, MRI is particularly well suited to studying the heart, and cardiac MRI is considered the clinical gold-standard for assessment of cardiac morphology, flow, and function. However, interpretation of cardiac MRI is highly dependent on image quality and often requires extensive manual annotation and visual analysis.

Convolutional neural networks (CNNs), a form of deep learning and artificial intelligence, have potential to revolutionize medical imaging. Broadly, CNNs comprise a series of trainable weights called layers, which iteratively learn the features required to perform a given task. Currently, CNNs are being explored for a variety of computer vision tasks, such as classification, localization, and segmentation, but have untapped potential. Specifically, their ability to perform image synthesis is unknown.

Given these challenges in MRI and the untapped potential of CNNs, I asked: can we use deep learning to perform image synthesis for MRI? Using this question as the bedrock for my dissertation, I set out to solve progressively more challenging problems in cardiovascular MRI using CNNs, building towards the ultimate task of automatically quantifying cardiac function and biomechanics. In aim 1, I asked whether existing CNNs can enhance low-resolution cardiac images. That is, can CNNs perform image super-resolution of steady-state free precession (SSFP)? Specifically, I asked which CNN architectures are suitable for this task and how well they perform relative to conventional image upscaling methods.

In aim 2, I asked whether I could upgrade the CNN architectures from aim 1 to isolate and remove background signal from 4D Flow MRI. That is, can CNNs perform phase-error correction of 4D Flow MRI acquisitions via synthesis of the background static vector field? To achieve this, I asked what architectural modifications are necessary to infer these multi-component volumetric vector fields. I then compared CNN-based phase error correction with existing manual segmentation-based methods.

In aim 3, I asked whether I could further upgrade my phase-error correction CNN from aim 2 to predict intracardiac blood flow from videos of the beating heart. That is, can CNNs infer dynamic blood flow velocity fields from cardiac cine SSFP images? Specifically, I asked how I could incorporate spatiotemporal information and anatomical boundaries into this new architecture I call Triton-Net. I then measured the correlation between the synthesized flow fields and 4D Flow MRI measurements. Lastly, I asked whether I could use these flow values to detect left ventricular outflow obstruction.

Finally, in aim 4, I asked whether I could refine Triton-Net to evaluate local myocardial function. That is, could I add explicit physical constraints into Triton-Net to infer dynamic myocardial velocity and strain tensor fields from cardiac cine SSFP images? Realizing that myocardial contraction is periodic, I explored how I may encode net-zero displacement and strain constraints into the Triton-Net architecture, resulting in a heavily modified deep learning synthetic strain (DLSS) CNN. I then characterized DLSS strain in a healthy population and asked whether I could use DLSS strain to identify wall motion abnormalities in an ischemic heart disease population. Lastly, I compared DLSS classification performance against the consensus visual assessment of four cardiothoracic radiologist readers.

Chapter 1: Introduction

1.1 Background

1.1.1 Introduction to Cardiac MRI

Since its invention in the 1970s [1–3], magnetic resonance imaging (MRI) has contributed greatly to our understanding of the human body in health and disease. Broadly, MRI leverages the fact that certain isotopes, notably protons, have a net magnetic moment and can be forcefully aligned in the direction of a strong external magnetic field (B_0). Once aligned, the orientation of these protons can be transiently perturbed using a brief radiofrequency electromagnetic pulse. Receiver coils record the radiofrequency echoes of the perturbed protons as they asymptotically relax and re-align themselves to B_0. The kinetics of relaxation vary between substances and tissues and serve as a molecular fingerprint. Thus, we may generate informative images of anatomy based on snapshots of their signal intensity, where the brightness of each voxel is dependent on the relaxation times and proton density of its encapsulated tissue[4].

The prescribed strength and timing of the external magnetic fields and radiofrequency pulses are called pulse sequences; different pulse sequences emphasize different aspects of the anatomy or permit measurement of physiology. For example, the steady-state free precession (SSFP) pulse sequence forms the backbone of cardiac MRI, as it produces high-contrast images with bright blood and darker myocardial tissue which permit assessment of morphology and function[5]. More complex pulse sequences e.g., 2D Phase-Contrast MRI[6] and 4D Flow MRI[7], measure the blood velocity field. Additionally, one may acquire and interleave multiple images over the cardiac cycle to generate movies with high temporal resolution through cine imaging[8]. Thus, the ability of

MRI to measure different aspects of cardiac physiology with high spatiotemporal resolution makes it particularly well-suited for studying the heart.

1.1.2 Strengths of Cardiac MRI

Cardiac MRI is the clinical gold standard for non-invasively measuring cardiac morphology[9,10], flow[11,12], and function[13,14]. Cardiac MRI's strengths and abilities are illustrated in the examples of ischemic heart disease and congenital heart disease.

Ischemic heart disease, also known as coronary artery disease, is exceedingly common and affects over 18 million adults in the USA[15]. Anatomically, the right and left coronary arteries originate from the sinus of Valsalva and deliver oxygen-rich blood to the heart. The branches of the coronary arteries in turn are responsible for nourishing distinct territories of the myocardium; any interruptions to blood flow results in tissue ischemia and resulting loss of function. The most common underlying cause of coronary blockage is plaque formation due to atherosclerosis, where fatty, fibrotic material gradually accumulates within the vessel walls and pinch off blood flow[16,17]. Severe ischemia eventually leads to tissue necrosis, scar tissue formation, and complete loss of function[18].

Clinically relevant information entails: 1) whether there is ischemia and loss of function, 2) which regions of the heart are affected, and 3) how to therapeutically manage disease. Cardiac MRI can help answer all these questions. Short-axis cine SSFP stacks permit accurate quantification of ejection fraction to determine whether there is globally depressed function[10,19]. From these same images, clinicians visually assess myocardial thickening to determine whether there are local wall motion abnormalities indicative of ischemic disease[20]. To pinpoint which regions have reduced blood flow, physicians administer intravenous contrast agent, which increases local signal intensity, and note any persistently dark, and therefore ischemic, myocardial segments. This is known as perfusion imaging[21]. Finally, we ask what can be done to manage these patients? Coronary bypass grafts short-circuit sites of occlusion and re-perfuse viable myocardium; however, such invasive interventions are likely futile when there is no viable tissue to recover[22]. Cardiac MRI guides whether surgical intervention may be helpful through quantification of myocardial scar. In healthy tissue, contrast agent transiently passes through the microvasculature of the myocardium; however, it will linger in enlarged extracellular spaces, which result from tissue injury and scarring. Through a technique called myocardial delayed enhancement, clinicians may locate and quantify bright regions denoting myocardial scar; poor surgical outcomes are probable when scarring is >50% transmural extent[23]. Thus, cardiac MRI provides insight into determining, localizing, and prognosticating ischemic heart disease.

Cardiac MRI also informs the management of patients with congenital heart disease. For example, ventricular septal defects (VSD) is a relatively common congenital cardiac defect estimated to occur in 2829 per 1 million live births and involves a persistent communicating hole through the ventricular septum[24]. As with ischemic heart disease, clinicians may assess cardiac morphology using cine SSFP MRI and locate any septal defects. To determine physiological severity of these VSDs, radiologists can employ 4D Flow MRI[25]. Specifically, flow measurements are taken at the aorta (systemic flow, Q_s) and the pulmonary artery (pulmonary flow, Q_p) to determine the degree of left-to-right shunting. Surgical intervention i.e., myocardial patching, is considered when the Q_p/Q_s ratio is greater than 1.5[26].

1.1.3 Limitations of Cardiac MRI

Despite the utility of cardiac MRI, there are multiple hurdles involving data acquisition, post-processing, and analysis which limit its potential. Broadly, my dissertation aims to build and evaluate image processing methods to augment assessment of cardiac morphology, flow, and function.

Cine SSFP forms the backbone of cardiac imaging and is crucial for the assessment of *cardiac morphology* and left ventricular function. However, MRI suffers from long acquisition times[27], often requiring averaging across multiple heartbeats, and necessitates a trade-off among spatial resolution, temporal resolution, and scan time[28]. Additionally, longer breath holds are required with increasing spatial resolution, which may be intolerable for patients with severe pulmonary disease[29]. Radiologists are therefore forced to balance acquisition time with resolution to fit clinical needs, and certain applications such as real-time imaging may require small acquisition matrices[30].

4D Flow MRI contributes critical *flow and hemodynamic information* for the diagnosis and management of cardiac disease[31], and its applications are growing to include assessment of abdominal[32] and brain vasculature[33]. However, the rapidly changing external magnetic fields inherent to MRI give rise to eddy currents, which substantially contribute to background phase error in 4D Flow MRI. Correction of background phase error remains a challenge[34–37]. Partial phase error correction can be achieved using pre-emphases techniques[38], incorporation of gradient nonlinearity in the image reconstruction process[39], and field derivation and correction via Maxwell equations[40]; however, residual phase error may compromise the accuracy of 4D Flow measurements[36,41]. Further phase error correction is therefore required. Additionally, acquisition of 4D Flow MRI is a lengthy process, as velocity measurements in the x, y, and z directions must be measured individually[42]. Advanced technical expertise is also required, and thus 4D Flow is currently not widely available[43].

Lastly, visual assessment of *regional myocardial function* is considered the clinical gold standard, however it largely remains a subjective visual task by expert readers[13,20,44–46]. Strain, defined as the change in length over initial length, has been proposed as a quantitative alternative for visual assessment. Since the 1980s[47], dedicated strain imaging techniques, such as myocardial tagging[47], DENSE[48], SENC[49], and HARP[50], have been developed to yield granular measurements of regional myocardial function. Each of these however requires acquisition of a dedicated imaging sequence and considerable post-processing analysis. More recently, feature tracking strain methods have emerged as a method for retrospective analysis of strain from cine SSFP images[51,52], with multiple studies showing potential values of measurements of global strain. However, the published values of feature tracking-derived strain in normal subjects varies widely between studies and vendors[53] and show poor agreement with established strain imaging techniques[54,55].

1.1.4 Introduction to Convolutional Neural Networks

Convolutional neural networks (CNNs), a form of deep learning and artificial intelligence, have emerged as a powerful technology for the analysis of biomedical image data[56]. In the broadest sense, CNNs learn relevant features from input images to produce desired outputs. The building blocks of CNNs are convolutional layers, which comprise a set of filters, followed by an activation function. Each filter comprises a grid of learnable weights, which are convolved with the input image to yield an intermediate output[57,58]. These intermediate outputs are then passed into a differentiable non-linear activation function e.g., sigmoid function, which permits approximation of linear and non-linear functions[59,60]. The outputs of each convolutional layer are called feature maps and can be passed as inputs into successive convolutional layers.

CNN training is the process in which the weights of each convolutional filter iteratively update to generate more accurate predictions, and requires input images, affiliated labels, and a loss function. For example, let us assume we wish to train a CNN to segment the lungs on a radiograph i.e., assign a label of 1 to all lung pixels and 0 to all non-lung pixels. We assume we have a curated set of chest radiographs, where an expert has provided manual segmentations of the lungs. As we feed each input radiograph image into a given CNN (with randomly initiated weights), each successive convolutional layer generates feature maps, until a single output image is produced[61]. Most likely, the output will bear minimal resemblance to the manually segmented label image. The first step in the learning process is quantifying how incorrect a given prediction is, which is the role of the loss function. A simple, yet powerful, example loss function is the mean-squared error between predicted and label images[62]. The aim of training is thus to minimize the value of the loss function. Assuming a differential loss function, it is possible to calculate the gradient of the loss function with respect to all weights in the CNN via the chain-rule of calculus. Given an appropriate step-size, we can use the gradient to iteratively update each weight in the CNN to minimize the loss function and produce more accurate predictions[63].

Over the last several years, CNNs have proven valuable for automating multiple visual tasks in medical imaging and are progressively being integrated into clinical workflows. Multiple groups have shown that CNNs can approach radiologist-level performance for detection of COVID-19 from radiographs[64,65], ventricular segmentation[10,19], and landmark localization[62,66,67]. While there has been significant progress for these visual tasks, CNNs have untapped potential to extrapolate beyond structural identification. Specifically, the ability of CNNs to perform image synthesis i.e., generation of realistic pixelwise representations of physical phenomena such as displacement and velocity, remains unknown.

1.2 Outline of the Dissertation

Broadly, my dissertation sought to answer the question: can we use deep learning to perform image synthesis for MRI? In stepwise fashion, I iteratively refined novel CNN architectures to accomplish more complex visual tasks and build the tools and expertise necessary to interrogate cardiovascular biomechanics.

In my first chapter, I asked whether CNNs can enhance low-resolution cardiac images. That is, can CNNs perform image super-resolution of steady-state free precession (SSFP)? I split this aim into two sub-aims to guide my approach:

1) Given existing CNN architectures commonly used for simple visual tasks, which are best suited for image super-resolution as a first foray into image synthesis?
2) How well does CNN super-resolution perform relative to conventional image upscaling methods?

In my second chapter, I asked whether I could upgrade the CNN architectures from aim 1 to isolate and remove background signal from 4D Flow MRI. That is, can CNNs perform phase-error correction of 4D Flow MRI acquisitions via synthesis of the background static vector field? In doing so, I aimed to extend the capabilities of image synthesis CNNs to perform static vector field synthesis. I split this aim into the following sub-aims:

1) What modifications to the CNNs explored in aim 1 are required to perform vector field synthesis?
2) How well does CNN phase error correction perform relative to existing manual correction methods?

In my third chapter, I build on my findings in aim 2 and asked whether I could further upgrade my phase-error correction CNN to predict intracardiac blood flow from videos of the beating heart. That is, can CNNs infer dynamic blood flow velocity fields from cardiac cine SSFP images? Thus, I aimed to further extend the capability of image synthesis CNNs to perform spatiotemporal vector field synthesis with the following sub-aims:

1) Given the dynamic nature of cardiac blood flow, what architectural modifications are required to incorporate spatiotemporal information into my CNN from aim 2?
2) How well do CNN-inferred flow fields compare with 4D Flow measurements?
3) Can we use CNN-inferred flow at the outflow tract to detect obstructive disease?

In my fourth and final chapter, I asked whether I could refine Triton-Net to evaluate local myocardial function. That is, could I add explicit physical constraints into Triton-Net to infer dynamic myocardial velocity and strain fields from cardiac cine SSFP images? I sought to demonstrate that CNNs can perform tensor field synthesis, and thus permit automated cardiovascular biomechanical analysis. My sub-aims were:

1) What modifications, particularly physical constraints, must be added to the CNN from aim 3 to accomplish inference of strain fields?
2) Given a normal population, what are the baseline ranges for segmental myocardial strain using this CNN method?
3) In an ischemic heart disease population, how well do cardiothoracic radiologists and my CNN identify wall motion abnormalities?
4) What are other potential clinical applications for this CNN?

This introduction was adapted in part from the following manuscripts:

1) “Deep Learning Single-Frame and Multiframe Super-Resolution for Cardiac MRI” in *Radiology*, 2020 by Evan Masutani, Naeim Bahrami, and Albert Hsiao
2) “Deep Learning Automated Background Phase Error Correction for Abdominopelvic 4D Flow MRI” in *Radiology*, 2021 by Sophie You*, Evan Masutani*, Marcus Alley, Shreyas Vasanawala, Pam Taub, Joy Liau, Anne Roberts, and Albert Hsiao
3) “Feasibility off Deep Learning to Synthesize Outflow Hemodynamics from Cardiac MRI”, manuscript in preparation, by Evan Masutani, Tara Retson, Brian Hurt, Kevin Blansit, and Albert Hsiao
4) “Deep Learning Synthetic Strain: Quantitative Assessment of Regional Wall Motion Abnormalities”, manuscript in preparation, by Evan Masutani. Rahul Chandrupatla, Lewis Hahn, Misha Horowitz, Kathleen Jacobs, Seth Kligerman, and Albert Hsiao

*Denote co-first authorship. The dissertation author was the first or co-first author in the listed manuscripts.

Chapter 2: Deep Learning Single-Frame and Multiframe Super-Resolution for Cardiac MRI

2.1 Abstract

Background

Cardiac MRI is limited by long acquisition times, yet faster acquisition of smaller-matrix images reduces spatial detail. Deep learning (DL) might enable both faster acquisition and higher spatial detail via super-resolution.

Purpose

To explore the feasibility of using DL to enhance spatial detail from small-matrix MRI acquisitions and evaluate its performance against that of conventional image upscaling methods.

Materials and Methods

Short-axis cine cardiac MRI examinations performed between January 2012 and December 2018 at one institution were retrospectively collected for algorithm development and testing. Convolutional neural networks (CNNs), a form of DL, were trained to perform super resolution in image space by using synthetically generated low-resolution data. There were 70%, 20%, and 10% of examinations allocated to training, validation, and test sets, respectively. CNNs were compared against bicubic interpolation and Fourier-based zero padding by calculating the structural similarity index (SSIM) between high-resolution ground truth and each upscaling method. Means and standard deviations of the SSIM were reported, and statistical significance was determined by using the Wilcoxon signed-rank test. For evaluation of clinical performance, left ventricular volumes were measured, and statistical significance was determined by using the paired Student’s t-test.

Results

For CNN training and retrospective analysis, 400 MRI scans from 367 patients (mean age, 48 years ± 18; 214 men) were included. All CNNs outperformed zero padding and bicubic interpolation at upsampling factors from two to 64 ($P < .001$). CNNs outperformed zero padding on more than 99.2% of slices (9828 of 9907). In addition, 10 patients (mean age, 51 years ± 22; seven men) were prospectively recruited for super-resolution MRI. Super-resolved low-resolution images yielded left ventricular volumes comparable to those from full-resolution images ($P > .05$), and super-resolved full-resolution images appeared to further enhance anatomic detail.

Conclusion

Deep learning outperformed conventional upscaling methods and recovered high-frequency spatial information. Although training was performed only on short-axis cardiac MRI examinations, the proposed strategy appeared to improve quality in other imaging planes.

2.2 Summary and Key Results

Summary

Deep learning image super resolution can consistently outperform conventional image upscaling methods and can infer high-frequency spatial detail from low-resolution inputs.

Key Results

- When trained with Fourier downsampled data, deep learning consistently outperformed Fourier domain zero padding and bicubic interpolation at upsampling factors of two to 64 ($P < .001$).

- Trained purely in image space, both single-frame and multiframe super-resolution convolutional neural networks (CNNs) showed filling of outer k-space, indicating CNN inference of high-frequency spatial detail.
- Super-resolution of small-matrix acquisitions from 10 patients yielded ventricular volumes comparable ($P > .05$ for each metric) to measurements from full-resolution images with improved image detail.

2.3 Introduction

Cardiac MRI is the clinical reference standard for visual and quantitative assessment of heart function[62]. Specifically, cine balanced steady-state free precession (SSFP) can yield cardiac images with high myocardium–blood pool contrast for evaluation of left ventricular (LV) function[5]. However, MRI suffers from long acquisition times, often requiring averaging across multiple heartbeats[27], and necessitates a trade-off among spatial resolution, temporal resolution, and scan time[28]. Clinically, radiologists are forced to balance acquisition time with resolution to fit clinical needs, and certain applications such as real-time imaging may require small acquisition matrices[30]. Image scaling is typically performed by using conventional upscaling methods, such as Fourier domain zero padding and bicubic interpolation[68,69]. These methods, however, do not readily recover spatial detail[70], such as the myocardium–blood pool interface or delineation of papillary muscles[68].

The concept of super-resolution, or recovery of high-resolution images from low-resolution observations, has been explored since the 1980s for application in video processing[71]. A few algorithms have been proposed[72] in attempts to combine information between spatially shifted and downsampled frames[73]. However, based on physical arguments regarding the transformation between image space and Fourier space, multiple authors are skeptical that such methods are feasible[74–76]. Peled et al[77] and Tieng et al[78] had inconsistent results when attempting to combine information from multiple intersecting imaging planes to recover spatial resolution in the white matter fiber tract and phantoms, respectively. It is largely believed that without prior knowledge, zero padding of outer k-space is the most reliable and effective method for image upscaling and therefore is widely used as the industry standard[75].

Convolutional neural networks (CNNs), a recently developed form of deep learning (DL), may have potential to overcome some of these limitations[56,79]. CNNs learn relevant features from input images to predict desired outputs[56]. In medical imaging, CNNs have shown potential for image classification[80], segmentation[81], and localization[62] for MRI and CT. Important to note, CNNs have a large capacity for recalling learned features and might supply a priori information and assumptions during inference[58]. Our aim was to explore the feasibility of DL for enhancing spatial detail from small-matrix MRI acquisitions and evaluate its performance against that of the conventional image upscaling methods of Fourier domain zero padding and bicubic interpolation.

2.4 Materials and Methods

2.4.1 Prototype Neural Networks

We developed and evaluated four neural networks[56,82,83] for their ability to perform single-frame (k) and multiframe (kt) super resolution. All algorithms were developed by the lead author, a 4th-year doctoral student (E.M.M.). Two general neural network architectures were explored for feasibility in performing this task (Supplemental Fig 1). The first, a relatively shallow network, is a super-resolution CNN–inspired neural network[84], which we refer to as k-SRNet *(http://mmlab.ie.cuhk.edu.hk/projects/SRCNN.html).* The second, a deeper, more complex network, is a modified U-Net CNN[61], which we refer to as k-UNet *(https://github.com/zhixuhao/unet).*

2.4.2 Multiframe Neural Networks

Given that additional data from neighboring time points might improve performance, we extended both architectures to incorporate three-dimensional convolutions, handling the temporal domain in the third dimension. Each input frame was combined with immediately flanking frames to generate input volumes. We refer to these spatiotemporal versions of k-SRNet and k-UNet as kt-SRNet and kt-UNet (Fig 1), respectively.

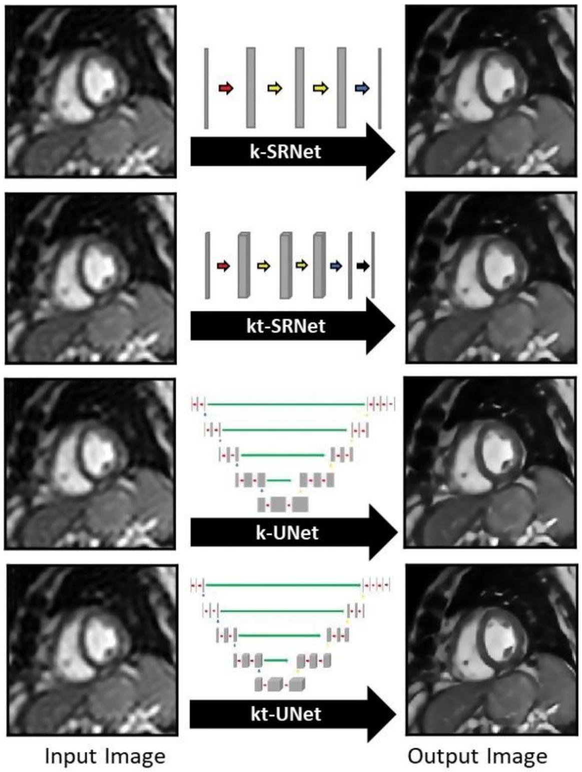

Figure 1: *Prototype Convolutional Neural Networks*. Images show prototype convolutional neural networks (CNNs) evaluated for their performance in generating single-frame (k) and multiframe (kt) super-resolution images. The k-SRNet and kt-SRNet CNNs are examples of shallow networks and k-UNet and kt-UNet

2.4.3 Patients and Image Data

This study was compliant with the Health Insurance Portability and Accountability Act, and institutional review board approval and waiver of written informed consent were obtained. We retrospectively collected a convenience sample of short-axis (SAX) cine SSFP series from 400 clinical cardiac MRI examinations performed at our academic institution in 367 patients between January 2012 and December 2018 for algorithm development (Table 1). No exclusion criteria were applied. Of these 400 studies, 200 were performed with a 1.5-T MRI scanner (Signa HDxt; GE Healthcare, Waukesha, Wis) and 200 were performed with a 3.0-T MRI scanner (Discovery MR750 DV26; GE Healthcare) (Table 2).

Table 1: *Patient Demographics*

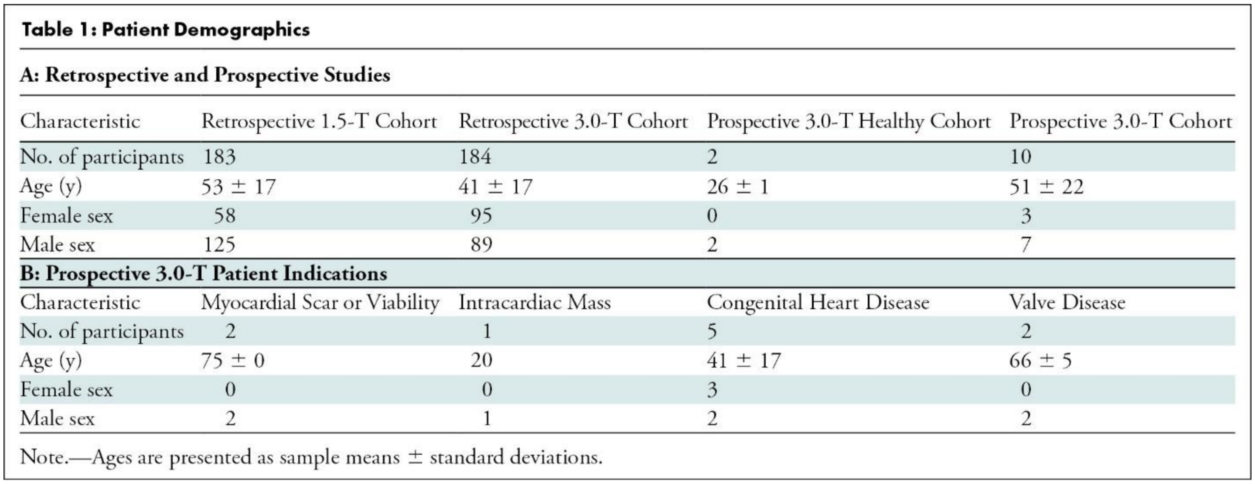

Table 1: Patient Demographics

A: Retrospective and Prospective Studies

Characteristic	Retrospective 1.5-T Cohort	Retrospective 3.0-T Cohort	Prospective 3.0-T Healthy Cohort	Prospective 3.0-T Cohort
No. of participants	183	184	2	10
Age (y)	53 ± 17	41 ± 17	26 ± 1	51 ± 22
Female sex	58	95	0	3
Male sex	125	89	2	7

B: Prospective 3.0-T Patient Indications

Characteristic	Myocardial Scar or Viability	Intracardiac Mass	Congenital Heart Disease	Valve Disease
No. of participants	2	1	5	2
Age (y)	75 ± 0	20	41 ± 17	66 ± 5
Female sex	0	0	3	0
Male sex	2	1	2	2

Note.—Ages are presented as sample means ± standard deviations.

Table 2: *MRI Short-Axis Cine Steady-State Free Precession Parameters*

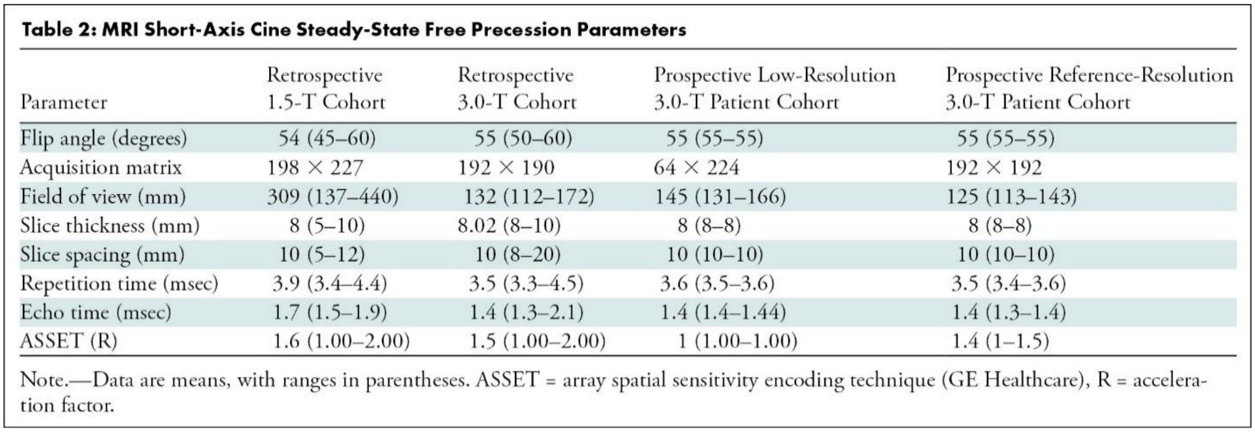

Table 2: MRI Short-Axis Cine Steady-State Free Precession Parameters

Parameter	Retrospective 1.5-T Cohort	Retrospective 3.0-T Cohort	Prospective Low-Resolution 3.0-T Patient Cohort	Prospective Reference-Resolution 3.0-T Patient Cohort
Flip angle (degrees)	54 (45–60)	55 (50–60)	55 (55–55)	55 (55–55)
Acquisition matrix	198 × 227	192 × 190	64 × 224	192 × 192
Field of view (mm)	309 (137–440)	132 (112–172)	145 (131–166)	125 (113–143)
Slice thickness (mm)	8 (5–10)	8.02 (8–10)	8 (8–8)	8 (8–8)
Slice spacing (mm)	10 (5–12)	10 (8–20)	10 (10–10)	10 (10–10)
Repetition time (msec)	3.9 (3.4–4.4)	3.5 (3.3–4.5)	3.6 (3.5–3.6)	3.5 (3.4–3.6)
Echo time (msec)	1.7 (1.5–1.9)	1.4 (1.3–2.1)	1.4 (1.4–1.44)	1.4 (1.3–1.4)
ASSET (R)	1.6 (1.00–2.00)	1.5 (1.00–2.00)	1 (1.00–1.00)	1.4 (1–1.5)

Note.—Data are means, with ranges in parentheses. ASSET = array spatial sensitivity encoding technique (GE Healthcare), R = acceleration factor.

2.4.4 Synthetic Training Data

We developed a strategy for generation and use of synthetic training data to mimic the super-resolution task. Training workflow comprised two steps: *(a)* cropping a central 128 × 128 area of the SAX image to standardize image presentation and serve as ground truth and *(b)* windowing a central region of k-space to generate synthetic training data (Fig 2).

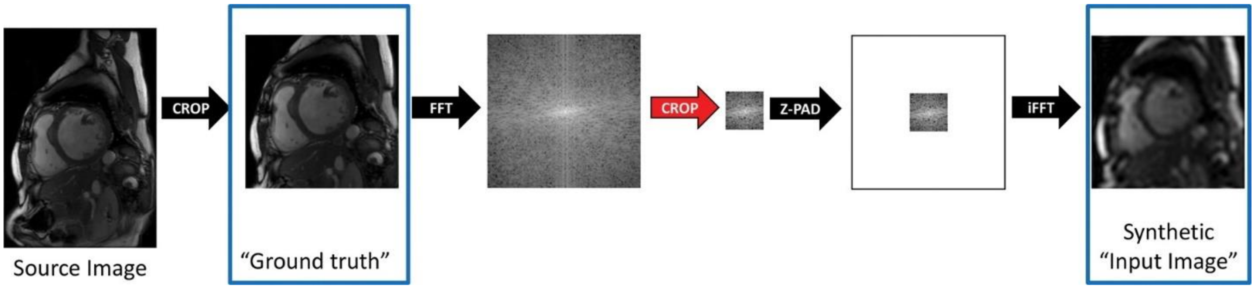

Figure 2: *Diagram shows strategy for generation of synthetic training data*. Source image data were first cropped to standardize image presentation to the neural network and were windowed in Fourier space to mimic a fully sampled low-resolution acquisition. The cropped images were later used as ground truth for training, and the downsampled images were used as synthetic input images. Z-PAD = zero padding.

2.4.5 Fourier Downsampling

To mimic low-resolution small-matrix MRI acquisitions, we performed a process we refer to as Fourier downsampling. Each downsampling factor was simulated by retaining central windows of k-space of varying sizes. Outer portions of k-space were zero filled to a matrix size of 128 × 128. Images were transformed back to the image domain, and pixel values were scaled to 0 and 1. Each downsampling (and commensurate upsampling) factor was defined as the ratio of the k-space window area to the cropped 128 × 128 area.

2.4.6 Neural Network Training

SAX examinations were randomly divided and allocated to 70% (140 of 200 1.5-T examinations and 140 of 200 3-T examinations) for training, 20% (40 of 200 1.5-T examinations and 40 of 200 3.0-T examinations) for validation, and 10% (20 of 200 1.5-T examinations and 20 of 200 3.0-T examinations) for testing. We trained our networks on two workstations running Ubuntu 16.04 (Canonical, London, England) and equipped with either two Titan Xp graphics cards or one Titan V graphics card (Nvidia, Santa Clara, Calif). We used Keras 2.2.4 with TensorFlow-GPU 1.12.0 (Google, Mountain View, Calif) at the back end for all DL experiments.

2.4.7 Hybrid Loss Function

We chose to use a hybrid loss function based on the work of Zhao et al[85]. Specifically, our loss function was the sum of L1 loss and a modified form of the multiscale structural similarity index (SSIM) loss (defined as 1 minus multiscale SSIM)[86] (Supplemental Appendix).

2.4.8 Evaluation of Performance

In compliance with the Health Insurance Portability and Accountability Act and with institutional review board approval and written informed consent, we prospectively acquired SAX and four-chamber cine SSFP cardiac MRI series at 3.0 T in two healthy men and 10 clinical patients at low resolution and full resolution (Table 1). Low-resolution scans were performed with a 64 × 224 matrix (resulting in a 3.5-fold shortened scan time), and full-resolution scans were performed with a 192 × 192 matrix while leveraging the array spatial sensitivity encoding technique (ASSET; GE Healthcare). The super-resolution networks were then applied to low-resolution acquisitions and, with a tiling approach, they were also applied to full-resolution acquisitions (Supplemental Appendix).

To evaluate the clinical utility of our strategy, we measured LV end-diastolic volume (EDV), LV end-systolic volume (ESV), LV stroke volume (SV), and LV ejection fraction (EF) in the patient cohort. One researcher (E.M.M.) performed all segmentation and volumetric analyses with software (Arterys Cardio DL, version 19.14.2; Arterys, San

Francisco, Calif) under the supervision of a cardiovascular radiologist with 12 years of experience in cardiac MRI (A.H.).

2.4.9 Statistical Analysis

We compared CNN-based approaches and conventional methods of bicubic interpolation and zero padding by calculating the SSIM[87] between each ground truth image and its corresponding super-resolved image from each method of upscaling (Fig 3, A). We reported the mean and standard deviation of SSIM and determined statistical significance by using the Wilcoxon signed-rank test with a type I error threshold of 0.05 ($P < .05$). For our comparison of SSIM performance relative to zero padding (Fig 3, B), we calculated the pairwise difference of SSIM between zero padding and each super-resolution method.

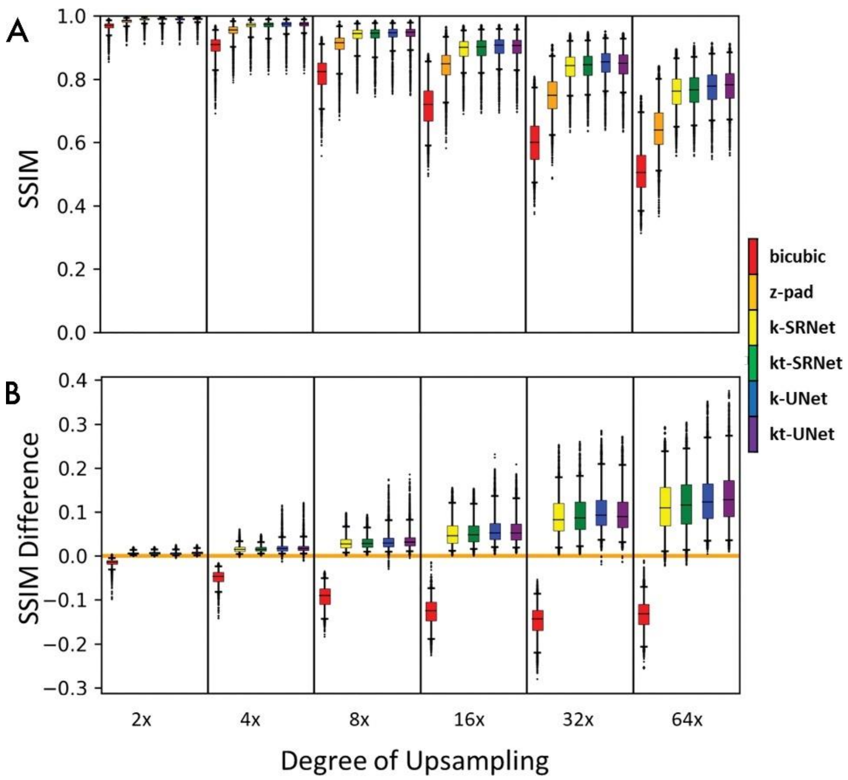

Figure 3: *Box-and-whisker plots compare performance based on the structural similarity index (SSIM) for each super-resolution method across multiple upsampling factors*. Boxes encapsulate interquartile ranges, whiskers demarcate the central 95% of data points, and black bars lie on the median (*n* = 9907 short-axis slices from testing set). *A,* Aggregate performance for each super-resolution method. *B,* Pairwise comparison of performance between each method and zero padding (z-pad). Deep learning–based methods consistently outperformed conventional methods on bulk and per-slice bases. Neural network–based methods outperformed traditional bicubic and zero padding for nearly every slice evaluated. Zero padding outperformed the bicubic method for nearly every slice evaluated. k = single frame, kt = multiframe.

To compare LV volumes from paired CNN super-resolved low-resolution acquisitions and high-resolution clinical acquisitions, we reported the mean and standard deviation of LV EDV, LV ESV, LV SV, and LV EF and determined statistical significance by using paired Student *t* test with a type I error threshold of 0.05 (*P* < .05). We used software (Python, version 3.5, Python Software Foundation, Wilmington, Del; Microsoft Excel, version 1912, Microsoft, Redmond, Wash) for all statistical analyses.

2.5 Results

2.5.1 Patient Characteristics

For CNN development, we retrospectively collected 200 1.5-T examinations from 183 patients (mean age, 53 years ± 17; 125 male patients) and 200 3.0-T examinations from 184 patients (41 years ± 17; 89 male patients). We prospectively collected two 3.0-T examinations from two healthy volunteers (26 years ± 1; two male patients) and 10 3.0-T examinations from 10 clinical patients (51 years ± 22; seven male patients) (Table 1). We did not exclude any of our initial 12 prospectively acquired participants.

2.5.2 Quantitative Differences

The SSIMs of shallow (SRNet) and deep (UNet) CNNs are shown in Table 3 and Figure 3. Mean SSIMs for zero padding ranged from 0.645 ± 0.074 at upsampling by a factor of 64 to 0.983 ± 0.007 at upsampling by a factor of two. Mean SSIMs for k-SRNet, the most poorly performing CNN, ranged from 0.760 ± 0.056 at upsampling by a factor of 64 to 0.989 ± 0.006 at upsampling by a factor of two. For all degrees of upsampling tested, every CNN outperformed conventional upscaling methods (*P* < .001) (Fig 3, A).

Table 3: *Pairwise Comparison of Shallow (SRNet) and Deep (UNet) Methods for Super Resolution*

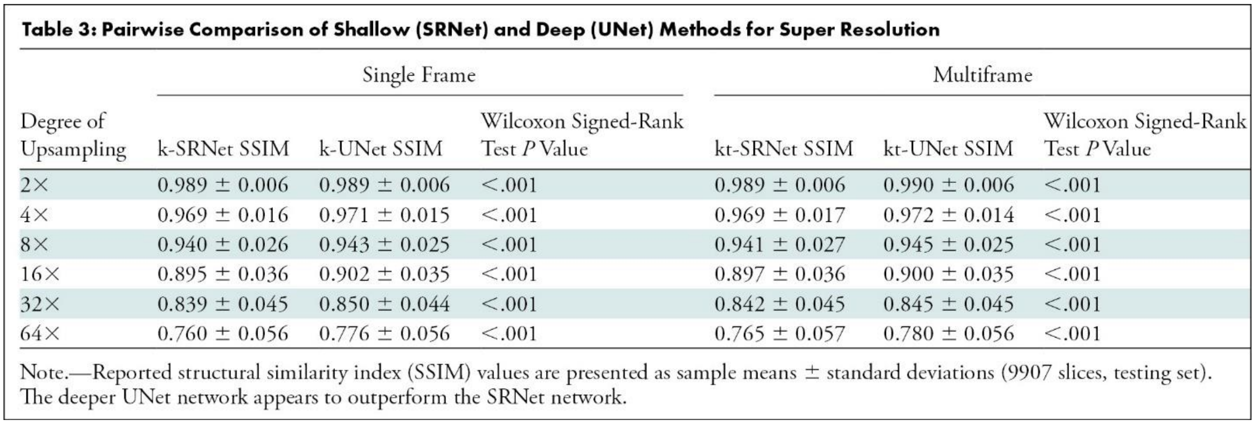

Table 3: Pairwise Comparison of Shallow (SRNet) and Deep (UNet) Methods for Super Resolution

	Single Frame			Multiframe		
Degree of Upsampling	k-SRNet SSIM	k-UNet SSIM	Wilcoxon Signed-Rank Test *P* Value	kt-SRNet SSIM	kt-UNet SSIM	Wilcoxon Signed-Rank Test *P* Value
2×	0.989 ± 0.006	0.989 ± 0.006	<.001	0.989 ± 0.006	0.990 ± 0.006	<.001
4×	0.969 ± 0.016	0.971 ± 0.015	<.001	0.969 ± 0.017	0.972 ± 0.014	<.001
8×	0.940 ± 0.026	0.943 ± 0.025	<.001	0.941 ± 0.027	0.945 ± 0.025	<.001
16×	0.895 ± 0.036	0.902 ± 0.035	<.001	0.897 ± 0.036	0.900 ± 0.035	<.001
32×	0.839 ± 0.045	0.850 ± 0.044	<.001	0.842 ± 0.045	0.845 ± 0.045	<.001
64×	0.760 ± 0.056	0.776 ± 0.056	<.001	0.765 ± 0.057	0.780 ± 0.056	<.001

Note.—Reported structural similarity index (SSIM) values are presented as sample means ± standard deviations (9907 slices, testing set). The deeper UNet network appears to outperform the SRNet network.

On a per-slice basis, every CNN consistently outperformed zero padding for nearly all input images (Fig 3, B). All four methods—k-SRNet, kt-SRNet, k-UNet, and kt-UNet—outperformed zero padding on more than 99.2% (9828 of 9907) of slices at all reported degrees of upsampling.

For synthetic test data, there were differences between SRNet and UNet (Table 3). For all degrees of upsampling, k-UNet and kt-UNet outperformed k-SRNet and kt-SRNet, respectively (*P* < .001). In addition, kt-SRNet outperformed k-SRNet at all degrees of upsampling (*P* < .001), whereas kt-UNet outperformed k-UNet at upsampling factors of two, four, eight, and 64 (*P* < .001). We observed average SSIM within 0.02 of all CNNs across each upsampling factor, in contrast to a widening performance gap with conventional upscaling methods with higher upsampling factors (Fig 3, A).

2.5.3 Qualitative Differences

We present examples of each upsampling method in a 62-year-old man (Fig 4). At upsampling by a factor of eight, bicubic interpolation showed noticeably reduced sharpness of the right ventricular trabeculations and the myocardium–blood pool interface. At upsampling by a factor of 16, all methods showed noticeable image quality degradation, particularly with respect to papillary muscle sharpness; however, the edges of the interventricular septum were noticeably sharper in the CNN outputs. At upsampling by a factor of 32, the LV papillary muscles appeared to blend in with the LV walls in the bicubic and zero-padding outputs. The ventricular walls were noticeably blurry in bicubic and zero-padding outputs. Although there was some gross loss in texture of the blood pool and blurriness of the papillary muscles in the CNNs, the boundaries of the ventricular walls remained sharp. At upsampling by a factor of 64, the boundary between the right ventricular wall and the blood pool became severely blurred with the conventional upscaling methods; all papillary muscle detail was also lost. The ventricular walls and boundaries remained sharp in all CNNs. From upsampling factors of eight to 64, z padding shows increasingly noticeable Gibbs artifact, which is absent in CNN predictions.

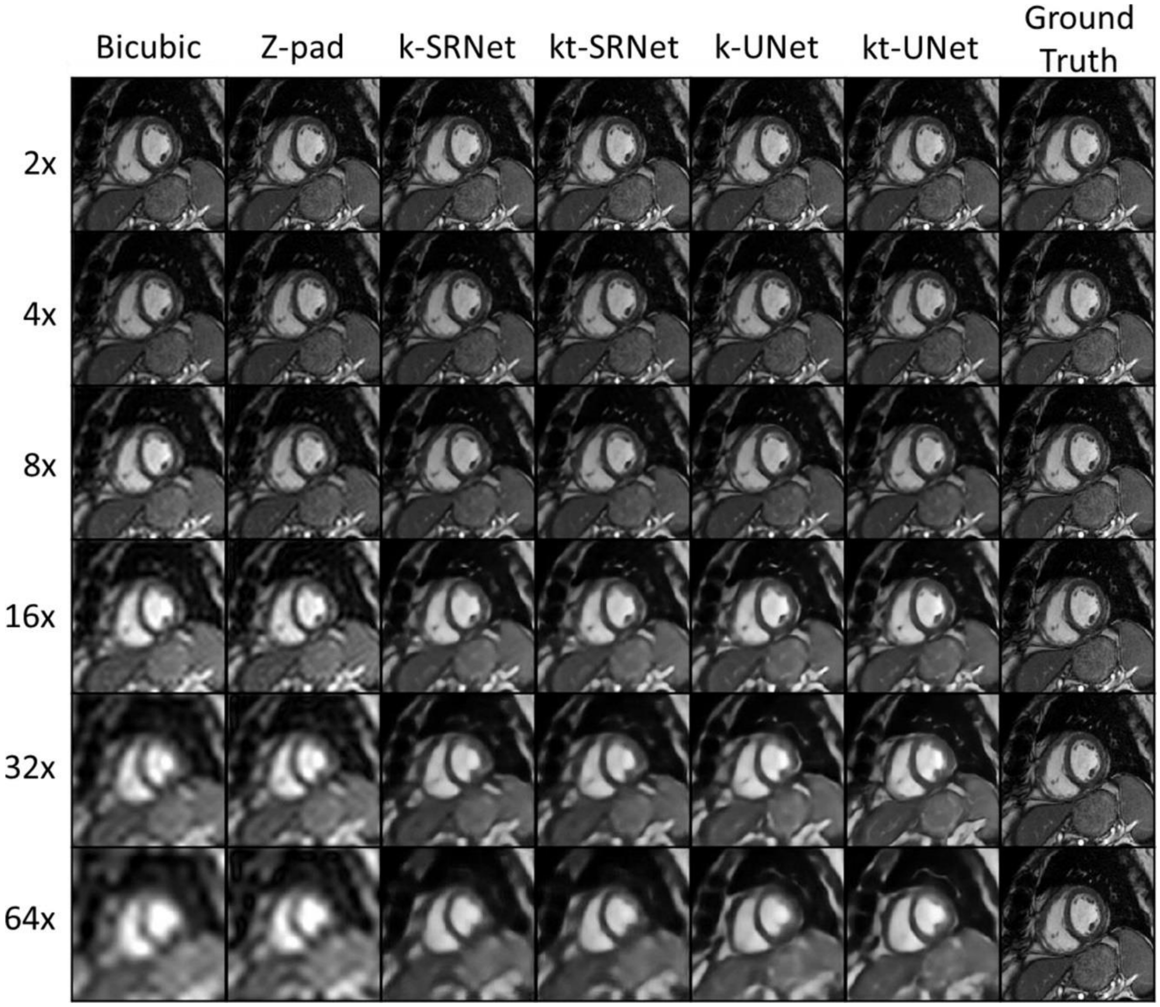

Figure 4: *Representative example images in a 62-year-old man for comparison of super-resolution methods across multiple upsampling factors*. Neural network–based methods had a pronounced effect at upsampling by a factor of eight or more. k = single frame, kt = multiframe, Z-pad = zero padding.

We present representative examples, upsampled by a factor of eight with each super-resolution method, in Figure 5. Each example shows the output image and corresponding k-space log plots for each method. In a 36-year-old man with hypertrophic cardiomyopathy examined at 1.5 T (Fig 5, A), only bicubic interpolation showed reduced image quality relative to ground truth. The log plots indicate that CNNs filled the outer k-space. CNNs also reduced severe radiofrequency artifacts in a 1.5-T examination in a 44-year-old woman (Fig 5, B). Both bicubic interpolation and zero padding showed reduced sharpness at the myocardium–blood pool interface and increased graininess compared with CNN outputs. The log plots showed radiofrequency artifacts in ground truth outer k-space, which were markedly reduced in CNN predictions.

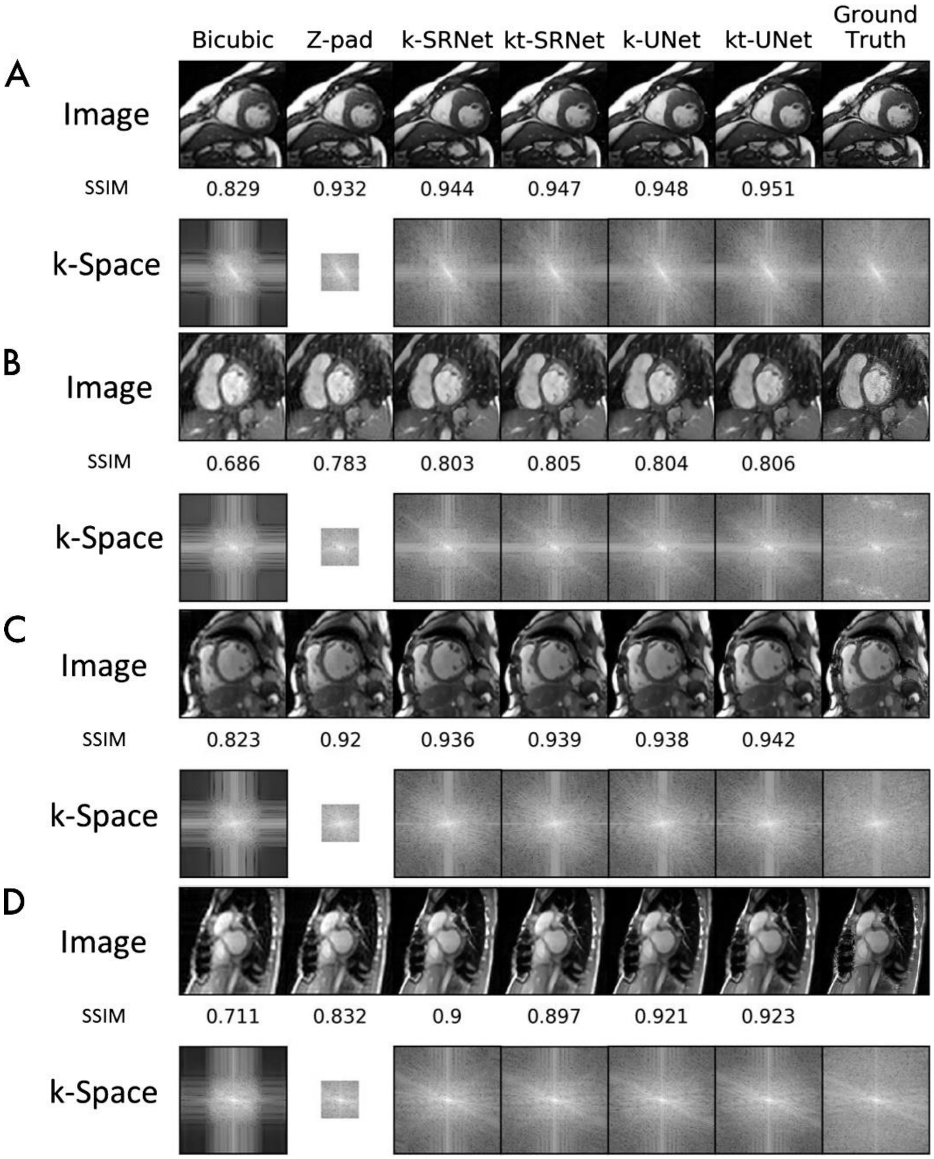

Figure 5: *Example images compare super-resolution methods at upsampling by a factor of eight.* Output images and corresponding log plots of k-space are shown along with the structural similarity index (SSIM) relative to ground truth. At 1.5 T, neural network methods, A, perform well in a 36-year-old male patient with hypertrophic cardiomyopathy and, B, serendipitously repair severe radiofrequency artifact in the outer k-space in a 44-year-old female patient. At 3.0 T, neural network methods, C, perform well in a 54-year-old female patient with dilated cardiomyopathy and, D, tolerate artifacts from sternal wires in a 28-year-old female patient. k = single frame, kt = multiframe, Z-pad = zero padding.

In a 54-year-old woman with dilated cardiomyopathy examined at 3.0 T (Fig 5, C), we saw loss of image sharpness with bicubic interpolation alone. The corresponding log plots indicated filling of outer k-space for all CNNs. CNNs also successfully super-resolved a 3.0-T examination with artifact from sternal wires in a 28-year-old woman (Fig 5, D). Both bicubic interpolation and zero padding showed increased blurring of the myocardium–blood pool boundary relative to CNN outputs. SSIMs of bicubic interpolation and zero padding were also markedly lower relative to CNN predictions. The log plots again indicated outer k-space filling by CNNs.

To illustrate an extreme upsampling factor, we performed super-resolved examinations upsampled by a factor of 64 at 1.5 and 3.0 T (Supplemental Fig 2). All super-resolution–method outputs displayed loss of detail in right ventricular trabeculations, LV papillary muscles, and the blood pool; however, CNNs clearly demarcated the myocardium–blood pool boundary. CNNs also exhibited markedly higher SSIM.

2.5.4 Clinical Proof of Concept

To assess clinical feasibility of the super-resolution technique, we undertook a proof-of-concept evaluation, prospectively acquiring SAX and four-chamber SSFP images in low resolution and full resolution in two healthy participants and 10 clinical patients (Fig 6).

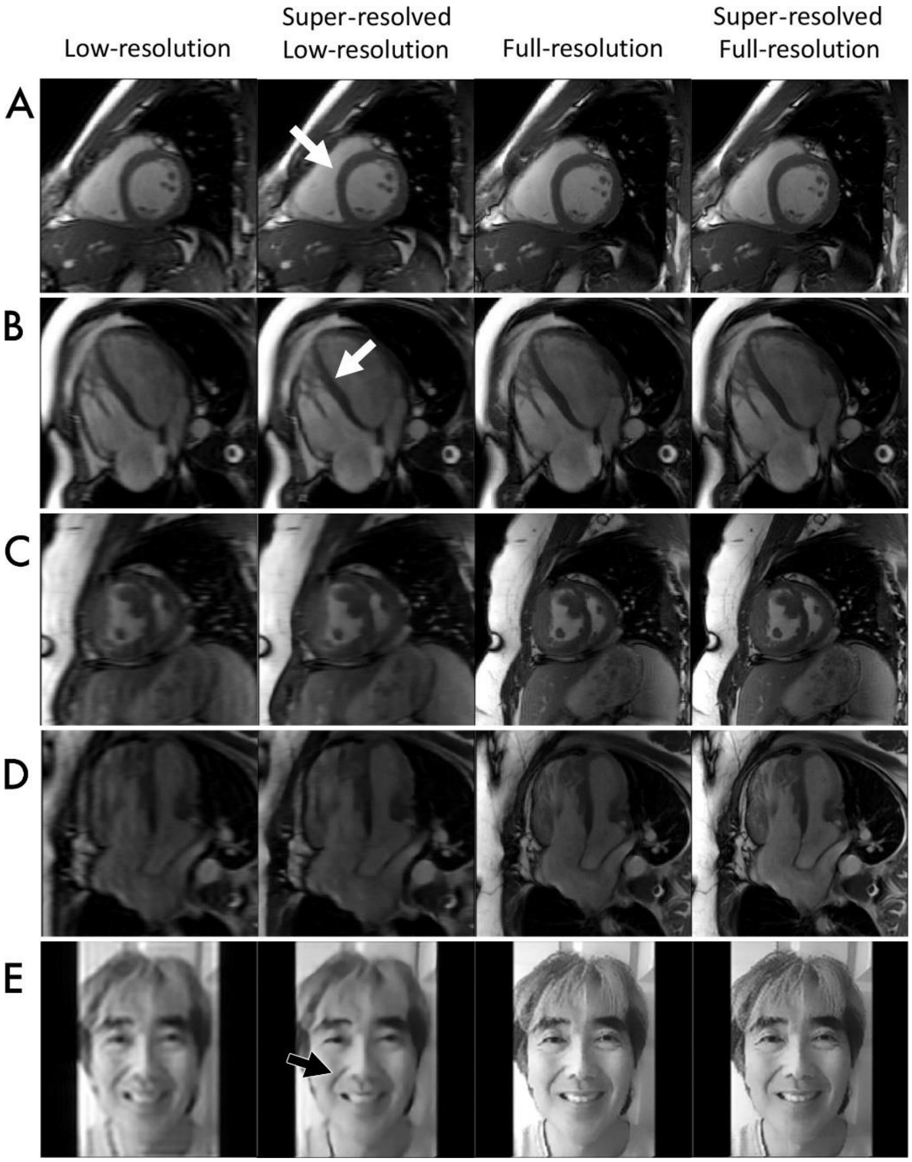

Figure 6: *Images demonstrate proof-of-concept assessment of super-resolution methods.* Low-resolution input, full-resolution reference, and k-UNet super-resolved images are shown for five experiments: A, short-axis cine steady-state free precession (SSFP) in a 27-year-old healthy male volunteer at 3.0 T, B, four-chamber cine SSFP in a 26-year-old healthy male volunteer at 3.0 T, C, short-axis cine SSFP in a 36-year-old patient with transposition of the great arteries after Mustard switch, D, four-chamber cine SSFP in the same patient as in, C, and, E, photographs of a human face. The k-UNet network appears to improve myocardium–blood pool delineation, especially along the septal wall. Although trained only with short-axis images, the k-UNet network appears to generalize to long-axis images and digital photographs, sharpening details. This network also appears to further enhance detail of low-resolution images and full-resolution reference acquisitions.

In the two healthy participants, we qualitatively assessed the performance of CNNs in enhancing anatomic detail. The k-UNet successfully super-resolved 2.4-fold abbreviated 3.0-T SAX images in a healthy 27-year-old man. We noted sharpening of the myocardium–blood pool interface, right ventricular trabeculations, and LV papillary muscles (Fig 6, A). The k-UNet, trained only on SAX images, also super-resolved 2.4-fold abbreviated four-chamber acquisitions from a healthy 26-year-old man and increased sharpness of right ventricular trabeculations and the septal wall (Fig 6, B).

In the cohort of 10 clinical patients, we quantitatively assessed ventricular volumetry and ejection fraction. There were no significant differences between volumetric measurements obtained from super-resolved low-resolution images and full-resolution images (Table 4). On average, reference examinations yielded LV EDV of 152 mL, LV ESV of 58 mL, LV SV of 96 mL, and LV EF of 64%. On average, super-resolved low-resolution images yielded values as follows, and the differences were not significantly different: LV EDV, 152 mL (*P* = .99); LV ESV, 55 mL (*P* = .40); LV SV, 98 mL (*P* = .57); and LVEF, 65% (*P* = .27). From this cohort, we show representative super-resolved low-resolution SAX (Fig 6, C) and four-chamber (Fig 6, D) images from a 36-year-old female patient with transposition of the great arteries after Mustard atrial switch. Super resolution yielded reduced Gibbs artifact and sharpened myocardium–blood pool interfaces compared with the low-resolution input images. When applied to full-resolution input images, super resolution also achieved a similar effect, with reduced Gibbs artifact and sharpened myocardium–blood pool interfaces.

Table 4: *Pairwise Comparison of LV Volumes Derived from Prospectively Acquired Examinations*

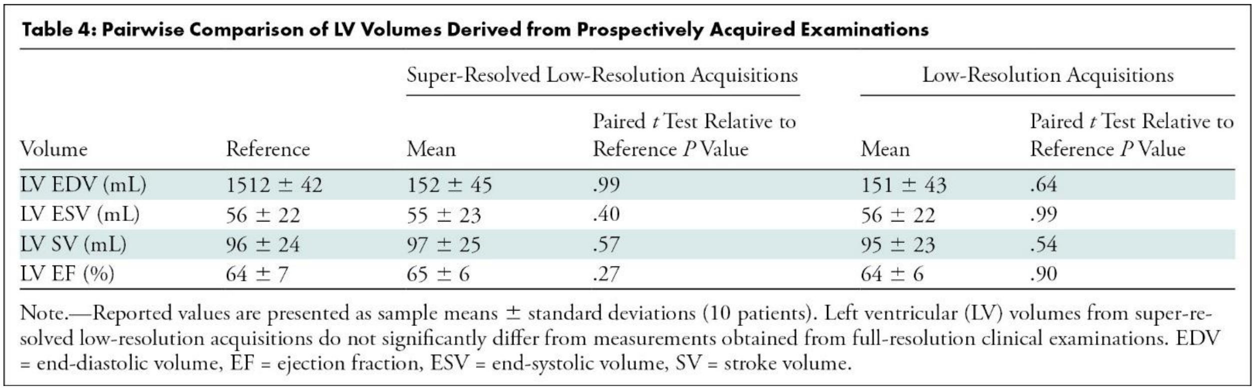

Table 4: Pairwise Comparison of LV Volumes Derived from Prospectively Acquired Examinations

		Super-Resolved Low-Resolution Acquisitions		Low-Resolution Acquisitions	
Volume	Reference	Mean	Paired *t* Test Relative to Reference *P* Value	Mean	Paired *t* Test Relative to Reference *P* Value
LV EDV (mL)	1512 ± 42	152 ± 45	.99	151 ± 43	.64
LV ESV (mL)	56 ± 22	55 ± 23	.40	56 ± 22	.99
LV SV (mL)	96 ± 24	97 ± 25	.57	95 ± 23	.54
LV EF (%)	64 ± 7	65 ± 6	.27	64 ± 6	.90

Note.—Reported values are presented as sample means ± standard deviations (10 patients). Left ventricular (LV) volumes from super-resolved low-resolution acquisitions do not significantly differ from measurements obtained from full-resolution clinical examinations. EDV = end-diastolic volume, EF = ejection fraction, ESV = end-systolic volume, SV = stroke volume.

To explore whether our CNNs have applicability beyond MRI, we super-resolved a low-resolution photograph of a human face (Fig 6, E). The k-UNet removed much of the Gibbs artifact and sharpened edges. Finally, we further super-resolved high-resolution reference images using k-UNet. We observed sharper edges and less pixelation on all super-resolved high-resolution reference images.

2.6 Discussion

We have demonstrated the feasibility of convolutional neural networks (CNNs) to super-resolve cardiac MRI scans acquired at both 1.5 T and 3.0 T at a wide range of upsampling factors. We quantitatively showed that both SRNets and UNets outperform conventional upscaling methods including Fourier domain zero padding and bicubic interpolation at multiple upsampling factors as evaluated with structural similarity index (SSIM) on more than 99.2% (9828 of 9907) of slices ($P < .001$). Qualitatively, CNNs appeared to improve some spatial details, including the myocardium–blood pool boundary. We further showed that this approach works not only with synthetic low-resolution data, but also prospectively with patients referred clinically for cardiac MRI.

Super resolution does not appear to negatively impact ventricular volumetry, achieving comparable left ventricular (LV) end-diastolic volume, LV end-systolic volume, LV stroke volume, and LV ejection fraction values between super-resolved low-resolution images and full-resolution reference images, while recovering noticeable improvement in spatial detail.

The concept of super-resolution in MRI has been explored in earlier studies, albeit without application of CNNs. These studies[71,77,78] attempted to recover in-plane high-frequency spatial information from multiple low-resolution frames but were not successful[71,74–76]. Many authors have felt that spatially shifted low-resolution images do not provide informational content to resolve high-frequency detail. Unlike earlier approaches, the CNNs we explored here appeared to work even on a single image frame. In fact, the addition of multiple adjacent frames did not markedly improve performance in our study. We are uncertain why each of the CNNs we evaluated appeared to accomplish super-resolution. We speculate that this might be related to the large feature capacity of CNNs[58], which can carry learned information as prior knowledge. For this application, the learned information appears to generalize across multiple views, including the four-chamber view and, surprisingly, a photograph of a human face.

Clinically, super resolution could be used to reduce scan time, increase temporal resolution, or both. Acquisition time is, of course, proportional to the number of phase-encode lines measured[88]. This results in relatively long breath holds for cardiac MRI, which cannot be tolerated by many patients. Multiple methods are now available to abbreviate acquisition, including parallel imaging[88] and compressed sensing[89]. Given that we have been able to implement this as an image-space task, it is possible that CNN-based super resolution may be combined with these techniques.

Our study had some limitations. First, initial analyses of performance were based on synthetically downsampled images. Second, we sourced training data from scanners from one vendor at one institution. Clinical evaluation was limited to proof of concept, showing feasibility in 12 patients. Finally, we were able to apply super-resolution to the full-resolution image data, but ultimately there is no reference standard for this final comparison because exceedingly long breath holds would be required.

In conclusion, in this proof-of-concept study we showed that convolutional neural network (CNNs) can recover high-frequency spatial detail from low-resolution MRI scans. Each of the CNNs we evaluated (SRNet and Unet) outperformed traditional zero padding and bicubic image upscaling strategies. Further work may be required to evaluate general applicability across institutions, MRI vendors, or other pulse sequences, but these results show feasibility of super-resolution methods to improve the speed of MRI acquisition. In particular, for cardiac MRI, it is often challenging to acquire high-quality images in patients with arrhythmia. A real-time strategy that combines multiple techniques including CNN super-resolution might make this more feasible.

2.7 Acknowledgements

We gratefully acknowledge the National Institute of General Medical Sciences; National Heart, Lung, and Blood Institute; and GE Healthcare for their generous support for this work. We thank Nvidia for generously donating Titan Xp and GV100 GPUs for training the convolutional neural networks in this research and the San Diego

Supercomputer Center for providing GPU-accelerated compute time. Additionally, we thank Dr Stephen Masao Masutani, the lead author's father, for providing a photograph of his face for use in this work.

This chapter was adapted, in part, from "Deep Learning Single-Frame and Multiframe Super-Resolution for Cardiac MRI" in Radiology (2020). The author list is: Masutani, Evan; Bahrami, Naeim; Hsiao, Albert. The dissertation author was the primary investigator and author of this paper.

2.8 Appendix: Supplemental Materials and Methods

2.8.1 Neural Network Training Data

From 400 short-axis examinations, we used 37,700 1.5T images + 32,380 3.0T images for training, 10,720 1.5T images + 32,380 3.0T images for validation, and 5,167 1.5T images + 4,740 3.0T images for testing. All reported statistical analyses are based on performance on the test set.

2.8.2 Recovery of Fourier Data from DICOM Files

To recover measured k-space data from source Digital Imaging and Communications in Medicine (DICOM) files, we first queried the Acquisition Matrix (0018,1310) field to determine the extent of Fourier zero-padding used by the manufacturer. We effectively reversed this zeropadding by transforming the DICOM pixel data to k-space and removing interpolated data beyond the acquisition matrix geometry.

2.8.3 Fourier Downsampling of Multiframe Data

To generate synthetic multiframe training data, we performed the same downsampling strategy at the time frame of interest and adjacent flanking time frames.

The three downsampled frames were stacked as a single volume to provide an input for the multiframe variants of the neural networks.

2.8.4 Hybrid Loss Function

We used the Tensorflow implementation of multiscale structural similarity index (MS-SSIM) and its default settings for filter size = 11, filter sigma = 1.5, k1 = 0.01, and k2 = 0.03. Due to relatively small 128 × 128 matrix size for training data, we only used the first four default MSSSIM power factors and renormalized them resulting in the weights [0.0517,0.3295,0.3462,0.2726]. For multiframe experiments, we added the 3D L1-loss to the mean of the MS-SSIM losses calculated for each of the three adjacent timeframes.

2.8.5 Other Training Parameters

We used the hyperbolic tangent as the final activation function for all cognitive neural networks (CNNs). Additionally, we used the Adam optimizer with a learning rate of 1e-4. We performed training with early-stopping for a maximum of 25 epochs. We trained a unique set of UNets and SRNets for multiple degrees of upsampling, from 2× to 64×.

Super-Resolution of Low-Resolution Images

To predict a high-resolution image from low-resolution inputs, we z-padded outer k-space of the low-resolution acquisitions, transformed them to the image domain, retained the central 128 × 128, and scaled pixel values to [0,1] prior to CNN inference.

2.8.6 Super-Resolution of Full-Resolution Images

To further super-resolve full-resolution acquisitions, we divided each full-resolution image into tiles, transformed the tiles into k-space, z-padded them to 128 × 128, converted them to image space, and scaled pixel values to [0,1] prior to CNN inference. We then concatenated the superresolved tiles to form a higher resolution image. As an example, to super-resolve a 128 × 128 image by a factor of 4 (2× along the row direction and 2× along the column direction), we first subdivide the source image into 4 64 × 64 tiles. We then transform each tile to k-space and z-pad them to 128 × 128. We then convert each tile back to image space, scale the pixel values to [0,1], and use k-UNet to super-resolve each tile. Following super-resolution, we have 4 128 × 128 tiles which, in this case, correspond to the four quadrants of our input image. We then concatenate the tiles relative to their original position in the source image to generate a final 256 × 256 super-resolved image.

2.9 Supplemental Figures

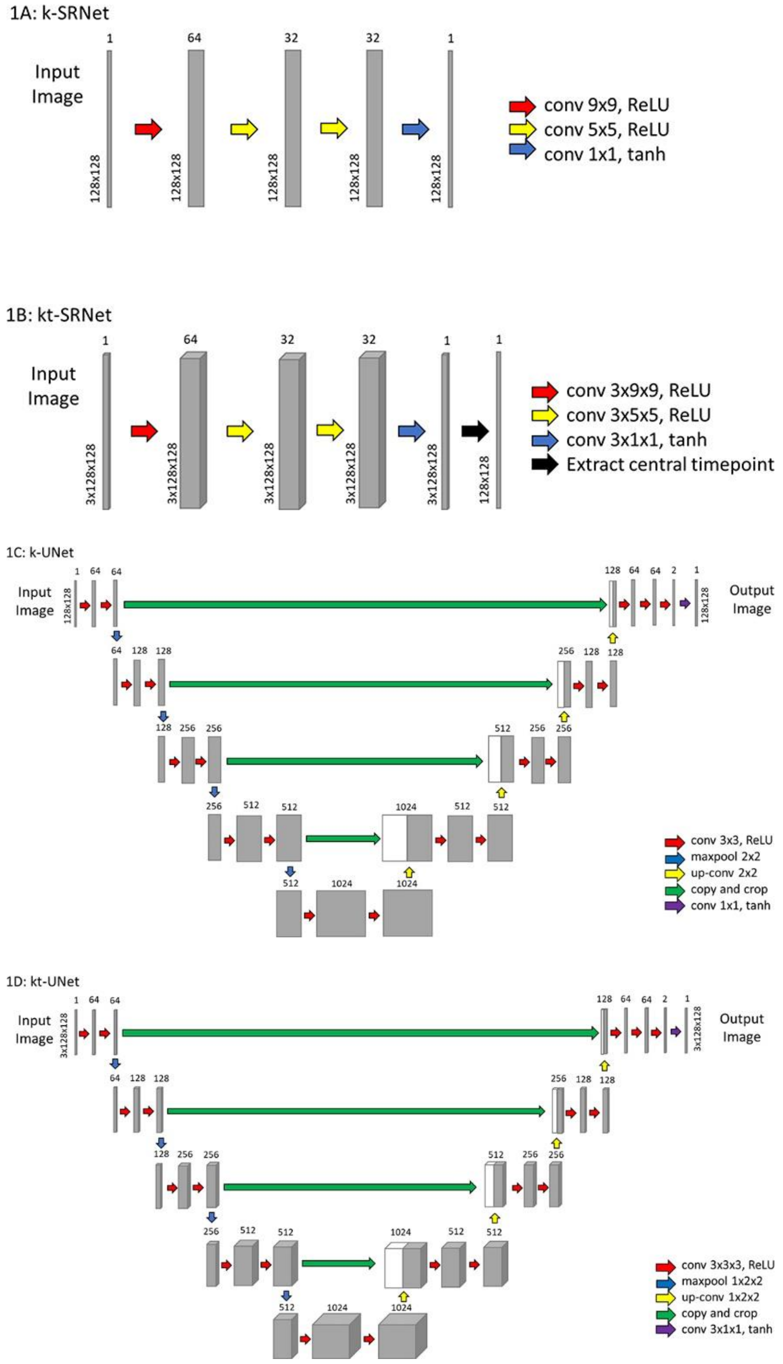

Supplemental Figure 1: *Four prototype CNNs we trained and evaluated for single-frame and multiframe super-resolution.* kt-SRNet and kt-UNet perform multiframe super-resolution on three temporally adjacent input images. Layer dimensions lie beside gray bars; number of channels lie atop gray bars. 3D gray bars in kt-SRNet and kt-Unet emphasize use of 3D convolutions.

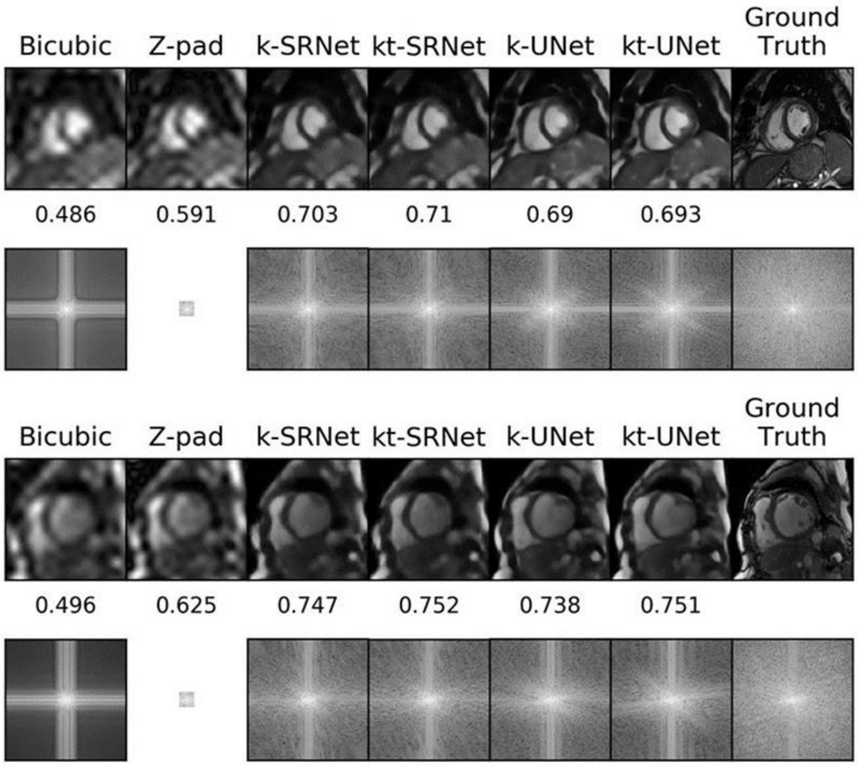

Supplemental Figure 2: *MRI examples comparing super-resolution methods at 64× upsampling.* Output images and corresponding log plots of k-space are shown along with structural similarity (SSIM) relative to ground truth. CNNs improve image quality at (top) 1.5T and (bottom) 3.0T.

Chapter 3: Deep Learning Automated Background Phase Error Correction for Abdominopelvic 4D Flow MRI

3.1 Abstract

Background

Four-dimensional (4D) flow MRI has the potential to provide hemodynamic insights for a variety of abdominopelvic vascular diseases, but its clinical utility is currently impaired by background phase error, which can be challenging to correct.

Purpose

To assess the feasibility of using deep learning to automatically perform image-based background phase error correction in 4D flow MRI and to compare its effectiveness relative to manual image-based correction.

Materials and Methods

A convenience sample of 139 abdominopelvic 4D flow MRI acquisitions performed between January 2016 and July 2020 was retrospectively collected. Manual phase error correction was performed using dedicated imaging software and served as the reference standard. After reserving 40 examinations for testing, the remaining examinations were randomly divided into training (86% [85 of 99]) and validation (14% [14 of 99]) data sets to train a multichannel three-dimensional U-Net convolutional neural network. Flow measurements were obtained for the infrarenal aorta, common iliac arteries, common iliac veins, and inferior vena cava. Statistical analyses included Pearson correlation, Bland-Altman analysis, and *F* tests with Bonferroni correction.

Results

A total of 139 patients (mean age, 47 years ± 14 [standard deviation]; 108 women) were included. Inflow-outflow correlation improved after manual correction ($\rho = 0.94$, $P < .001$) compared with that before correction ($\rho = 0.50$, $P < .001$). Automated correction showed similar results ($\rho = 0.91$, $P < .001$) and demonstrated very strong correlation with manual correction ($\rho = 0.98$, $P < .001$). Both correction methods reduced inflow-outflow variance, improving mean difference from –0.14 L/min (95% limits of agreement: –1.61, 1.32) (uncorrected) to 0.05 L/min (95% limits of agreement: –0.32, 0.42) (manually corrected) and 0.05 L/min (95% limits of agreement: –0.38, 0.49) (automatically corrected). There was no significant difference in inflow-outflow variance between manual and automated correction methods ($P = .10$).

Conclusion

Deep learning automated phase error correction reduced inflow-outflow bias and variance of volumetric flow measurements in four-dimensional flow MRI, achieving results comparable with manual image-based phase error correction.

3.2 Summary and Key Results

Summary

Deep learning-based background phase error correction improved the consistency of flow measurements in abdominopelvic four-dimensional flow MRI and simplified hemodynamic analysis for clinical use.

Key Results

- A deep learning algorithm trained with 99 abdominopelvic four-dimensional (4D) flow MRI examinations successfully generated phase error fields for automated correction.

- In an independent sample of 40 patients, flow measurements after deep learning correction had very strong correlation with manually corrected measurements (ρ = 0.98, $P < .001$).
- Automated correction reduced inflow-outflow bias and variance ($P < .001$), improving mean difference from –0.14 L/min uncorrected to 0.05 L/min deep learning corrected.

3.3 Introduction

The visual and quantitative assessment of abdominopelvic hemodynamics is essential in the evaluation of many clinical entities. In abdominal imaging, this is primarily undertaken with Doppler US and time-resolved two-dimensional phase-contrast MRI[90]. Abdominal US is limited by sonographic windows, but targeted windows can be applied to interrogate postoperative vascular complications of transplantation, renal artery stenosis, and other indications[91–93]. Because of the need to place precise imaging planes at the time of the scan, planar phase-contrast MRI is challenging to implement in the clinical environment but can be used to evaluate mesenteric ischemia, aortic dissections, and other vascular conditions [94,95]. Time-resolved three-dimensional (3D) phase-contrast MRI with three-directional velocity encoding (four-dimensional [4D] flow MRI) addresses these limitations by providing comprehensive imaging of the entire abdomen, allowing blood flow in any vessel to be retrospectively assessed in any direction[90,96,97].

While applications of 4D flow MRI have grown rapidly[31,33], the correction of magnetic eddy current–related background phase error remains a challenge[34–37]. Partial phase error correction can be achieved using pre-emphasis techniques[38], incorporation of gradient nonlinearity in the image reconstruction process[39], and field derivation and correction via Maxwell equations[40]; however, residual phase error may compromise the accuracy of 4D flow measurements[36,41]. Further phase error correction is therefore required (Fig 7). Current methods primarily address residual phase error through one of two approaches: stationary phantom imaging and polynomial regression of phase error in static soft tissues[41]. Phantom-based correction methods[98] require a second phantom scan after the patient scan with identical imaging parameters and are therefore impractical in a routine clinical setting[99]. Image-based correction[37,100] can use pixel-based velocity thresholding throughout the cardiac cycle but often requires a human operator for reliable segmentation of static soft tissues.

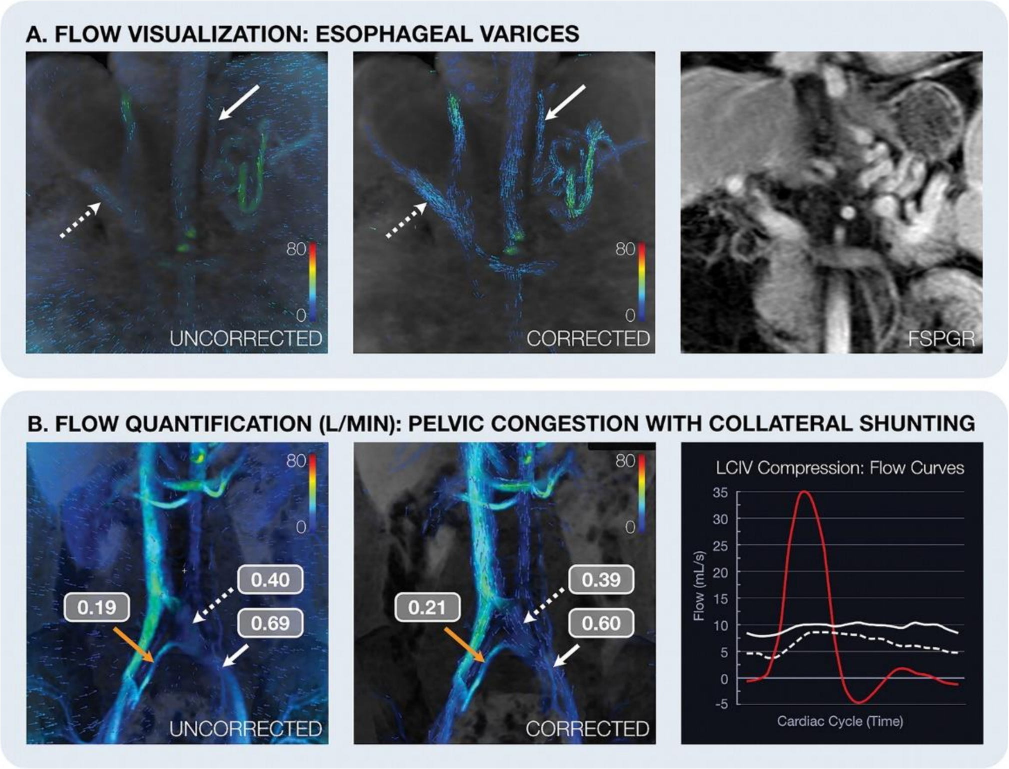

Figure 7: *Effect of background phase error correction on flow visualization and quantification.* **(A)** Coronal images in a 53-year-old man with cirrhosis and severe portal hypertension. Postcontrast four-dimensional (4D) flow MRI scans of the abdomen show portosystemic shunting through variceal vessels (solid arrows) that are difficult to discern prior to correction but are clearly seen after correction. The main portal vein (dashed arrows) is also better depicted. Adjacent anatomy is shown in the fast spoiled gradient echo (FSPGR) image. **(B)** Postcontrast 4D flow MRI scans in a 29-year-old woman with pelvic venous congestion, marked compression of the left common iliac vein (LCIV) under the right common iliac artery, and compensatory collateral flow connecting the LCIV to the right common iliac vein (RCIV). A large discrepancy in the amount of collateral flow (orange arrow) that passes to the RCIV is seen prior to correction. After correction, LCIV flow (0.60 L/min) is equal to the sum of flow within the compressed LCIV and the collateral vein (0.39 + 0.21 L/min). Line graph shows flow curves throughout one cardiac cycle for two locations in the LCIV, where right common iliac arterial flow (red line) suppresses venous return in the LCIV (dashed line and arrows). Venous flow in the LCIV before the collateral (solid line and arrows) remains unaffected.

Convolutional neural networks (CNNs) are an emerging class of deep learning techniques that have been used for classification, localization, and segmentation and have broad potential to further benefit medical image analysis[101]. Our objective was to develop a deep learning algorithm to generate phase error corrections without human intervention, simplifying the analysis and interpretation of abdominopelvic 4D flow acquisitions. We evaluated the feasibility of using a fully automated deep learning algorithm to perform image-based background phase error correction in 4D flow MRI and compared its effectiveness relative to manual image-based correction, applying inflow-outflow consistency as a principal benchmark of algorithm performance.

3.4 Materials and Methods

3.4.1 Patients

This study was compliant with the Health Insurance Portability and Accountability Act, and we obtained institutional review board approval, with waiver of informed consent. We retrospectively collected a convenience sample of 139 abdominopelvic 4D flow MRI acquisitions performed at our institution between January 2016 and July 2020 as part of routine clinical MRI examinations, which also included contrast-enhanced MR angiography and postcontrast fast spoiled gradient-echo imaging.

3.4.2 Data Acquisition

MRI examinations were performed on a 3-T MRI scanner (Discovery MR 750; GE Healthcare) using a 32-channel phased-array coil. Postcontrast 4D flow MRI was performed with a 3D cartesian strategy in which Ky-Kz samples were grouped in spiral-like sets and were acquired with golden angle ordering[102,103], evenly spaced over time[104] with dense central k-space sampling for respiratory soft gating[105]. Imaging parameters are summarized in Table 5. The 4D flow MRI scans were acquired as a coronal slab through the abdomen and pelvis, with the patient’s arms raised above his or her head to prevent soft-tissue wrapping in the right-left phase direction.

Table 5: *Imaging Parameters for Time-resolved 3D Phase-Contrast MRI with 3D Velocity Encoding*

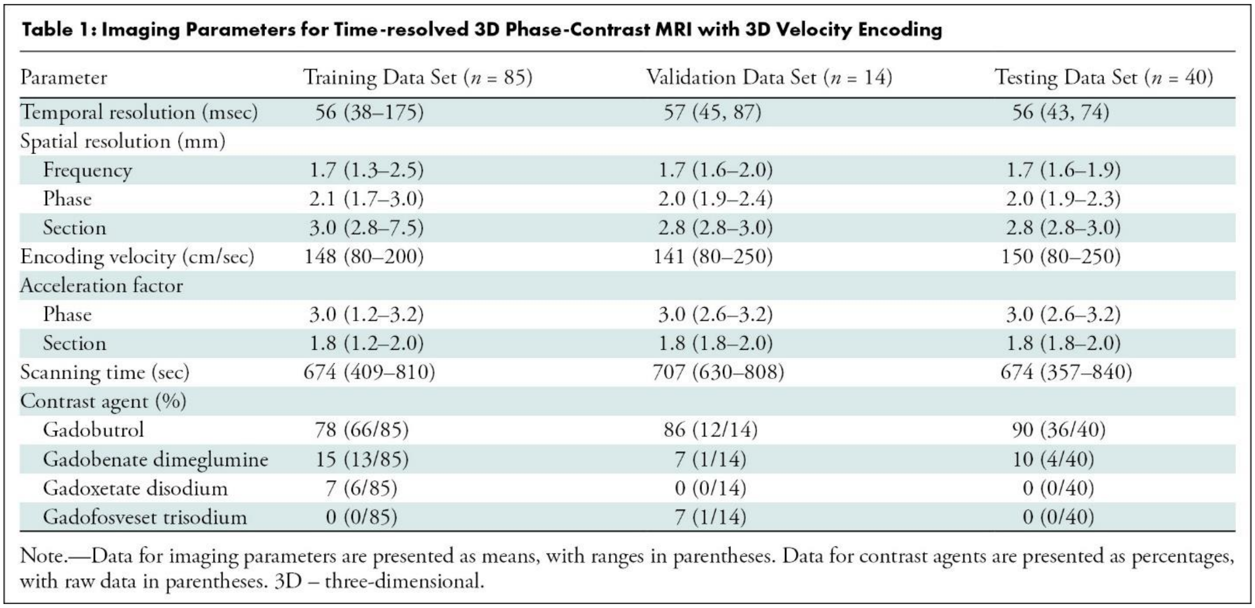

Table 1: Imaging Parameters for Time-resolved 3D Phase-Contrast MRI with 3D Velocity Encoding

Parameter	Training Data Set (*n* = 85)	Validation Data Set (*n* = 14)	Testing Data Set (*n* = 40)
Temporal resolution (msec)	56 (38–175)	57 (45, 87)	56 (43, 74)
Spatial resolution (mm)			
Frequency	1.7 (1.3–2.5)	1.7 (1.6–2.0)	1.7 (1.6–1.9)
Phase	2.1 (1.7–3.0)	2.0 (1.9–2.4)	2.0 (1.9–2.3)
Section	3.0 (2.8–7.5)	2.8 (2.8–3.0)	2.8 (2.8–3.0)
Encoding velocity (cm/sec)	148 (80–200)	141 (80–250)	150 (80–250)
Acceleration factor			
Phase	3.0 (1.2–3.2)	3.0 (2.6–3.2)	3.0 (2.6–3.2)
Section	1.8 (1.2–2.0)	1.8 (1.8–2.0)	1.8 (1.8–2.0)
Scanning time (sec)	674 (409–810)	707 (630–808)	674 (357–840)
Contrast agent (%)			
Gadobutrol	78 (66/85)	86 (12/14)	90 (36/40)
Gadobenate dimeglumine	15 (13/85)	7 (1/14)	10 (4/40)
Gadoxetate disodium	7 (6/85)	0 (0/14)	0 (0/40)
Gadofosveset trisodium	0 (0/85)	7 (1/14)	0 (0/40)

Note.—Data for imaging parameters are presented as means, with ranges in parentheses. Data for contrast agents are presented as percentages, with raw data in parentheses. 3D – three-dimensional.

3.4.3 Manual Background Phase Error Correction

Manual phase error correction was performed with dedicated imaging software (Arterys, version 26.7.6; Arterys) by two individuals (S.Y., a 4th-year medical student; A.H., a board-certified radiologist with more than 10 years of experience working with 4D flow MRI). Manual correction was performed via segmentation of static tissue followed by patchwise linear regression of static tissue velocities. Raw uncorrected and corrected velocity data were exported from the imaging software.

3.4.4 Data Preprocessing

After 40 examinations were reserved for testing, the remaining 1980 temporal volumes from 99 examinations were randomly divided by examination into two cohorts, with 86% (85 of 99) for training and 14% (14 of 99) for validation. Maxwell terms and gradient field nonlinearity were corrected in-line during the image reconstruction process[39,40]. After performing semiautomatic thresholding of magnitude images for exclusion of air pixels, velocity values corresponding to unexcluded pixels were used to generate a third-order polynomial regression of the manual correction. Velocities were scaled by the encoding velocity for each examination, and all data were downsampled to 64 × 64 × 64 cubes due to anticipated GPU memory limitations.

3.4.5 Neural Network Training

Our 3D multichannel U-Net[61], a type of CNN whose architecture is illustrated in Figure 8, was trained for 300 epochs using mean squared error loss, hyperbolic tangent activation, and Adam optimization with a learning rate of 1×10^{-4}. Network training used TensorFlow-GPU 2.1 (Google) on a workstation running Ubuntu 18.04 (Canonical) equipped with four Nvidia Quadro GV100 GPUs (Nvidia). CNN design and training were performed by two authors (S.Y.; E.M.M., a doctoral student in his 6th year of training). The code for the model architecture and training routine is available on request (release version 1.0; *https://github.com/AiDALabUCSD/Abdominal-Phase-Error-Correction*); GitHub login required).

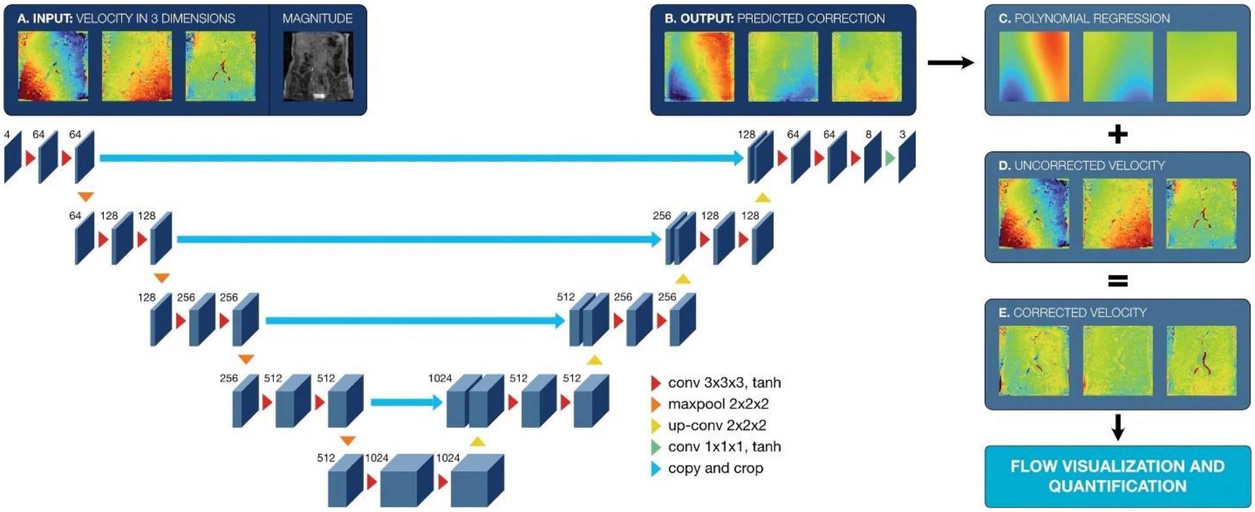

Figure 8: *Pipeline for automated phase error correction.* A three-dimensional (3D) multichannel U-Net (a type of convolutional neural network) designed with **(A)** four input channels, including flow velocities encoded in three cardinal directions and corresponding magnitude volumes, and **(B)** three output channels to infer corrections for the same three velocity components. Architecture of the 3D multichannel U-Net is shown, with numbers indicating the total number of channels, operations (arrowheads), and kernel sizes and activation functions indicated in the legend. As a postprocessing step, pixelwise inferred corrections are smoothed with least squares regression to a third-order polynomial in **(C)**. This correction is then added to the **(D)** original uncorrected data to generate **(E)** corrected flow data.

3.4.6 Polynomial Regression and Application

Pixelwise velocity corrections generated by the CNN were supplied as input to third-order polynomial least-squares regression after intensity thresholding for exclusion of air pixels. A single-phase error correction was generated for each examination, computed as the average of corrections generated for each of the 20 time points in the 4D flow time series. The fully automated postprocessing pipeline is shown in Figure 8.

3.4.7 Volumetric Flow Measurements

Segmentation of vessels for flow quantification was performed by two observers (S.Y., A.H.) for the infrarenal aorta in triplicate and individually for the left common iliac artery (LCIA) and right common iliac artery (RCIA), inferior vena cava, left common iliac vein (LCIV), and right common iliac vein (RCIV). The same manual segmentations were used for uncorrected, manually corrected, and automatically corrected data, such that measurements between the three data sets were spatially consistent.

3.4.8 Performance Evaluation

Internal consistency of flow measurements was established by assessing conservation of mass in the 40 test cases. The average of the three aortic measurements was compared with the sum of the LCIA and RCIA, while the inferior vena cava was compared with the sum of the LCIV and RCIV. Each arterial vessel was compared with its venous counterpart (aorta vs inferior vena cava, LCIA vs LCIV, and RCIA vs RCIV). A representative case from the test set is illustrated in Figure 9, showing the 24 total measurements per case.

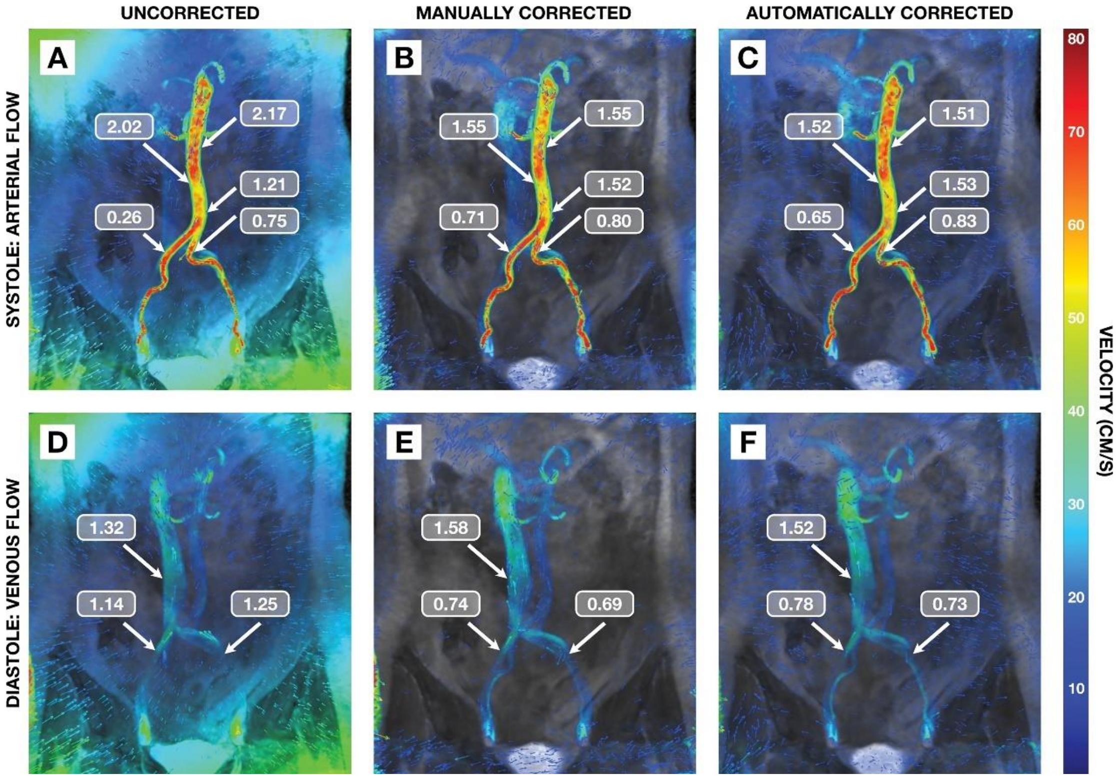

Figure 9: *Visual example of background phase error correction for four-dimensional flow MRI.* Images show visual and quantitative reduction of background phase error after manual or convolutional neural network (CNN)-based correction. **(A–C)** Coronal MRI scans of the aorta and common iliac arteries during peak systole. **(D–F)** Coronal MRI scans show the inferior vena cava and common iliac veins during mid-diastole. Flow velocity is represented by a color map ranging from blue (0 cm/sec) to red (80 cm/sec). For assessment of flow continuity, measurements (in liters per minute) were taken at multiple locations (arrows). Corrected velocity measurements showed improved consistency along the length of the infrarenal aorta and conservation of mass across bifurcations in the arterial and venous systems.

3.4.9 Statistical Analysis

For the 40 test cases, *t* tests were performed with a difference of zero as the null hypothesis for the five comparisons assessing conservation of mass and a type I error threshold of $P < .01$ ($\alpha = .05$ with Bonferroni correction for multiple comparisons). Additional statistical comparisons were performed using the Bartlett test of homoscedasticity[106] followed by pairwise *F* tests with Bonferroni correction. These analyses were performed in RStudio 1.3.959 (R Foundation for Statistical Computing).

Inflow-outflow consistency in the test set was further assessed using Pearson correlation and Bland-Altman analysis. The time required for manual versus automated correction was assessed using a *t* test. We fitted a single-rater two-way random effects intraclass correlation model[107] to assess absolute agreement between flow measurements made by two observers (S.Y., A.H.). These statistical analyses were performed using the Scipy 1.4.1 and Pingouin 0.3.12 libraries in Python (version 3.7.7; *https://www.python.org/*).

3.5 Results

3.5.1 Patient Characteristics

We retrospectively collected abdominopelvic 4D flow MRI examinations from 140 patients (mean age, 47 years ± 14 [standard deviation]; 108 women). Patient characteristics grouped by clinical indication are summarized in Table 6.

Table 6: *Patient Characteristics*

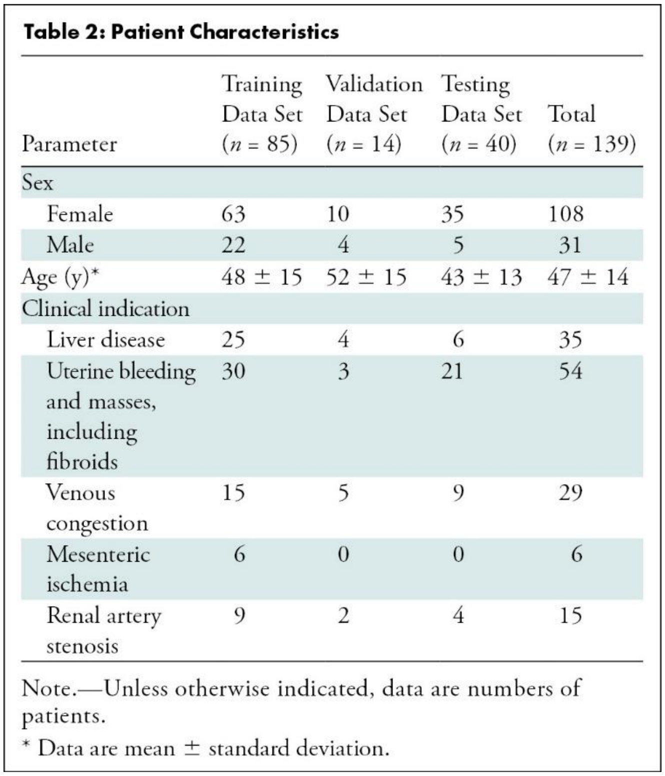

Table 2: Patient Characteristics

Parameter	Training Data Set (*n* = 85)	Validation Data Set (*n* = 14)	Testing Data Set (*n* = 40)	Total (*n* = 139)
Sex				
Female	63	10	35	108
Male	22	4	5	31
Age (y)*	48 ± 15	52 ± 15	43 ± 13	47 ± 14
Clinical indication				
Liver disease	25	4	6	35
Uterine bleeding and masses, including fibroids	30	3	21	54
Venous congestion	15	5	9	29
Mesenteric ischemia	6	0	0	6
Renal artery stenosis	9	2	4	15

Note.—Unless otherwise indicated, data are numbers of patients.

* Data are mean ± standard deviation.

3.5.2 Performance of Manual Phase Error Correction

Prior to background phase error correction, there was poor inflow-outflow consistency for comparison of arterial flow with venous flow and for comparison of blood flow before bifurcation with blood flow after bifurcation (Fig 9A, 9D). The mean absolute difference between flow measurements was 0.52 L/min ± 0.55 (standard deviation), while the mean percentage difference was 37% ± 26. Correlation between flow measurements was moderate ($\rho = 0.50$, $P < .001$).

After manual correction (Fig 9B, 9E), the mean absolute difference improved to 0.15 L/min ± 0.12, with a corresponding mean percentage difference of 14% ± 10.

Corrected flow measurements also demonstrated very strong correlation between inflow and outflow measurements ($\rho = 0.94$, $P < .001$).

3.5.3 Clinical Application of 4D Flow

In Figure 10, we highlight two example cases in which manually corrected 4D flow MRI was helpful for diagnosis.

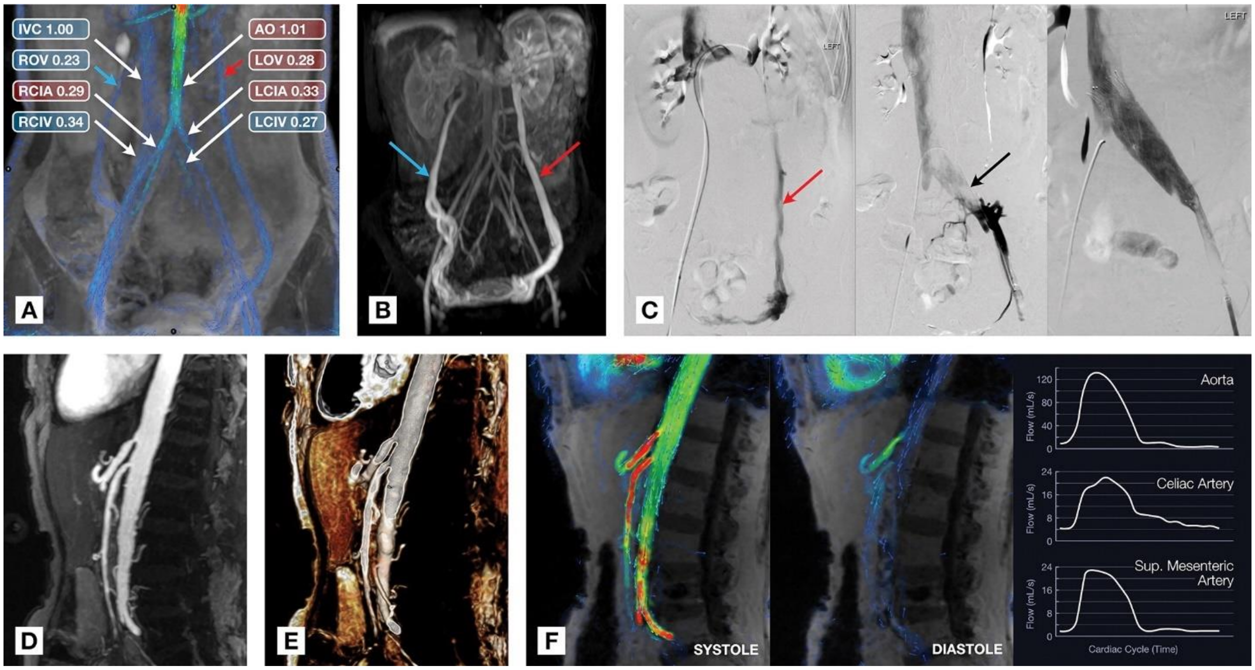

Figure 10: *Clinical applications of abdominopelvic four-dimensional (4D) flow MRI.* **(A–C)** Coronal oblique MRI scans obtained with postcontrast 4D flow MRI (**A**) and MR angiography (**B**) in a 24-year-old woman with Nutcracker syndrome and May-Thurner syndrome who had retrograde flow in an asymmetrically enlarged left ovarian vein (LOV) (red arrow) and antegrade flow in the enlarged contralateral ovarian vein (blue arrow). AO = aorta, IVC = inferior vena cava, LCIA = left common iliac artery, RCIA = right common iliac artery, RCIV = right common iliac vein, ROV = right ovarian vein. In **C,** both retrograde ovarian flow and left common iliac vein (LCIV) stenosis were confirmed during catheter angiography, with flow through the compressed LCIV (black arrow) being restored after stent placement. **(D–F)** Sagittal oblique images in an 89-year-old woman with a history of ischemic colitis and severe stenosis of the celiac artery and superior mesenteric artery at their origins, seen as focal vessel narrowing in the two-dimensional MR angiography image (**D**) and three-dimensional (3D) reconstruction (**E**). Postcontrast 4D flow MRI scan (**F**) shows similar narrowing and provides additional hemodynamic information: high flow velocity is shown in red, and persistent high-velocity flow in the celiac artery during diastole is reflected in the corresponding flow curves.

In the first example case (Fig 10A-10C), a 24-year-old woman with postural orthostatic tachycardia syndrome presented with orthostatic lightheadedness, left leg discomfort, and abdominopelvic pressure that worsened throughout the day. She underwent multisequence MRI, including differential subsampling with cartesian ordering [108], which demonstrated dilated ovarian veins bilaterally and filling of pelvic venous collaterals. Further evaluation with 4D flow MRI enabled us to confirm retrograde flow in the left ovarian vein (280 mL/min) and anterograde flow in the right ovarian vein (230 mL/min). There was absent flow in the left renal vein as it passed under the superior mesenteric artery, indicating nutcracker physiology. There was limited flow (270 mL/min) in the LCIV as it passed under the RCIA, which was inadequate to accommodate the retrograde ovarian venous flow, indicating May-Thurner venous insufficiency.

The patient subsequently underwent catheter venography, which enabled us to confirm left ovarian vein reflux and left iliac venous insufficiency. This was followed by LCIV stenting, resolution of May-Thurner venous insufficiency and left leg discomfort, and, later, left gonadal vein embolization with resolution of her abdominal bloating, urinary discomfort, and pelvic pain.

In a second example case (Fig 10D-10F), an 89-year-old woman with a history of ischemic colitis underwent abdominal MRI for evaluation of persistent abdominal pain and diarrhea. Quantitative flow measurements using two-dimensional phase-contrast MRI demonstrated limited augmentation of mesenteric blood flow after a prandial challenge[94], with flow through the superior mesenteric vein increasing from 299 to 330 mL/min and flow through the superior mesenteric artery increasing from 386 to 414 mL/min.

Postprandial 4D flow MRI measurements were obtained to assess the feasibility of using 4D flow in place of two-dimensional phase-contrast planes, and the 4D flow measurements were found to be similar to the two-dimensional phase-contrast flow measurements. We observed several additional findings on 4D flow MRI scans, including high-velocity systolic blood flow through the celiac (159.41 cm/sec) and superior mesenteric (136.33 cm/sec) arteries and prolonged diastolic forward flow through the stenotic celiac artery (Fig 10F). Taken together, these findings are consistent with hemodynamically significant celiac and superior mesenteric artery stenosis and chronic mesenteric ischemia.

3.5.4 Performance of Automated Phase Error Correction

Neural network inference required a mean of 0.54 second ± 0.01 per case, while postprocessing required a mean of 11.75 seconds ± 0.61 per case. The mean total time for automated phase error correction was 12.29 seconds ± 0.61 compared with manual phase error correction performed by the most experienced observer (A.H.), which required 152.3 seconds ± 52.58 per case ($P < .001$).

The multichannel 3D U-Net led to an improvement in inflow-outflow consistency comparable to that of manual correction, with strong correlation between flow measurements ($\rho = 0.91$, $P < .001$). The average standard deviation for the three aortic measurements performed for each case was 0.07 L/min, compared with 0.07 L/min after manual correction and 0.23 L/min for uncorrected cases. The CNN algorithm was successfully executed in all 40 test cases, resolving phase error in all three principal directions (Fig 11). There were no technical failures.

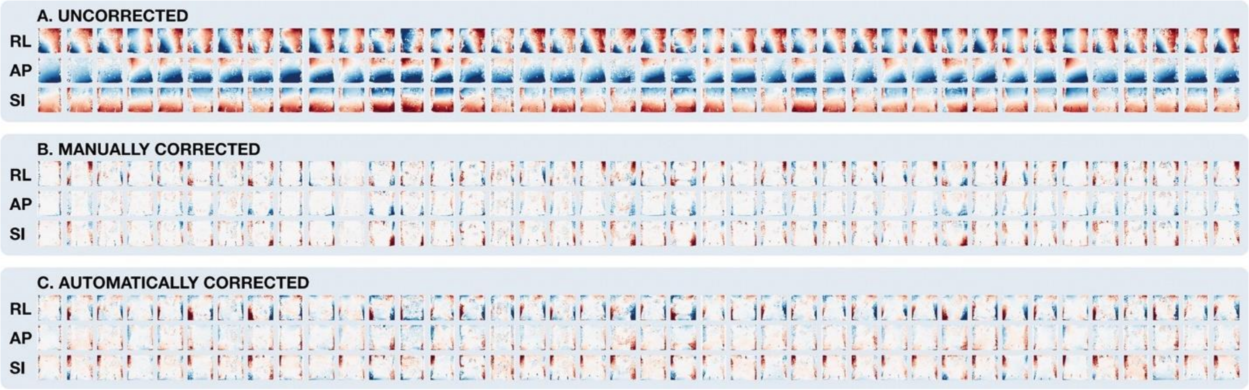

Figure 11: *Representative coronal sections of MRI scans from all 40 test cases.* With velocity shown on a red-white-blue color scale, manual and automated correction methods show a similar reduction of soft-tissue phase error, seen as primarily white coloring (zero flow). Phase errors for each cardinal direction appear to follow fairly consistent patterns but with slight differences from case to case. AP = anterior to posterior, RL = right to left, SI = superior to inferior.

A direct comparison of flow measurements obtained using manual and automated correction demonstrated very strong correlation ($\rho = 0.98$, $P < .001$) (Fig 12A).

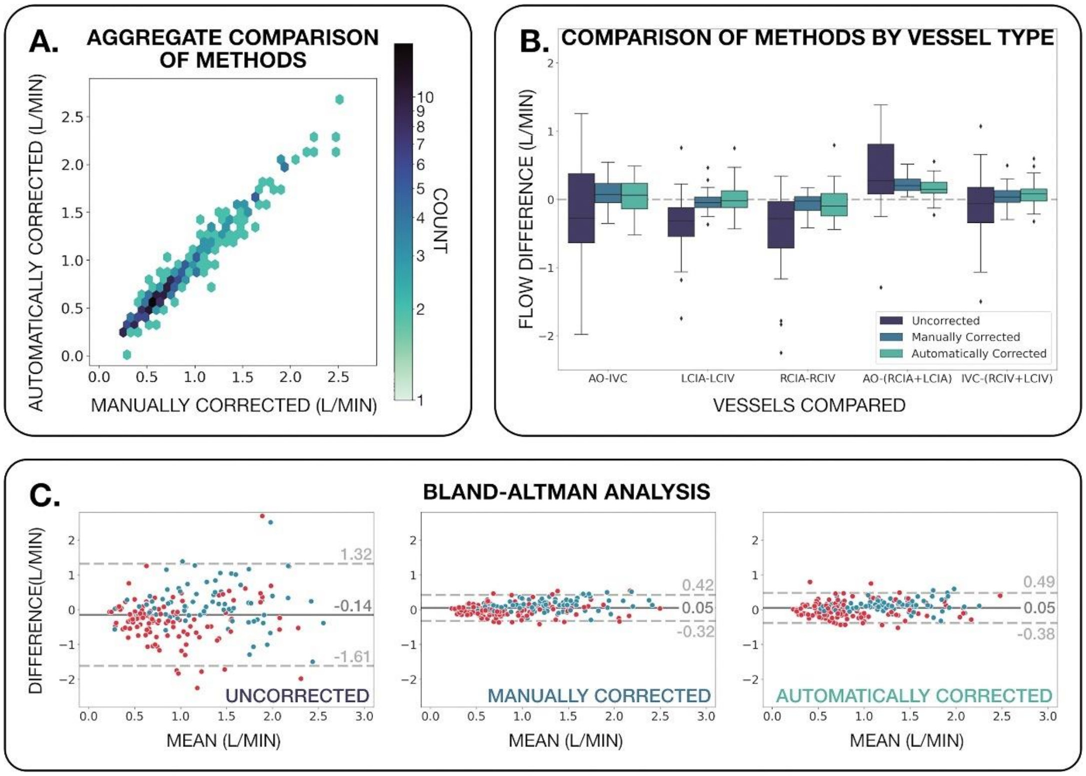

Figure 12: *Analysis of volumetric flow continuity in the testing data set (40 examinations).* **(A)** Panel shows a comparison of all manually and automatically corrected flow measurements. The slope of the regression is 1.01, and the correlation coefficient is 0.98. **(B)** Box-and-whisker plot grouped by vessel type compares uncorrected, manually corrected, and automatically corrected flow differences among the five vessel comparisons. Compared with uncorrected measurements, manually and automatically corrected measurements show an overall reduction in range, with mean values closer to zero. AO = aorta, IVC = inferior vena cava, LCIA = left common iliac artery, LCIV = left common iliac vein, RCIA = right common iliac artery, RCIV = right common iliac vein. **(C)** Bland-Altman plots with comparisons of arterial and venous flow (red) and comparisons of flow before and after bifurcation (blue) show greater flow consistency with narrower limits of agreement after both manual and automated correction.

The multichannel 3D U-Net achieved an average difference between vessel measurements of 0.05 L/min overall (*P* < .001), an improvement over uncorrected measurements, which had an average difference of –0.14 L/min overall (*P* = .01). In comparison, manual correction had an average difference of 0.05 L/min (*P* < .001). When considering only comparisons of arterial flow versus venous flow, both correction methods showed marked improvement over uncorrected data, with mean differences of –0.005

L/min (*P* = .79) after manual correction and –0.003 L/min (*P* = .89) after automated correction compared with –0.35 L/min for uncorrected data (*P* < .001). Comparisons between pre- and postbifurcation flow also showed an improvement in mean difference from 0.17 L/min uncorrected to 0.14 L/min manually corrected and 0.13 automatically corrected, though the mean difference remained greater than zero for both correction methods (*P* = .02 for uncorrected, *P* < .001 for manually corrected, *P* < .001 for automatically corrected). Uncorrected data demonstrated a mean difference significantly different from zero for three of the five vessel comparisons (*P* < .001 for the difference between the LCIA and LCIV, the difference between the RCIA and RCIV, and the difference between the aorta and the sum of the RCIA and LCIA, while manually and automatically corrected vessel comparisons were significantly different from zero (*P* < .001 and *P* < .001, respectively) for only the difference between the aorta and the sum of the RCIA and LCIA (Table 7, Fig 12B).

Table 7: *Effect of Manual and Deep Learning-based Automated Phase Error Correction on Inflow-Outflow Consistency for Five Vessel Comparisons*

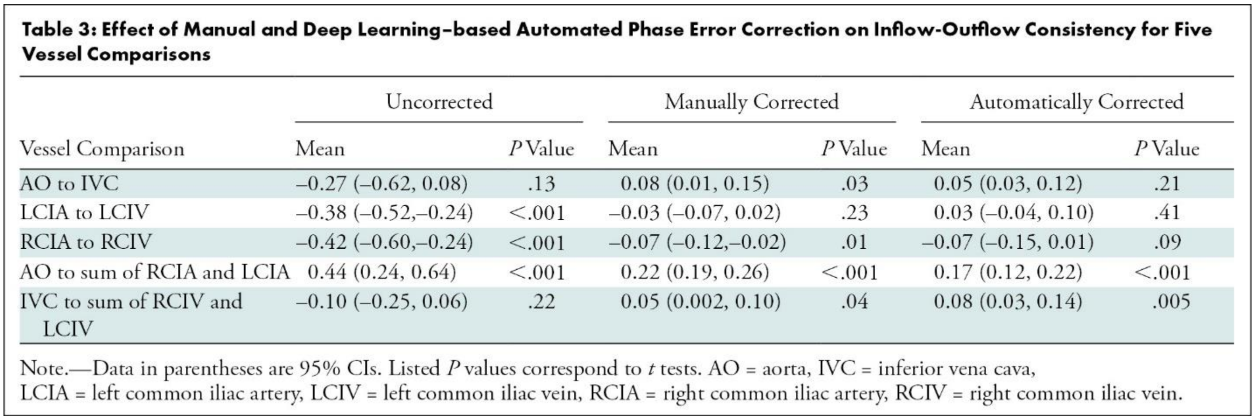

Table 3: Effect of Manual and Deep Learning–based Automated Phase Error Correction on Inflow-Outflow Consistency for Five Vessel Comparisons

	Uncorrected		Manually Corrected		Automatically Corrected	
Vessel Comparison	Mean	*P* Value	Mean	*P* Value	Mean	*P* Value
AO to IVC	–0.27 (–0.62, 0.08)	.13	0.08 (0.01, 0.15)	.03	0.05 (0.03, 0.12)	.21
LCIA to LCIV	–0.38 (–0.52,–0.24)	<.001	–0.03 (–0.07, 0.02)	.23	0.03 (–0.04, 0.10)	.41
RCIA to RCIV	–0.42 (–0.60,–0.24)	<.001	–0.07 (–0.12,–0.02)	.01	–0.07 (–0.15, 0.01)	.09
AO to sum of RCIA and LCIA	0.44 (0.24, 0.64)	<.001	0.22 (0.19, 0.26)	<.001	0.17 (0.12, 0.22)	<.001
IVC to sum of RCIV and LCIV	–0.10 (–0.25, 0.06)	.22	0.05 (0.002, 0.10)	.04	0.08 (0.03, 0.14)	.005

Note.—Data in parentheses are 95% CIs. Listed *P* values correspond to *t* tests. AO = aorta, IVC = inferior vena cava, LCIA = left common iliac artery, LCIV = left common iliac vein, RCIA = right common iliac artery, RCIV = right common iliac vein.

Manual and automated correction methods also demonstrated a reduction in variance of volumetric flow differences, with overall mean difference as follows: –0.14 L/min (95% limits of agreement: –1.61, 1.32) for uncorrected data, 0.05 L/min (95% limits of agreement: –0.32, 0.42) for manually corrected data, and 0.05 L/min (95% limits of agreement: –0.38, 0.49) for automatically corrected data (Fig 12C). The Bartlett test of homogeneity of variances yielded an overall *P* < .001, and pairwise *F* tests with Bonferroni correction demonstrated no significant difference between manual and automated correction (*P* < .001 for manually corrected vs uncorrected data, *P* < .001 for automatically corrected vs uncorrected data, *P* = .10 for manual vs automatically corrected data).

Analysis of interobserver variability demonstrated excellent reliability both before and after background phase error correction. The intraclass correlation coefficient prior to correction was 0.94 (*P* < .001). Manual and automated correction methods each improved the coefficient to 0.99 (*P* < .001 for both).

3.6 Discussion

Four-dimensional (4D) flow MRI has become increasingly valuable in the qualitative and quantitative assessment of blood flow. Since all measurements can be retrospectively obtained after image acquisition without the need for targeted US windows or placement of two-dimensional phase-contrast planes at the time of the examination, 4D flow MRI provides versatility that can be essential in the diagnostic process. However, the correction of magnetic eddy current–related background phase error remains a challenge in abdominal applications.

In this study, we demonstrated the feasibility of automating background phase error correction using a multichannel 3D U-Net, with improved consistency in comparisons of arterial and venous flow as well as in comparisons of blood flow before and after bifurcations. In a test set of 40 patients, automated phase error correction demonstrated very strong correlation with manually corrected measurements (ρ = 0.98, $P < .001$). Inflow-outflow bias and variance were also reduced, with mean difference and limits of agreement improving from –0.14 L/min (95% limits of agreement: –1.61, 1.32) (uncorrected) to 0.05 L/min (95% limits of agreement: –0.38, 0.49) (automatically corrected) and no significant difference in variance between manual and automated correction methods (P = .10, F test with Bonferroni correction).

Performance of manual correction requires substantial time and expertise due to the need for manual vessel segmentation. Previous studies[41,109] have explored the effect of various parameters on the accuracy of image-based phase error correction, including the signal-to-noise ratio of the data itself, the percentage of stationary tissue used in the regression, and the spatial order of the regressed correction. In general, the quality of the correction decreases with decreasing percentage of static tissue, which means that manual tissue segmentation requires a delicate balance between excluding as many vessels as possible and maximizing inclusion of soft tissue. This deterioration is increasingly pronounced with regressions of higher spatial order; in fact, third- and sometimes second-order polynomial regressions are frequently rendered impossible due to insufficient soft-tissue selection. CNNs are able to overcome this limitation because they learn relevant features of input images on their own.

Our study had limitations. First, our training and testing data were sourced using one MRI scanner from one vendor at one institution. Second, because many of our patients underwent 4D flow MRI for clinical evaluation of venous abnormalities, low encoding velocity (usually 80 cm/sec) created velocity aliasing within some high-flow arteries, limiting our ability to accurately measure blood flow in some vessels. Although we did not evaluate the potential of CNNs to correct for velocity aliasing, it is plausible that they might be applied similarly for this purpose as well. Finally, performance evaluation of our neural network relied on inflow-outflow consistency in major abdominal vessels. We did not assess whether detection of intraabdominal shunts was impaired or improved with phase error correction, instead focusing primarily on the feasibility of using a CNN to perform this correction.

In conclusion, correction of background phase offset poses a challenge to the clinical application of four-dimensional (4D) flow MRI but can be accomplished using a single multichannel three-dimensional U-Net, a type of convolutional neural network (CNN). We expect that similar results may be possible for other body territories, scanners, vendors, and institutions, which might be the subject of future investigations. This could be accomplished by retraining the CNN using new 4D flow data sets or by using transfer learning to expand the generalizability of this CNN. Our proof-of-concept study demonstrates the feasibility of automating phase error correction, bypassing the segmentation that is generally required for manual correction. In essence, we have trained a CNN to perform a complex task, simultaneously capturing the phase error in static soft tissue while ignoring flowing blood in the arterial and venous systems. The feasibility of this work highlights the untapped potential of CNNs to accomplish complex visual and computational tasks that may not be readily performed by humans and may help bring advanced imaging technologies, including 4D flow MRI, into routine clinical care.

3.7 Acknowledgements

We acknowledge Microsoft AI for Health for computational resources used for CNN training. E.M.M. is supported by a predoctoral fellowship from the American Heart Association and the University of California San Diego Medical Scientist Training Program (NIH/NIHGMS T32GM007198). S.Y. is supported by the Altman Clinical and Translational Research Institute MedGap Program.

This chapter was adapted, in part, from “Deep Learning Automated Background Phase Error Correction for Abdominopelvic 4D Flow MRI” in Radiology (2021). The author list is: You, Sophie*; Masutani, Evan*; Alley, Marcus; Vasanawala, Shreyas; Taub, Pam; Liau, Joy; Roberts, Anne; Hsiao, Albert. *Denotes co-first authorship. The dissertation author was the co-first investigator and co-first author of this paper.

Chapter 4: Feasibility of Deep Learning to Synthesize Outflow Hemodynamics from Cardiac MRI

4.1 Abstract

Purpose

Convolutional neural networks (CNNs) have proven valuable for segmentation and localization of anatomical structures on cardiac MRI. However, CNNs have potential to extrapolate beyond these straightforward visual tasks. We hypothesized that a CNN might be capable of inferring left ventricular outflow hemodynamics from cine SSFP images obtained during routine cardiac MRI.

Materials and Methods

Conventional and 4D Flow MRI acquisitions were retrospectively collected from 139 patients. We devised a novel CNN, Triton-Net, to synthesize the blood flow velocity field, while concurrently segmenting ventricular chambers and localizing cardiac landmarks. To evaluate technical performance of Triton-Net, segmentation and localization were compared against manual annotation; synthesized flow fields were compared against 4D Flow. As a clinical proof-of-concept, the algorithm was evaluated for its ability to detect left ventricular hypertrophy and predict outflow gradient >25 mmHg in an independent test set of 50 patients, measuring area under the receiver operating characteristic curve (AUROC).

Results

Median Dice of cardiac chamber segmentation ranged from 0.80–0.92, while median localization error of valve and apex positions ranged from 3.14–4.45 mm. Synthesized flow fields significantly correlated with 4D Flow ($p<0.001$, Wald test) with

median root-mean-squared-error from 136–252 mm/s. AUROC for detection of hypertrophy and outflow gradient were 0.863 and 0.830, respectively.

Conclusion

Triton-Net can perform multiple concurrent tasks, notably inference of left ventricular outflow hemodynamics directly from anatomic images, without separate acquisition of flow-sensitive MRI sequences. CNNs can infer cardiovascular fluid-mechanical relationships from routine cardiac MR images and may be applied for retrospective analysis of historical cardiac MRI exams.

4.2 Summary and Key Results

Summary

We demonstrate feasibility of a convolutional neural network named Triton-Net to synthesize intracardiac blood flow fields from SSFP MRI anatomic images and illustrate its clinical potential for hypertrophic cardiomyopathy and aortic stenosis.

Key Results

1. Triton-Net can synthesize intraventricular flow fields from anatomic images, which are correlated with 4D Flow MRI measurements ($p < 0.001$, Wald test).
2. The trifurcated architecture of Triton-Net enables concurrent cardiac segmentation and landmark localization to facilitate automated measurement of myocardial wall thickness.
3. Triton-Net outputs accurately classified elevated outflow pressure gradients (AUROC = 0.830) and hypertrophy (AUROC = 0.863), suggesting its ability to autonomously detect outflow stenosis and assist diagnostic interpretation.

4.3 Introduction

Cardiac MRI is a versatile imaging technique for assessment of anatomy and function[90,110–112]. Cine balanced steady-state free precession (SSFP) forms the backbone of cardiac MRI and is the standard for quantification of cardiac function[111] and morphology. A newer technique, 4D Flow MRI, is increasingly used to assess hemodynamics[113] to guide management and surgical correction of structural heart diseases[25]. For example, diseases like hypertrophic cardiomyopathy (HCM) and aortic stenosis (AS) exhibit structural abnormalities and benefit from hemodynamic assessment[114]. HCM is a relatively common inherited disease[115] associated with left ventricular outflow tract (LVOT) obstruction and can contribute to sudden cardiac death[116]. Septal reduction therapy is indicated for patients with outflow pressure gradients ≥50 mmHg[117]. Similarly, patients with AS are assessed with a combination of anatomic and hemodynamic parameters, usually with echocardiography, including aortic valve area and transvalvular pressure gradient. Symptomatic patients with untreated severe AS can have a >50% 2-year mortality rate.[118] While 4D Flow MRI has potential to assist in assessing hemodynamic severity to complement traditional Cine SSFP imaging, it requires acquisition of a separate specialized pulse sequence, advanced technical expertise, and is not yet widely available[43].

Over the last several years, convolutional neural networks (CNNs) have proven valuable for automating multiple visual tasks, including segmentation and localization of anatomic landmarks and cardiac chambers, and are progressively being integrated into clinical workflows[119,120]. Multiple groups have shown that CNNs can approach radiologist-level performance for ventricular segmentation[10,121] and landmark localization[62,122]. While there has been significant progress for these visual tasks, CNNs have untapped potential to extrapolate beyond structural identification. Recent work has hinted at the ability of CNNs to learn dynamic features to perform more complex tasks such as direct regression of ventricular function[123,124], synthesis of high frequency spatial information[125], and computation of pixel image velocimetry[126]. We hypothesized that in the same vein, we could develop a CNN to learn cardiovascular fluid-mechanical relationships and synthesize intracardiac blood flow fields from Cine SSFP images commonly obtained during cardiac MRI. In doing so, we might provide hemodynamic data, which otherwise would require a dedicated 4D Flow MRI acquisition.

To undertake this problem, we designed a novel three-pronged CNN, which we call Triton-Net, to concurrently perform multiple complementary tasks – cardiac chamber segmentation, landmark localization and synthesis of the intracardiac blood flow field. This CNN was then trained using our historical database of 4D Flow MRI examinations, which provided pixelwise ground truth vector fields for Triton-Net training and evaluation.

4.4 Materials and Methods

4.4.1 Patients and Image Data

Our study was performed with institutional review board approval and waiver of written informed consent. We retrospectively collected a convenience sample of 139 cardiac MRI exams that included 3-chamber Cine SSFP and 4D Flow as part of the clinical exam at our institution between December 2017 to May 2021. On a per patient basis, exams were divided 64% for training (89/139 examinations) and 36% for independent testing (50/139 examinations). We specifically enriched our testing set to contain patients with elevated outflow gradient i.e., peak pressure gradient exceeding 25 mmHg at the AV or LVOT, and randomly allocated the remainder of patients. Of the 50 patients in the test set, 7 had aortic stenosis, 8 had hypertrophic cardiomyopathy, and 1 had subaortic stenosis due to subaortic membrane (Fig 13). The remaining 34 patients in the test set did not have stenosis of the LVOT or aortic valve.

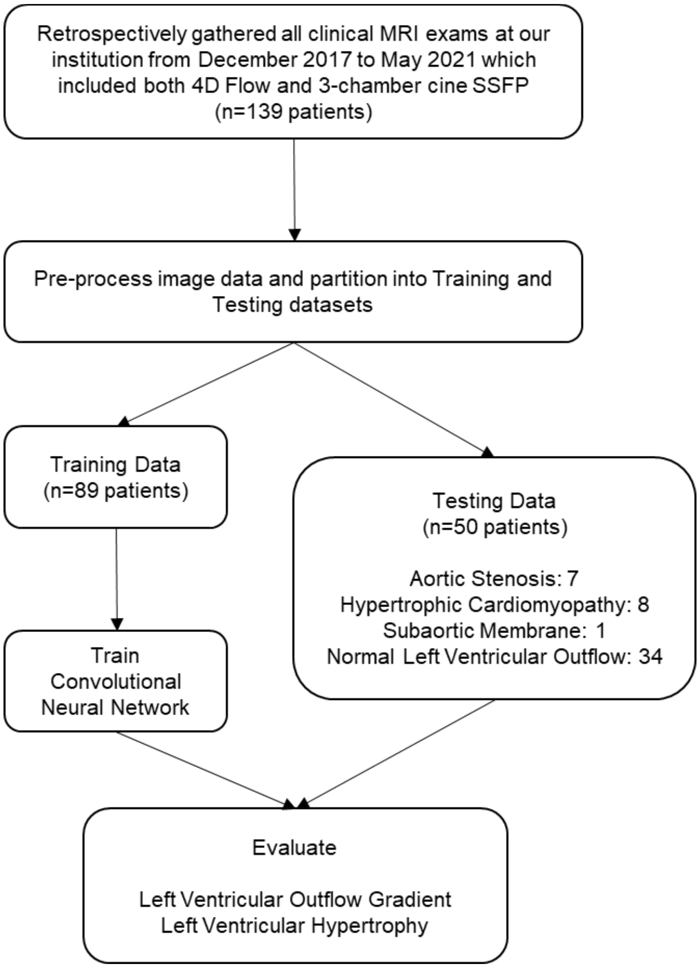

Figure 13: *Patient Population Flowchart*

All 4D Flow MRI examinations were performed following administration of intravenous gadolinium contrast (gadobenate dimeglumine, 0.15 mmol/kg) and employed respiratory self-navigation, iterative compressed-sensing, and parallel imaging reconstruction[127]. From the same set of exams, we collected 231 concurrently performed

3-chamber cine SSFP series. All studies were performed with a 3.0-T MRI scanner (Discovery MR750 DV26; GE Healthcare) with a standard 32-channel phased-array coil (Table 8).

Table 8: *MRI Scanner Parameters.* Data are means, with ranges in parentheses. VENC = Velocity encoding

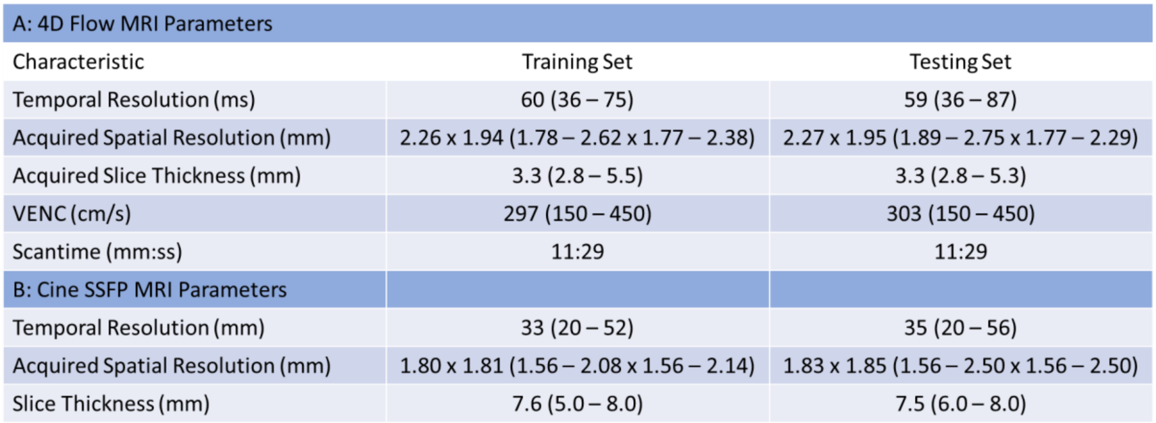

A: 4D Flow MRI Parameters		
Characteristic	Training Set	Testing Set
Temporal Resolution (ms)	60 (36 – 75)	59 (36 – 87)
Acquired Spatial Resolution (mm)	2.26 x 1.94 (1.78 – 2.62 x 1.77 – 2.38)	2.27 x 1.95 (1.89 – 2.75 x 1.77 – 2.29)
Acquired Slice Thickness (mm)	3.3 (2.8 – 5.5)	3.3 (2.8 – 5.3)
VENC (cm/s)	297 (150 – 450)	303 (150 – 450)
Scantime (mm:ss)	11:29	11:29
B: Cine SSFP MRI Parameters		
Temporal Resolution (mm)	33 (20 – 52)	35 (20 – 56)
Acquired Spatial Resolution (mm)	1.80 x 1.81 (1.56 – 2.08 x 1.56 – 2.14)	1.83 x 1.85 (1.56 – 2.50 x 1.56 – 2.50)
Slice Thickness (mm)	7.6 (5.0 – 8.0)	7.5 (6.0 – 8.0)

4.4.2 Image Annotation

Image annotation and registration of 4D Flow and Cine SSFP images were performed using in-house software developed in Python by the lead author, a 5th-year MD-PhD student (E.M.M.). The lead author and a 3rd year diagnostic radiology resident (T.A.R.) manually annotated all 3-chamber cine SSFP series under the supervision of a cardiovascular radiologist with 12 years of experience in cardiac MRI (A.H.). For cardiac chamber segmentation and landmark localization, we generated 1) segmentations of the left atrium, left ventricular blood pool, left ventricular myocardium, right ventricular blood pool, aortic root and 2) marked locations for the mitral valve, aortic valve, and apex.

4.4.3 Triton-Net: A Multi-Prong Neural Network

Triton-Net is a novel three-pronged CNN (Fig 14). It simultaneously performs: 1) localization of anatomical landmarks, 2) segmentation of cardiac chambers, and 3) synthesis of blood flow fields. Triton-Net takes as input five adjacent timeframes from 3-

chamber cine SSFP series, which are passed into an encoder-decoder block based on the 3D-UNet architecture[61], which are then temporally condensed into a single-timeframe feature map (Supplemental Figure 3). This shared feature map is then passed into three output prongs, each comprising a squeeze-excitation block and shallow sub-CNN based on the SRNet architecture[128] to infer chamber segmentations, landmark localizations, and intracardiac blood flow fields. The synthesized blood flow fields comprise pixel-wise inferences of velocity in the x and y directions. Training data were standardized by performing in-plane rotation. Training data was augmented with -5° and 5° degree in-plane rotations. Additional details of CNN training can be found in the Chapter Appendix Text.

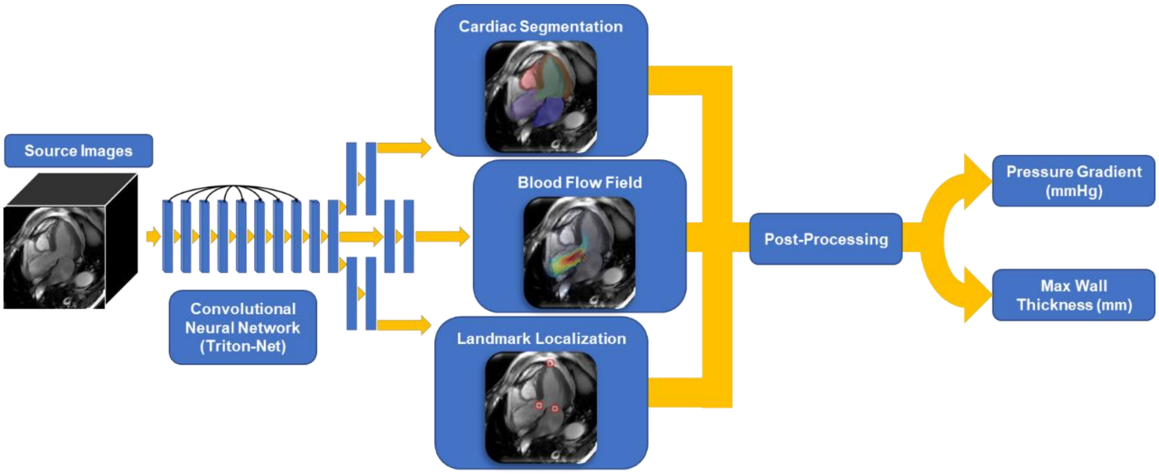

Figure 14: *Triton-Net: A three-pronged, spatiotemporal multitask convolutional neural network.* A multitask deep convolutional neural network named Triton-Net accomplishes three related component tasks from source 3-chamber cine SSFP cardiac MR images: 1) segmentation of cardiac chambers, 2) localization of anatomical landmarks, and 3) synthesis of blood flow fields. These inferences are post-processed to generate measurements of maximal left ventricular wall thickness and peak left ventricular outflow tract pressure gradient.

4.4.4 Evaluation of Performance

To evaluate the clinical utility of Triton-Net for outflow obstruction, CNN inferences were used to compute estimates for outflow gradients and maximum wall thicknesses.

Peak pressure gradients were calculated using the modified Bernoulli equation, $\Delta P = 4v^2$, where v is the peak speed. Gradients exceeding 25 mmHg were considered significant. Left ventricular wall thickness was calculated by defining the mitral valve-apex axis and slicing the end-diastolic myocardial mask orthogonally to this axis. Ground truth values were derived in the same manner using manual annotations and 4D Flow MRI data.

4.4.5 Statistical Analysis

All statistical analyses were performed on the independent test set. We evaluated the ability of Triton-Net to perform multi-class segmentation by calculating the Sorenson-Dice coefficient between inferred and annotated ground truth masks. For the evaluation of multi-landmark localization performance, we calculated the Euclidean distance between the inferred and annotated ground truth landmark coordinates. We report the first, second, and third quartiles for Dice coefficients and Euclidean distances.

To evaluate correlation between synthesized and ground truth blood flow fields, we performed pixel-wise calculation of Pearson correlation. Additionally, we reported the per-frame root-mean-squared-error between synthesized and ground truth flow fields for each chamber. To assess effectiveness of the CNN-derived classifications of outflow stenosis and myocardial hypertrophy, we generated Receiver-Operating Characteristic curves by comparing inferred and ground-truth values and report the area under the receiver operating characteristic curve (AUROC).

Statistical analysis was performed using Python (version 3.7, Python Software Foundation, Wilmington, Del), NumPy, SciPy, scikit-learn, and Excel (Microsoft, Redmond, Wash). Statistical significance of correlation between inferred and ground truth values was assessed using the Wald test with type I error threshold of 0.05.

4.5 Results

4.5.1 Patient Characteristics

For CNN development and evaluation, we retrospectively collected 139 4D Flow MRI series and 243 corresponding 3-chamber cine SSFP series from 139 patients (mean age, 51 years ± 18; 66 female). MRI exams from 50 patients were reserved for independent testing of the CNN algorithm. Of the patients in the independent test set, 64% had myocardial wall thickness greater than 15 mm and 32% had left ventricular outflow peak gradient exceeding 25 mmHg.

4.5.2 Chamber Segmentation and Landmark Localization

On aggregate, we observed strong overlap between inferred and ground truth segmentations as assessed by the Dice coefficient (Fig 15C).

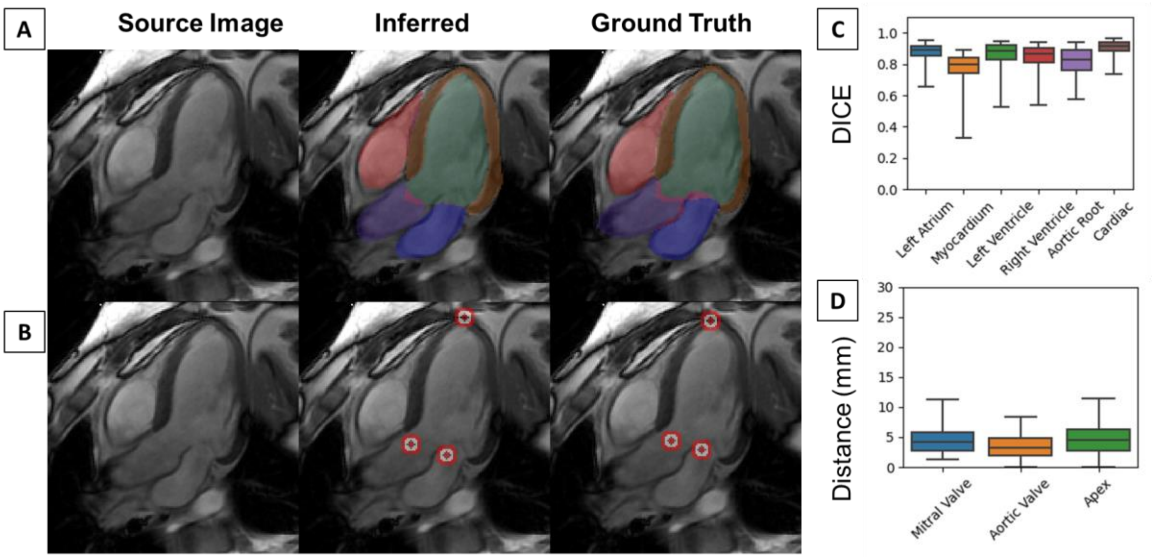

Figure 15: *Performance of the segmentation and localization prongs of Triton-Net.* A) Representative multi-chamber cardiac segmentation and B) multi-landmark localization in a morphologically normal 41 year-old female. Left atrium (blue), left myocardium (orange), left ventricular blood pool (green), right ventricle (red), and aortic root (purple) shown. Bullseyes at mitral valve, aortic valve, and apex. Box-and-whisker plots show aggregate C) segmentation performance based on the Sorenson-Dice coefficient and D) localization performance based on distance from ground truth annotations (D) (n = 1780 slices from testing set). Boxes encapsulate interquartile ranges, whiskers demarcate the central 95% of data points, and black bars lie on the median.

Median Dice coefficients (with 1st and 3rd quartiles in parentheses) for each chamber were 0.89 (0.85 – 0.92) for the left atrium, 0.80 (0.74 – 0.84) for the left myocardium, 0.89 (0.83 – 0.92) for the left ventricular blood pool, 0.87 (0.81 – 0.90) for the right ventricle, and 0.83 (0.76 – 0.89) for the aortic root (Table 9). We measured similarly strong aggregate performance for landmark localization as assessed by Euclidean distance between inferred and annotated positions (Fig 15D). Median distances in millimeters (with 1st and 3rd quartiles in parentheses) for each landmark were 4.20 (2.80 – 5.80) for the mitral valve, 3.14 (1.99 – 4.84) for the aortic valve, and 4.45 (2.81 – 6.30) for the apex.

We present a representative case of chamber segmentation (Fig 15A) and landmark localization (Fig 15B) in a morphologically normal 41-year-old female. For this case, the left atrium, left ventricular blood pool, left myocardium, right ventricle, and aortic root showed good agreement between the inferred and ground truth segmentations. Likewise, we found concurrence between Triton-Net and annotated localizations of the mitral valve, aortic valve, and apex. To show further agreement between inferred and annotated segmentations over the cardiac cycle, we track the predicted and ground truth areas for each chamber for this exemplar case (Supplemental Video 1).

Table 9: *Performance of Triton-Net Multi-Chamber Segmentation and Multi-Landmark Localization.* Data are medians, with first and third quartiles in parentheses.

A: Triton-Net Segmentation Performance	DICE
Left Atrium	0.89 (0.85 – 0.92)
Left Myocardium	0.80 (0.74 – 0.84)
Left Ventricle	0.89 (0.83 – 0.92)
Right Ventricle	0.87 (0.81 – 0.90)
Aortic Root	0.83 (0.76 – 0.89)
Cardiac Mask	0.92 (0.88 – 0.94)
B: Triton-Net Localization Performance	Distance (mm)
Mitral Valve	4.20 (2.80 – 5.80)
Aortic Valve	3.14 (1.99 – 4.84)
Apex	4.45 (2.81 – 6.30)

4.5.3 Intracardiac Blood Flow Field Synthesis

Triton-Net showed an ability to synthesize intracardiac blood flow fields from two-dimensional time series, provided only image data from the 3-chamber view. Quantitatively, on a pixel-wise basis Triton-Net showed significant correlation between synthesized and ground-truth velocities (Fig 16B), with slightly stronger correlation of synthesized flow fields along the major axis ($p<0.001$, $\rho=0.57$, slope=0.75) than minor axis ($p<0.001$, $\rho=0.57$, slope=0.78) of the left ventricle (Table 10).

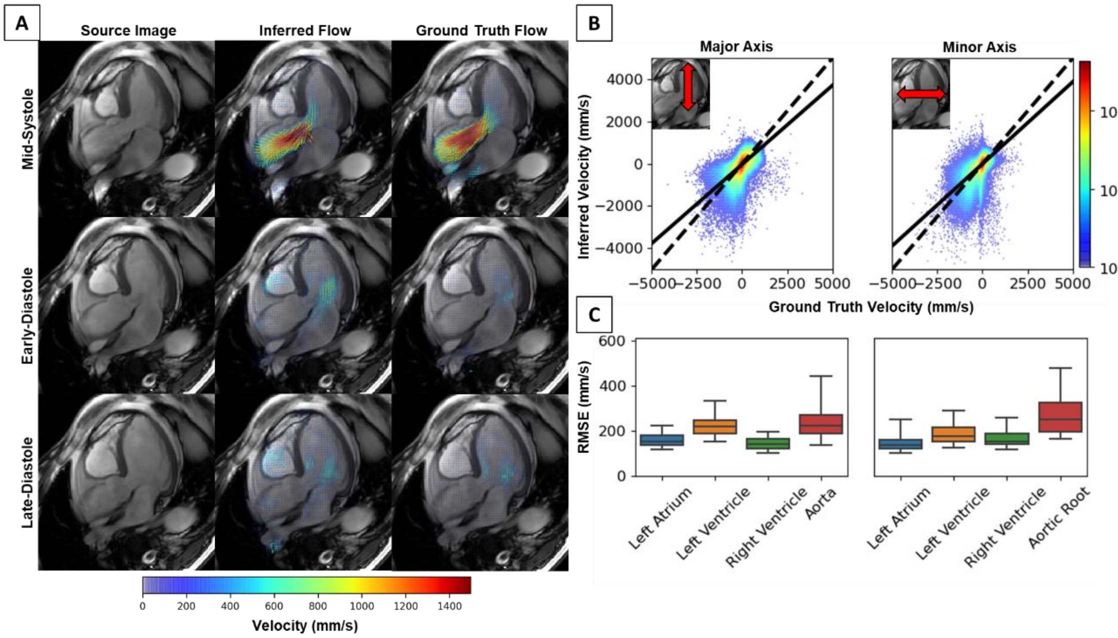

Figure 16: *Performance of the blood flow field synthesis prong of Triton-Net*. A) Representative example from a 69 year-old male with normal cardiac function depicting source 3-chamber cine SSFP images (left column), Triton-Net synthesized blood flow fields (center column), and ground truth flow fields derived from 4D Flow MRI(right column). B) Triton-Net synthesized flow compared with 4D Flow MRI-derived ground-truth along the major (left) and minor (right) axis in the left ventricle (n=1780 slices). The solid line indicates the least-squares regression line between synthesized and ground-truth flow, dashed line is line of identity. C) Root-mean-squared-error between Triton-Net synthesized blood flow velocities and 4D Flow MRI-derived ground truth along major (left) and minor (right) axes, for each cardiac chamber. Boxes encapsulate the interquartile range and whiskers demarcate the central 95% of data points

Root-mean-squared error (RMSE) for the synthesized velocities were within the range of measurement error of phase-contrast MRI (approximately 150-250 mm/s) for each chamber (Fig 16C). For the major axis, median RMSE (with 1st and 3rd quartiles in parentheses) were 154 (137 – 179) mm/s for the left atrium, 220 (188 – 247) mm/s for the left ventricle, 142 (121 – 166) mm/s for the right ventricle, and 223 (190 – 273) mm/s for the aortic root. For the minor axis, we found RMSE values of 136 (124 – 163) mm/s for the left atrium, 179 (154 – 216) mm/s for the left ventricle, 154 (140 – 190) mm/s for the right ventricle, and 252 (197 – 326) mm/s for the aortic root (Table 10).

.

Table 10: *Performance of Triton-Net Flow Synthesis.* RMSE results are medians, with first and third quartiles in parentheses. RMSE = Root Mean Squared Error

A: Triton-Net Flow Synthesis Linear Regression	Major Axis	Minor Axis
Slope	0.75	0.78
Intercept (mm/s)	-30.27	-3.79
Pearson Correlation Coefficient	0.57	0.57
P-value (Wald Test)	$P < 0.001$	$P < 0.001$
B: Triton-Net Flow Synthesis RMSE (mm/s)		
Left Atrium	154 (137 – 179)	136 (124 – 163)
Left Ventricle	220 (188 – 247)	179 (154 – 216)
Right Ventricle	142 (121 – 166)	154 (140 – 190)
Aortic Root	223 (190 – 273)	252 (197 – 326)

Images from a representative patient, a morphologically normal 69-year-old male, are shown in Figure 16A, spanning several timepoints over the cardiac cycle. During systole, we observe the ability of Triton-Net to infer a pattern of systolic flow in the left ventricular outflow tract similar to measured velocities from 4D Flow. During diastole, we observe the ability of Triton-Net to infer mitral inflow both during early ventricular relaxation (E-wave) and atrial contraction (A-wave), which were also comparable to ground truth 4D Flow MRI data.

We found that Triton-Net was generally able to correctly infer the presence of high velocity flow in the left ventricular outflow tract and aortic valve (Fig 17).

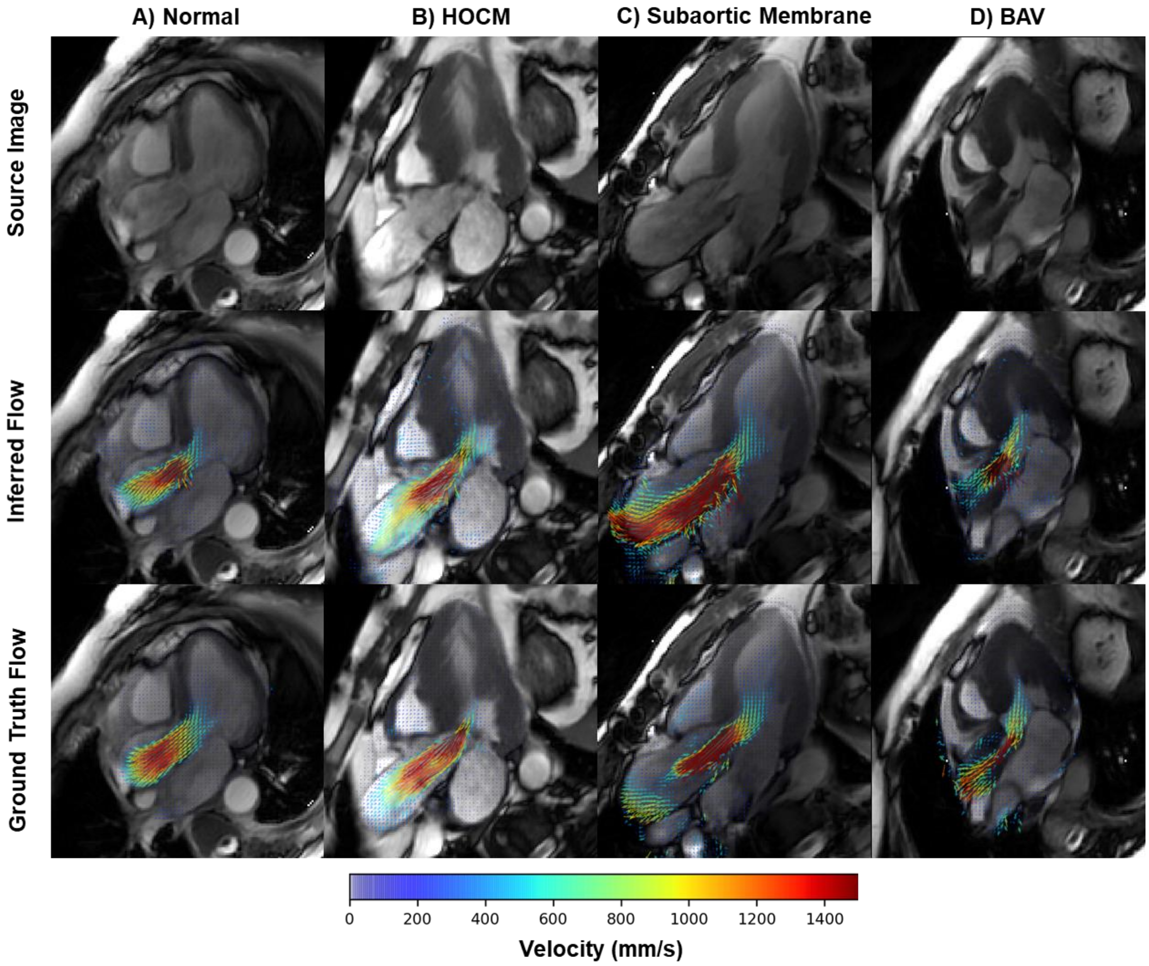

Figure 17: *Performance of Triton-Net flow synthesis on cine SSFP series with left ventricular outflow tract obstruction.* Representative mid-systolic examples depicting source long-axis cine SSFP images (top row), Triton-Net synthesized blood flow fields (center row), and ground truth flow fields derived from 4D Flow MRI (bottom row). Triton-Net synthesizes realistic intracardiac blood flow fields in: A) a structurally normal 51 year-old female, B) a 66 year-old male with hypertrophic obstructive cardiomyopathy, C) a 35 year-old male with subaortic membrane, and D) a 69 year-old female with bicuspid aortic valve.

In a morphologically normal patient, a 51-year-old female, Triton-Net inferred normal velocities within the left ventricular outflow tract, which were also normal by 4D Flow MRI (Supplemental Video 2). In contrast, in three representative patients with LVOT or AV obstruction on 4D Flow MRI, Triton-Net was able to infer high velocities at each location of outflow tract and valvular stenosis. In a 66-year-old male patient with hypertrophic obstructive cardiomyopathy and diffuse left ventricular hypertrophy (Fig 17B), Triton-Net inferred marked flow acceleration in the narrowed LVOT, comparable to 4D Flow MRI (Supplemental Video 3). Inferred peak velocity was 2.689 m/s, corresponding to a gradient of 29 mmHg. Measured peak velocity on 4D Flow was 4.093 m/s, corresponding to a gradient of 67 mmHg. In a 35-year-old male patient with subaortic membrane, Triton-Net inferred the presence of high velocity flow in the LVOT (Fig 17C). Inferred peak velocity was 4.433 m/s, corresponding to a gradient of 79 mmHg. Measured peak velocity on 4D Flow was 3.317 m/s, corresponding to a gradient of 44 mmHg. Lastly, in a 69-year-old female patient with bicuspid aortic valve, Triton-Net inferred the presence of flow acceleration at the stenotic aortic valve (Fig 17D). Inferred peak velocity was 3.620 m/s, corresponding to a gradient of 52 mmHg. Measured peak velocity on 4D Flow was 3.969 m/s, corresponding to a gradient of 63 mmHg.

4.5.4 Detection of Outflow Stenosis and Wall Thickening

To further assess the potential clinical utility of Triton-Net for outflow stenosis and myocardial wall thickening, we performed additional analyses in the test population for detection of both entities (Fig 18).

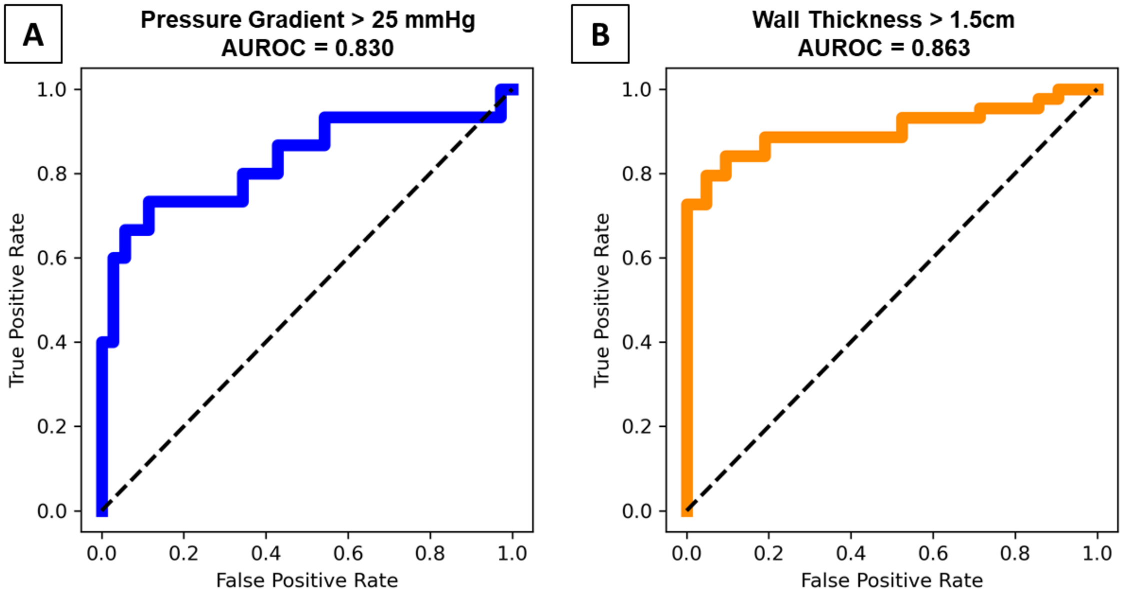

Figure 18: *Post-Processing of Triton-Net Inferences Yields Detection of Increased Left Ventricular Outflow Tract Pressure Gradients and Myocardial Thickness.* Receiver-Operating-Characteristic Curve for detection of A) left ventricular outflow obstruction (AUROC=0.830) and B) left ventricular hypertrophy (AUROC=0.863) in an independent test set (n=50 patients).

There was moderate agreement between outflow gradients inferred by Triton-Net and those measured by 4D Flow (p<0.001, r=0.54, slope=0.56). There was strong agreement between Triton-Net and manual measurements of myocardial thickness (p<0.001, r=0.77, slope=0.62). Receiver operating characteristic curves for detection of outflow obstruction showed strong ability to detect outflow tract obstruction exceeding 25 mmHg (AUROC 0.830). Similarly, receiver operating characteristic curves for left myocardial hypertrophy showed strong ability to detect myocardial wall thickening with end-diastolic wall thickness > 15 mm (AUROC 0.863).

4.6 Discussion

In this work, we illustrated the feasibility of a novel CNN architecture to concurrently perform the disparate but complementary tasks of cardiac chamber segmentation, landmark localization, and synthesis of blood flow fields. To our knowledge, Triton-Net is the first CNN capable of synthesizing blood flow fields solely from routine cine SSFP imaging data. Furthermore, in contrast to previous methods which have attacked the segmentation[19,129] and localization[62,122] problems separately, we show that the trifurcated architecture of Triton-Net can perform these tasks within a single comprehensive end-to-end architecture and achieve comparable performance to previously reported methods for the individual tasks.

There was strong quantitative agreement between synthesized flow fields and 4D Flow-derived ground truth across the entire cardiac cycle, particularly in the left ventricle. While synthesis of the blood flow field has historically been the domain of computational fluid dynamics[130], these methods are computationally expensive and require explicit boundary conditions, which are often approximated, particularly at the valves[131]. We attribute the performance of the CNN to the multi-pronged architecture that we employed, which was able to incorporate knowledge from the cardiac chamber segmentations and landmark locations to learn the relevant biomechanical relationships between the myocardial wall and blood flow velocity field from a relatively small training set. Recent work suggest that much fewer datasets are required when manual annotations of component sub-tasks are provided during training[132].

Our study has several limitations. All MRI data were sourced from examinations performed from a scanner from a single vendor from our institution. It is unclear how well the CNN will perform on images obtained on MR images from other vendors or institutions. It is likely that a larger training set incorporating image data from other MRI manufacturers and field strengths will further benefit the performance of the CNN on images from other institutions. Another limitation is that we have focused primarily on two-dimensional time-series, primarily on the 3-chamber view, as an illustration of the feasibility of this approach. We anticipate that this work may be further expanded to other imaging planes and volumetric imaging, including cardiac CTA, to enable synthesis of more comprehensive velocity fields.

In conclusion, we show the potential of a novel CNN architecture to extrapolate beyond the straightforward visual tasks of localization and segmentation. Specifically, Triton-Net can learn to synthesize the outflow blood velocity field from routine cine SSFP cardiac MR images. CNNs that can infer such information may provide additional hemodynamic insights retrospectively for patients who undergo routine cardiac MR imaging. We anticipate that similar strategies will be valuable to enable convolutional neural networks to perform complex tasks that require extrapolation of pathophysiology beyond what is anatomically visible. Such techniques may enable more in-depth biomechanical and hemodynamic analyses of historical cardiac MRI exams.

4.7 Acknowledgements

We acknowledge Microsoft Azure for their computational resources used to train our algorithms. We thank Hana G. Hadiprodjo for her assistance with manual segmentation and Dr. Stephen M. Masutani for their comments on this manuscript. Evan M. Masutani would like to acknowledge training grant funding from RSNA Medical Student Research Grant RMS2120, the American Heart Association Pre-Doctoral Fellowship 20PRE35180166, NIH T32GM007198, and NHLBI T32 HL105373. Tara A. Retson would like to acknowledge training support from NIH T32 EB005970, RSNA RR1879, and the UC San Diego Friedman Family Endowed Radiology Fellowship. Brian Hurt would like to acknowledge training support from NIH T32 EB005970 and RSNA RR2031. Kevin Blansit would like to acknowledge training support from the National Library of Medicine (T15LM011271).

This chapter was adapted, in part, from "Feasibility of Deep Learning to Synthesize Outflow Hemodynamics from Cardiac MRI" in preparation for submission to Radiology: Artificial Intelligence. The author list is: Masutani, Evan; Retson, Tara; Hurt, Brian; Blansit, Kevin; Hsiao, Albert. The dissertation author was the primary investigator and author of this paper.

4.8 Appendix

4.8.1 Triton-Net

Triton-Net is a novel, three-pronged architecture designed by the lead-author for multi-prong training and inference. Triton-Net segments cardiac chambers, localizes anatomical landmarks, and synthesize blood flow fields.

Triton-Net is composed of multiple output prongs for each component task and a deep decoder-encoder block that forms the shaft of the CNN. The encoder-decoder block is based on the 3D U-Net[61] architecture, and receives a temporal window (5 adjacent time frames) of long-axis cine SSFP images. Specifically, the encoder-decoder block sequentially comprised a 3D U-Net, a 3D-to-2D convolutional block, and a resolution scaling layer. The 3D-to-2D convolutional block comprised a 3-dimensional convolutional block with kernel size 5x1x1 and appropriate padding, resulting in coalescence of the temporal dimension, followed by a lambda squeeze layer. The resolution scaling layer scales the outputs of the 3D-to-2D convolutional block, incorporating pixel resolution and heart rate. From these scaled feature maps, triple output prongs produce single-frame cardiac chamber segmentations, landmark localization heatmaps, and flow fields. Each output prong comprised a sequential squeeze-excitation[133] and SRNet[128] blocks. We iterate Triton-Net over adjacent temporal windows to generate inferences over the entire cardiac cycle. To generate point-localizations, we solve for the argmax of each heatmap[62].

4.8.2 Data Preprocessing

We developed a semi-automated strategy for generating our training data. Our workflow comprised four steps: a) re-slicing source 4D Flow data to in-plane flow vectors based on each 3-chamber view's coordinates using trilinear interpolation, b) view-standardizing each paired 3-chamber-flow dataset[62] orienting the apex upward while reducing and centering the field of view to the heart, c) manually co-registering and annotating the cardiac chambers/landmarks between 3-chamber and flow datasets using in-house software to provide CNN segmentation ground truth[132], and d) organizing and scaling each dataset. We scaled 3-chamber pixel values to lie within [0,1] and flow values to lie within [-1,1] to serve as CNN blood flow synthesis ground truth.

4.8.3 Neural Network Training

We trained Triton-Net for 200 epochs using the Adam optimizer with a learning rate of 3e-5. We trained Triton-Net using a Microsoft Azure virtual machine running Ubuntu 18.04 (Canonical, London, England) equipped with four Quadro GV100 graphics cards with 16 GB of VRAM (Nvidia, Santa Clara, California). We used TensorFlow-GPU 2.1.0 (Google, Mountain View, California) with mixed-precision for all deep-learning experiments.

4.8.4 Loss Functions

For the following mathematical expressions, we denote each prong's output inference as $\hat{y}$ and its corresponding ground truth as y.

4.8.5 Segmentation Loss

For cardiac chamber segmentation, we employed a multichannel Dice loss function with a smoothing factor of 1[81]:

$$Segmentation\ Loss = 1 - \frac{1}{N_{segmentations}} \sum_{i}^{N_{segmentations}} Dice(y_i, \hat{y}_i)$$

4.8.6 Localization Loss

For landmark localization, we employed a heatmap localization strategy[62], where we Gaussian blurred the annotations for the mitral valve (s = 20 pixels), aortic valve (s = 20 pixels) and the apex (s = 40 pixels) to serve as multichannel ground-truth. This strategy permits use of weighted mean-squared-error (MSE) loss. We additionally solved for regions of high speed, y_{speed} (values greater than 0.05 in ijk coordinates). Together, the combine loss function took the form of:

$$Localization\ Loss = \left(\frac{1}{N_{localizations}} \sum_{i}^{N_{localizations}} MSE(y_i, \hat{y}_i) \right) + \lambda * MSE\left(y_{speed}, \hat{y}_{speed}\right)$$

$$\lambda = 1000$$

4.8.7 Flow Synthesis Loss

For blood flow field synthesis, we built a custom loss function incorporating the multi-scale structural similarity index (MSSSIM)[87] and piecewise linear regression for each component of velocity and the speed. We first define our piecewise linear regression function:

Given 1D vectors of inferred, $\hat{x}$, and ground truth, x, values, solution of the normal equation yields coefficients defining the best-fit linear regression[134]: For example:

We first generate a matrix $A = \begin{bmatrix} 1 & x_1 \\ \vdots & \vdots \\ 1 & x_N \end{bmatrix}$ and a column vector $\hat{x} = \begin{bmatrix} \hat{x}_1 \\ \vdots \\ \hat{x}_N \end{bmatrix}$

Solving $(A^T A)^{-1} A^T \hat{x}$ yields the coefficient matrix, $\hat{\theta} = \begin{bmatrix} \widehat{m}_0 \\ \widehat{m}_1 \end{bmatrix}$, such that $\widehat{m}_1 x + \widehat{m}_0$ defines the least-squares best-fit line. Given objective coefficients, $\theta = \begin{bmatrix} m_0 \\ m_1 \end{bmatrix}$, the loss function takes the form of $\sum\left(\theta - \hat{\theta}\right)^2$. Under ideal conditions, values of $\widehat{m}_0 = 0$ and $\widehat{m}_1 = 1$ mean $\hat{x} = x$. However, experimentally, objective values of $m_0 = 0, m_1 = 1$ do not necessary yield $\widehat{m}_0 = 0$ and $\widehat{m}_1 = 1$ and are dependent on training set composition and competing contributions from other component loss functions.

In the case of severe class imbalance e.g., preponderance of low-velocity pixels of low clinical significance, piecewise-linear regression permits greater weighing of high-magnitude pixels. For piecewise-linear regression, we wish to regress such that:

$\hat{x} = \begin{cases} m_1 x, & |x| \geq \alpha \\ m_2 x, & |x| < \alpha \end{cases}$; since this form is non-differentiable, we approximate it using a logistic function such that:

$\hat{x} = m_1 x + \frac{(m_2 - m_1)(x-\alpha)}{1+e^{-\sigma(x-\alpha)}} + \frac{(m_2 - m_1)(x+\alpha)(2+e^{-\sigma(x+\alpha)})}{1+e^{-\sigma(x+\alpha)}}$, which we denote as

$$\hat{x} = m_1 x + (m_2 - m_1) * f_1(x) + (m_2 - m_1) * f_2(x)$$

To solve the normal equation, we expand A column-wise:

$$A = \begin{bmatrix} 1 & x_1 & f_1(x_1) & f_2(x_1) \\ \vdots & \vdots & \vdots & \vdots \\ 1 & x_N & f_1(x_N) & f_2(x_N) \end{bmatrix}$$

Solving $(A^T A)^{-1} A^T \hat{x}$ yields the coefficient matrix, $\hat{\theta} = \begin{bmatrix} \widehat{m}_0 \\ \widehat{m}_1 \\ \widehat{m}_2 \\ \widehat{m}_3 \end{bmatrix}$, such that $\widehat{m}_3 f_2(x) + \widehat{m}_2 f_1(x) + \widehat{m}_1 x + \widehat{m}_0$ defines the piecewise least-squares best-fit line. As before, we can thus set our loss function to be of the form $\sum\left(\theta - \hat{\theta}\right)^2$, where $\theta = \begin{bmatrix} m_0 \\ m_1 \\ m_2 \\ m_3 \end{bmatrix}$ contains our objective coefficients. Note that each component of velocity requires its own linear regression. For our experiments, we used the following hyperparameters:

For objective coefficients, $m_0 = 0,\ m_1 = m_2 = m_3 = 1.25$

For logistic function, $\sigma = 10, \alpha = 0.3$

Thus, our flow loss function took the general form of:

$$Flow\ Loss = \sum_i^c (1 - MSSSIM(y_i, \hat{y}_i)) + \sum \left(\theta_i - \hat{\theta}_i\right)^2$$

Where c comprises the row and column components of velocity and the speed. We average the squared differences for the velocity components, and do not consider the negative term of the piecewise function for speed.

4.8.8 Peak Left Ventricular Speed Loss

Lastly, we composed an auxiliary loss function to optimize peak left ventricular speed in each frame (rather than over all pixels) to aid regression of LVOT peak pressure gradients. In a given batch, we multiplied each frame’s inferred speed by the commensurate left ventricular ground truth masks and applied global 2D maxpooling to solve for the peak left ventricular speeds. We use weighted linear regression, such that, given vectors of inferred, $\hat{x}$, and ground truth, x, values (with length equal to batch-size): $A = \begin{bmatrix} 1 & w_1 x_1 \\ \vdots & \vdots \\ 1 & w_N x_N \end{bmatrix}$, where w_i is the ground truth peak left ventricular speed at given frame, giving greater weight to high-speed values. We declare our objective coefficients $\theta = \begin{bmatrix} m_0 \\ m_1 \end{bmatrix}$, with $m_0 = 0, m_1 = 2$

Thus, our loss function is:

$$Peak\ Speed\ Loss = \sum \left(\theta - \hat{\theta}\right)^2 + MSE(y_i, \hat{y}_i)$$

4.8.9 Loss Function Weighing

For training, we gave scaled each component loss function such that their values were of similar scale. We weighed segmentation loss, localization loss, flow synthesis loss, and peak speed loss by factors of 10, 10, 0.1, and 0.1, respectively. Our final loss function is, therefore:

$$Loss = 10(Segmentation\ Loss + Localization\ Loss) + 0.1(Flow\ Loss + Peak\ Speed\ Loss)$$

4.9 Supplemental Figures and Videos

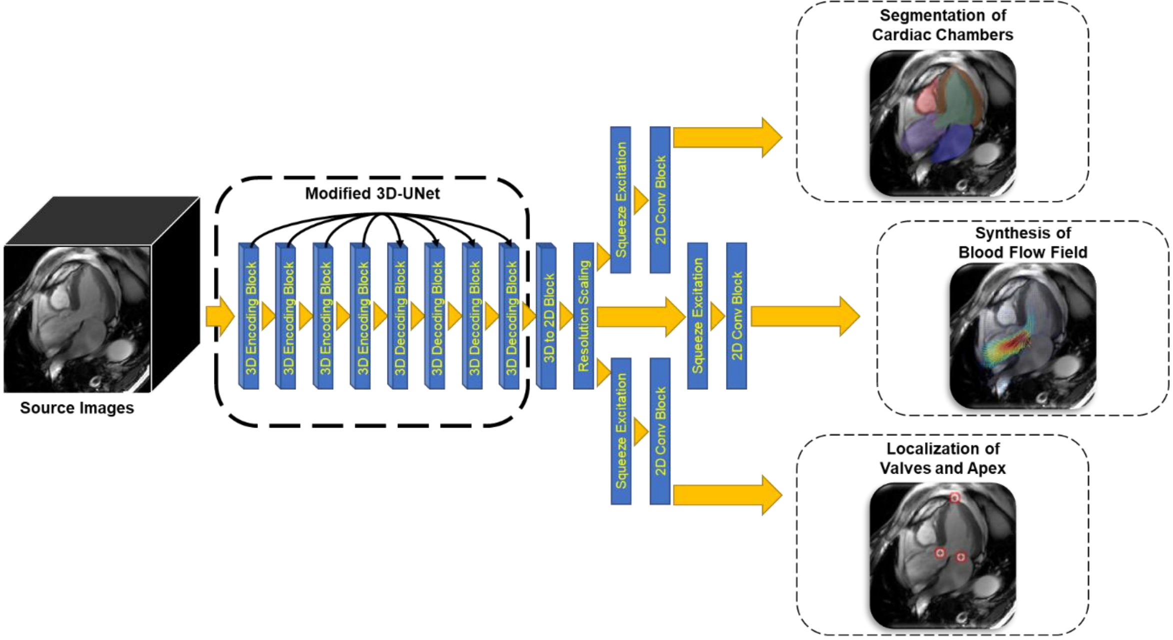

Supplemental Figure 3: *Details of Triton-Net Architecture*. Triton-Net is a deep multi-prong convolutional neural network which broadly comprises three parts. 1) A modified 3D-UNet architecture generates spatiotemporal feature maps from anatomic cine SSFP images. 2) These feature maps are condensed to a single timepoint and are scaled by the input cine SSFP series' spatiotemporal resolution. 3) The scaled feature maps trifurcate into three shallow, sub-convolutional neural network output prongs based on the SRNet architecture to generate inferences for multi-chamber segmentation, synthesis of blood flow field, and multi-landmark localization.

Supplemental Video 1: *Multi-chamber Segmentation Over the Cardiac Cycle.* Exemplar multi-chamber cardiac segmentation from a morphologically normal 41-year old female. Source 3-chamber cine SSFP images (left column), Triton-Net inferences (center column), and ground truth (right column), display segmentations over the entire cardiac cycle. (Bottom) The corresponding area of each color-matched inferred (-) and ground truth (x) segmentation is shown the cardiac cycle.

Supplemental Video 2: *Intracardiac Blood Flow Field Synthesis in a Morphologically-Normal Patient.* Exemplar blood flow fields from a 69 year-old male with normal cardiac function depicting source 3-chamber cine SSFP images (left column), Triton-Net synthesized blood flow fields (center column), and ground truth flow fields derived from 4D Flow MRI (right column). Systolic outflow, diastolic E-wave, and diastolic A-wave can all be visualized in inferred and ground truth flow fields.

Supplemental Video 3: *Intracardiac Blood Flow Field Synthesis in a Patient with Hypertrophic Obstructive Cardiomyopathy.* Exemplar blood flow fields from a 66 year-old male with hypertrophic obstructive cardiomyopathy depicting source 3-chamber cine SSFP images (left column), Triton-Net synthesized blood flow fields (center column), and ground truth flow fields derived from 4D Flow MRI (right column). Accelerated systolic outflow is seen in the obstructed left ventricular outflow tract in both inferred and ground truth flow fields.

Chapter 5: Deep Learning Synthetic Strain: Quantitative Assessment of Regional Wall Motion Abnormalities

5.1 Abstract

Background

Assessment of regional myocardial function in MRI is an essential component of diagnosing ischemic heart disease but is currently a qualitative visual task. Deep learning algorithms have potential to learn biomechanical tissue properties from image data, which might be used to detect disease.

Purpose

To assess the feasibility of a novel algorithm, which we call deep learning synthetic strain (DLSS), to infer myocardial velocity from cine SSFP images and detect wall motion abnormalities in patients with ischemic heart disease.

Methods

DLSS was developed using a retrospectively curated data set of 223 cardiac MRIs including cine SSFP images and 4D Flow velocity data. To establish normal ranges for DLSS, segmental peak radial strain was calculated from 40 subjects (age 41 ± 17 years, 10 female). Performance of DLSS was then evaluated on MRIs from a separate retrospective cohort of 53 patients with catheter angiography-proven coronary artery disease, which were independently evaluated for wall motion abnormalities by four cardiothoracic radiologists. The consensus of four readers was considered ground truth for evaluation of DLSS. Statistical analyses included Cohen's κ and area under the receiver operating characteristic (AUROC) curves.

Results

Median peak segmental radial strain in normal subjects was 38% (IQR: 30 – 48%). Amongst patients with ischemic heart disease (846 segments from 53 patients, age 61 ± 12 years, 12 female), Cohen's κ between four cardiothoracic readers ranged between 0.60 – 0.78. AUROC for DLSS detection of segmental wall motion abnormalities was 0.87. Using a fixed 30% threshold for abnormal peak radial strain, sensitivity, specificity, and accuracy for detection of segmental wall motion abnormalities were 84%, 83%, and 84%, respectively.

Conclusion

Deep learning can be used to infer myocardial velocity from routine cine SSFP images. DLSS discriminates normal from abnormal myocardial contraction in patients with ischemic heart disease with performance comparable to subspecialty radiologists.

5.2 Summary and Key Results

Summary

A deep learning algorithm can infer myocardial velocities and quantify strain from cine SSFP images to detect wall motion abnormalities in patients with ischemic heart disease with performance comparable to subspecialty radiologists.

Key Results

- Normal ranges for segmental myocardial strain and strain rate for the algorithm were established in 40 normal subjects.
- Subspecialty radiologists showed moderate-to-substantial agreement for detection of wall motion abnormalities in 53 patients with ischemic heart disease (Cohen's k: 0.60-0.78)

- Relative to the consensus of four subspecialty radiologists, the algorithm detected wall motion abnormalities in patients with ischemic heart disease with AUROC of 0.87, and accuracy, sensitivity, and specificity of 84%, 84%, and 83%, respectively.

5.3 Introduction

Cardiac MRI is the clinical reference standard for non-invasive evaluation of cardiac function due to its ability to completely visualize the heart without ionizing radiation and without dependence on sonographic windows[9,135,136]. Ventricular volumetry and ejection fraction remain the principal measurements clinically used to assess ventricular function, but do not provide information regarding regional function. Clinical assessment of regional myocardial function (4–6) largely remains a subjective visual task by expert readers[13,20,44–46], and provides important cues for diagnosis of multiple diseases[137–139] including ischemic heart disease.

Strain imaging techniques, first described in the 1980s[140], have potential to provide granular measurements of regional myocardial function. Multiple methods have been developed over the last several decades, including myocardial tagging[140], DENSE[141], SENC(14)(14), HARP[143] and phase-contrast velocity mapping[144,145]. Each of these however requires acquisition of a dedicated imaging sequence and considerable post-processing analysis. More recently, feature tracking strain methods have emerged as a method for retrospective analysis of strain from cine SSFP images[51,52], with multiple studies showing potential value of measurements of global strain. However, while echocardiographic studies have confirmed the relationship between regional speckle tracking strain and visual grades of myocardial function[146] or myocardial scar[147,148], feature tracking methods currently lack this evidence base. The lack of such data may be due to limited reliability of current feature tracking methods for assessing regional wall motion[148] with widely varying ranges in normal subjects[149] and poor agreement with established strain imaging techniques[150,151].

Deep learning methods, specifically convolutional neural networks (CNNs), have emerged as a powerful technology for the analysis of biomedical image data, and have the capability of rapidly performing computational tasks. Applications of this technology in cardiac MRI include image classification[152], localization[62,66], segmentation[10,153,154], and image enhancement[125,155]. Recent groups have proposed application of deep learning methods to simplify the analysis of dedicated strain imaging techniques[156,157]. However, a rate-limiting factor for such techniques remains the need for a separate acquisition of strain image data.

We thus sought to develop an alternative strategy, which we call Deep Learning Synthetic Strain (DLSS) to enable the measurement of myocardial wall motion from cine SSFP images that are routinely acquired in clinical cardiac MRI examinations. We apply this new approach to determine normal ranges for strain and strain rate to a population of normal subjects and use this to establish thresholds for abnormal myocardial contraction. Finally, we evaluated the ability of DLSS to identify regional wall motion abnormalities in patients with catheter-angiography proven coronary artery disease, assessing performance against a consensus of four cardiothoracic radiologist readers.

5.4 Materials and Methods

Our study was performed with institutional review board (IRB) approval including waiver of informed consent for development of the algorithm and assessment on retrospective patient populations. Written informed consent was additionally obtained from normal volunteers according to a separate IRB protocol for MRI scanning of volunteer subjects.

5.4.1 Algorithm Training Data

To establish data for deep learning algorithm development, we retrospectively collected a convenience sample of 223 cardiac MRI exams from 219 patients, which included short-axis cine SSFP and 4D Flow as part of routine clinical exams at our institution between November 2017 to May 2021. 4D Flow MRI images were corrected for phase error (Arterys Cardio AI; San Francisco, CA). 4D Flow velocities were then linearly resampled and co-registered with cine SSFP images by the lead author using custom in-house software developed in Python. Left ventricular myocardial segmentations were obtained using a previously developed, commercially available neural network (Cardio AI, Arterys; San Francisco, CA) and incorporated into algorithm training.

Data was divided into training and validation data sets by exam. 90% of exams (602 short-axis slices from 201 exams) were allocated to the training set and 10% of exams (65 slices from 22 exams) were allocated to the validation set for CNN optimization. Training data was augmented by in-plane rotation at 15-degree increments and variable adjustments of image contrast including intensity thresholding and normalization.

5.4.2 Neural Network Architecture

We designed a novel CNN architecture to infer spatiotemporal myocardial velocity fields from short axis cine SSFP images (Figure 19). The CNN takes images from the entire cardiac cycle and returns 1) the in-plane myocardial velocity field and 2) myocardial segmentations for each time frame, which are post-processed to yield strain rate and strain fields. These are further decomposed into radial and circumferential components. Additional details regarding CNN architecture and data post-processing can be found in the Supporting Information.

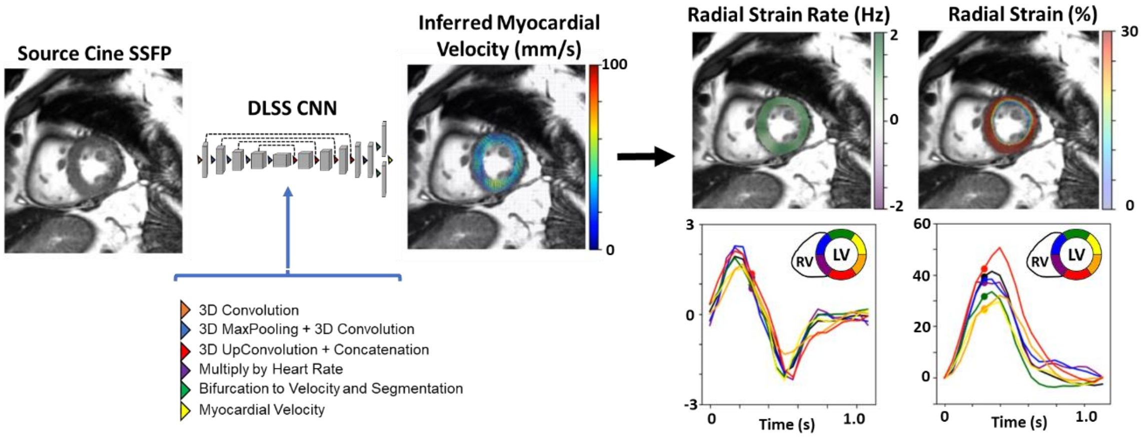

Figure 19: *Overview of the deep learning synthetic strain (DLSS) approach.* A CNN was trained to infer myocardial velocities from a series of cine SSFP images. Training data included co-registered myocardial velocities from cardiac MRIs from 219 patients who underwent 4D Flow as part of their clinical exam. The inferred myocardial velocities are then used to calculate myocardial strain rate and strain maps, which are superimposed on the source SSFP images for quantification and visual interpretation.

5.4.3 Establishment of Segmental and Global Normal Ranges

To establish segmental normal ranges for the DLSS technique, short-axis cine SSFP series were obtained from 21 healthy volunteers and a retrospective population of 19 patients with normal cardiac MRI (referred for iron deposition or arrhythmogenic right ventricular dysplasia/cardiomyopathy) from February 2015 and October 2021. Normal cardiac MRI was defined as normal ventricular volume, function, and absence of delayed enhancement. Images were processed with DLSS to yield segmental and global strain measurements.

5.4.4 Assessment of Wall Motion Abnormalities in Patients with Ischemic Heart Disease

To assess the ability of DLSS to identify segmental wall motion abnormalities in an independent population, short-axis cine SSFP images from 53 patients with catheter angiography-proven ischemic heart disease were retrospectively curated between September 2014 and December 2020. Strain was calculated using DLSS and partitioned into 16 AHA segments, excluding the apical segment, for a total of 846 segments.

To establish a reference standard for the presence of wall motion abnormalities, four board-certified cardiothoracic radiologists (blinded for peer review) graded each segment on a 1-4 scale as either 1-normal, 2-hypokinetic, 3-akinetic, or 4-dyskinetic. Post-fellowship experience of each radiologist was 14 years, 2 years, 2 years, and 3 years, respectively. Radiologists were solely provided short axis cine SSFP images and were blinded to all other clinical and demographic information. Because few dyskinetic segments were identified in this population, dyskinetic and akinetic segments were pooled for analysis. Segmental wall motion scores for all four radiologists were averaged to serve as consensus ground truth for assessment of DLSS.

5.4.5 Data Acquisition

MRI exams were performed with either a 1.5-T MRI scanner (Signa HDxt; GE Healthcare) or a 3.0-T MRI scanner (Discovery MR750 DV26; GE Healthcare). All exams employed a standard 32-channel phased-array coil. 4D Flow MRI was performed at 3.0-T following administration of intravenous gadolinium contrast (gadobenate dimeglumine, 0.15 mmol/kg) and employed respiratory self-navigation, compressed-sensing, and parallel imaging reconstruction[127]. Additional scanner parameters are listed in Supplemental Table 1.

5.4.6 Statistical Analysis

To assess inter-rater agreement between subspecialty cardiothoracic radiologists for grading of wall motion abnormalities, we calculated the Cohen's kappa (κ) coefficient and intra-class correlation coefficient (ICC)[158]. To evaluate DLSS algorithm performance for detecting wall motion abnormalities, we generated receiver-operating characteristic (ROC) curves and reported the area under the ROC curve (AUROC). Thresholds for discriminating normal from abnormal myocardial wall motion were defined based on the Youden index[159]. Thresholds for akinesis and dyskinesis were defined as 50% of this threshold. We also report accuracy, sensitivity, and specificity of the DLSS algorithm for detecting abnormal wall motion.

Statistical analysis was performed using Python (version 3.7, Python Software Foundation, Wilmington, Del), NumPy, SciPy, scikit-learn, pingouin, and Excel (Microsoft, Redmond, Wash). k values between 0.41 – 0.60 and between 0.61 – 0.80 denoted moderate and substantial agreement, respectively[160]. ICC values above 0.75 were considered excellent[161].

5.5 Results

5.5.1 Ranges of Segmental Strain in Normal Subjects

To establish normal ranges for segmental myocardial strain, we applied DLSS to analyze cine SSFP images from a cohort of 40 normal subjects comprised of two groups with no known cardiovascular disease: (a) 21 healthy volunteers and (b) 19 patients with normal cardiac MRI. Demographic parameters are summarized in Table 11.

Table 11: Patient Demographics. Age, BMI, BSA, and Heart Rate presented as sample means ± standard deviation

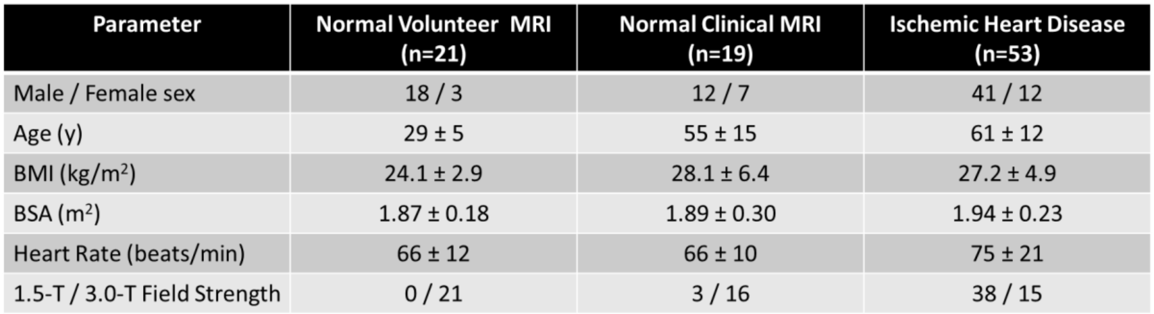

Parameter	Normal Volunteer MRI (n=21)	Normal Clinical MRI (n=19)	Ischemic Heart Disease (n=53)
Male / Female sex	18 / 3	12 / 7	41 / 12
Age (y)	29 ± 5	55 ± 15	61 ± 12
BMI (kg/m^2)	24.1 ± 2.9	28.1 ± 6.4	27.2 ± 4.9
BSA (m^2)	1.87 ± 0.18	1.89 ± 0.30	1.94 ± 0.23
Heart Rate (beats/min)	66 ± 12	66 ± 10	75 ± 21
1.5-T / 3.0-T Field Strength	0 / 21	3 / 16	38 / 15

DLSS peak radial and circumferential strain for each segment are listed in Table 12. Peak radial strain for each segment is shown in figure 20. Broadly, we note lower median peak radial strain in the anterior, anteroseptal, and inferoseptal segments. Peak radial strain was greater in apical segments. In contrast, we observed less variability in segmental peak circumferential strain across segments.

Table 12: *DLSS peak strain in volunteers and patients without known cardiac disease.* Data for all myocardial segments are presented as population median, values in parentheses are the interquartile range.

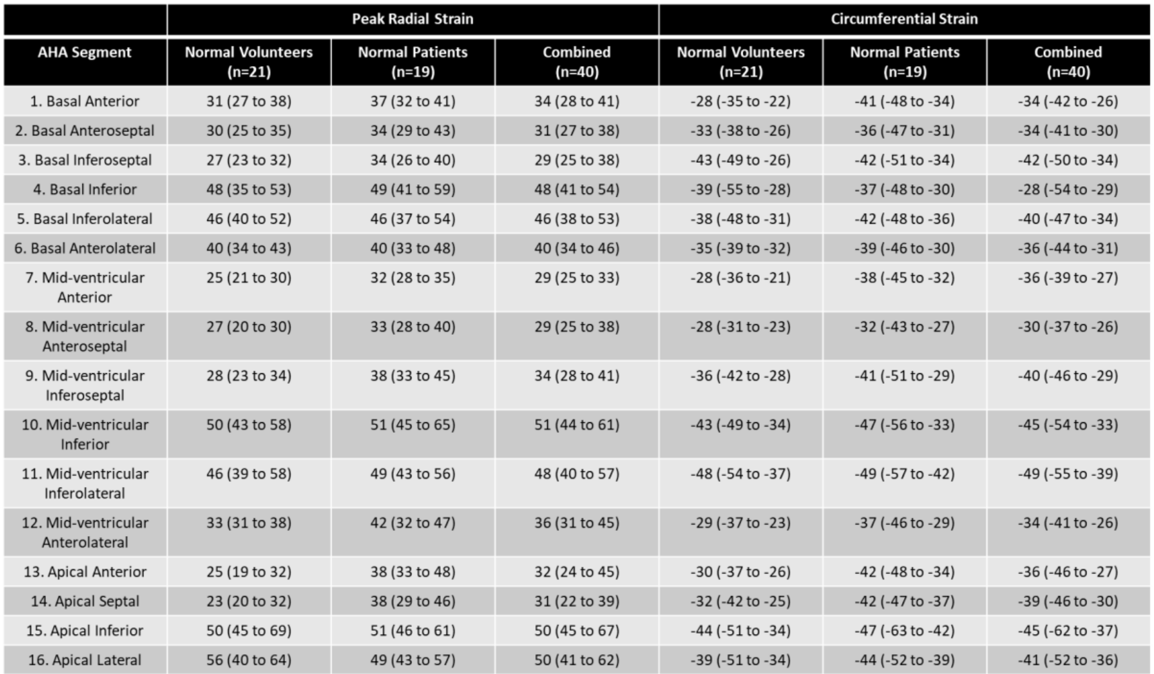

	Peak Radial Strain			Circumferential Strain		
AHA Segment	Normal Volunteers (n=21)	Normal Patients (n=19)	Combined (n=40)	Normal Volunteers (n=21)	Normal Patients (n=19)	Combined (n=40)
1. Basal Anterior	31 (27 to 38)	37 (32 to 41)	34 (28 to 41)	-28 (-35 to -22)	-41 (-48 to -34)	-34 (-42 to -26)
2. Basal Anteroseptal	30 (25 to 35)	34 (29 to 43)	31 (27 to 38)	-33 (-38 to -26)	-36 (-47 to -31)	-34 (-41 to -30)
3. Basal Inferoseptal	27 (23 to 32)	34 (26 to 40)	29 (25 to 38)	-43 (-49 to -26)	-42 (-51 to -34)	-42 (-50 to -34)
4. Basal Inferior	48 (35 to 53)	49 (41 to 59)	48 (41 to 54)	-39 (-55 to -28)	-37 (-48 to -30)	-28 (-54 to -29)
5. Basal Inferolateral	46 (40 to 52)	46 (37 to 54)	46 (38 to 53)	-38 (-48 to -31)	-42 (-48 to -36)	-40 (-47 to -34)
6. Basal Anterolateral	40 (34 to 43)	40 (33 to 48)	40 (34 to 46)	-35 (-39 to -32)	-39 (-46 to -30)	-36 (-44 to -31)
7. Mid-ventricular Anterior	25 (21 to 30)	32 (28 to 35)	29 (25 to 33)	-28 (-36 to -21)	-38 (-45 to -32)	-36 (-39 to -27)
8. Mid-ventricular Anteroseptal	27 (20 to 30)	33 (28 to 40)	29 (25 to 38)	-28 (-31 to -23)	-32 (-43 to -27)	-30 (-37 to -26)
9. Mid-ventricular Inferoseptal	28 (23 to 34)	38 (33 to 45)	34 (28 to 41)	-36 (-42 to -28)	-41 (-51 to -29)	-40 (-46 to -29)
10. Mid-ventricular Inferior	50 (43 to 58)	51 (45 to 65)	51 (44 to 61)	-43 (-49 to -34)	-47 (-56 to -33)	-45 (-54 to -33)
11. Mid-ventricular Inferolateral	46 (39 to 58)	49 (43 to 56)	48 (40 to 57)	-48 (-54 to -37)	-49 (-57 to -42)	-49 (-55 to -39)
12. Mid-ventricular Anterolateral	33 (31 to 38)	42 (32 to 47)	36 (31 to 45)	-29 (-37 to -23)	-37 (-46 to -29)	-34 (-41 to -26)
13. Apical Anterior	25 (19 to 32)	38 (33 to 48)	32 (24 to 45)	-30 (-37 to -26)	-42 (-48 to -34)	-36 (-46 to -27)
14. Apical Septal	23 (20 to 32)	38 (29 to 46)	31 (22 to 39)	-32 (-42 to -25)	-42 (-47 to -37)	-39 (-46 to -30)
15. Apical Inferior	50 (45 to 69)	51 (46 to 61)	50 (45 to 67)	-44 (-51 to -34)	-47 (-63 to -42)	-45 (-62 to -37)
16. Apical Lateral	56 (40 to 64)	49 (43 to 57)	50 (41 to 62)	-39 (-51 to -34)	-44 (-52 to -39)	-41 (-52 to -36)

In the 21 healthy volunteers, the median peak radial strain averaged over all 16 AHA segments, was 35% (IQR: 27 – 45%). Median peak GRS was 38% (IQR: 34 – 40%). We observed similar values in an independent cohort of 19 patients with normal cardiac MRI. The median peak radial strain was 41% (IQR: 33 – 49%) and the median GRS was 40% (IQR: 38 – 47%). Pooled median peak radial strain was 38% (IQR: 30 – 48%) and median GRS 39% (36 – 44%).

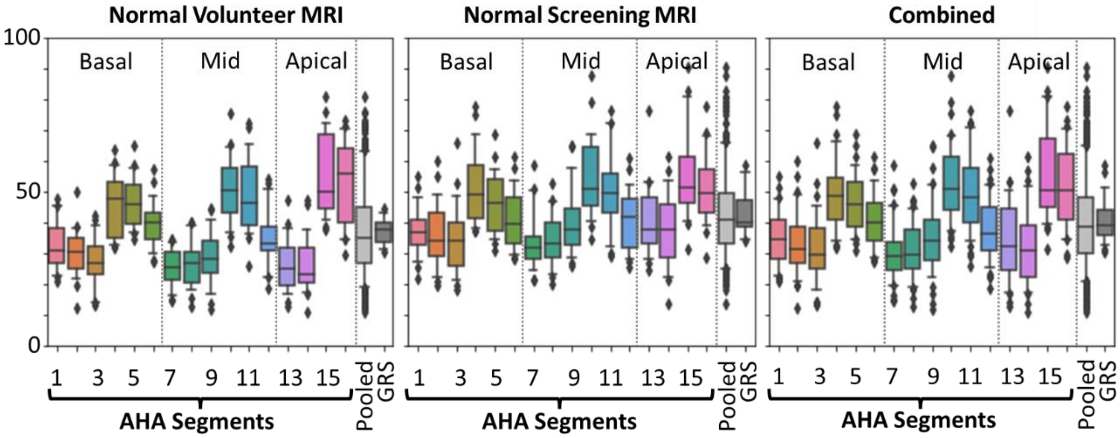

Figure 20: *Distribution of Peak Radial Strain in Normal Volunteers and Clinically-Normal Patients.* DLSS estimates of radial strain were computed in 21 normal volunteers and 19 patients with normal cardiac MRIs, who were referred for screening for iron deposition, family history of ARVD/C, or hemoglobinopathy. Both populations show similar distributions of DLSS-estimated peak radial strain and provide a reference point for identification of reduced regional wall motion.

We observed similar trends for peak circumferential strain. For the 21 healthy volunteers, median peak circumferential strain averaged over all 16 AHA segments was -35% (IQR: -44 to -27%) and median peak GCS was -36% (IQR: -40 to -32%). Likewise, for the 19 patients with normal cardiac MRI, median peak circumferential strain was -41% (IQR: -49 to -33%) and median peak GCS was -40% (IQR: -47 to -38%). Pooled median peak circumferential strain was -38% (IQR: -47 to -30%) and median GCS -38% (-43 to -35%).

5.5.2 Reader Agreement for Ischemic Wall Motion Abnormalities

Table 13 shows the interobserver agreement as assessed by Cohen's κ between the four cardiothoracic radiologists. For classification of normal vs abnormal segments, Cohen's κ ranged from 0.60 – 0.78, indicating moderate-to-substantial interobserver agreement. ICC(2,k) was 0.96 (95% CI: 0.93, 0.98). For classification of normal vs hypokinetic vs akinetic/dyskinetic segments, Cohen's κ ranged from 0.52 – 0.64, indicating moderate-to-substantial interobserver agreement. ICC(2,k) was 0.97 (95% CI: 0.95 – 0.98).

Table 13: *Inter-rater Cohen's kappa for identification of segmental wall motion abnormalities*

A

Normal vs. Abnormal Segments Cohen's κ				
	Reader 1	Reader 2	Reader 3	Reader 4
Reader 1		0.75	72	0.60
Reader 2			0.78	0.62
Reader 3				0.60

B

Normal vs. Hypokinetic vs. Akinetic/Dyskinetic Segments Cohen's κ				
	Reader 1	Reader 2	Reader 3	Reader 4
Reader 1		0.64	0.61	0.52
Reader 2			0.62	0.54
Reader 3				0.52

5.5.3 Deep Learning Detection of Wall Motion Abnormalities

In the schematic diagram of the implementation of the deep learning synthetic strain algorithm (Figure 19), we show an exemplar case of a 58-year-old male patient with a normal cardiac MRI, who initially presented with fatigue and dyspnea on exertion. The patient was subsequently found to have no obstructive coronary artery disease on coronary artery catheterization. DLSS radial strain rate curves were relatively uniform across all myocardial segments with peak segmental strain rate ranging from 1.47 – 2.27 Hz. Similarly, DLSS radial strain curves were also relatively uniform across all myocardial segments with peak segmental values ranging from 29 – 47%.

In contrast, a 66-year-old male with a history of coronary artery disease and ST-segment elevated myocardial infarction presented with intermittent chest pressure and underwent cardiac MRI 3 days after acute presentation (Figure 21).

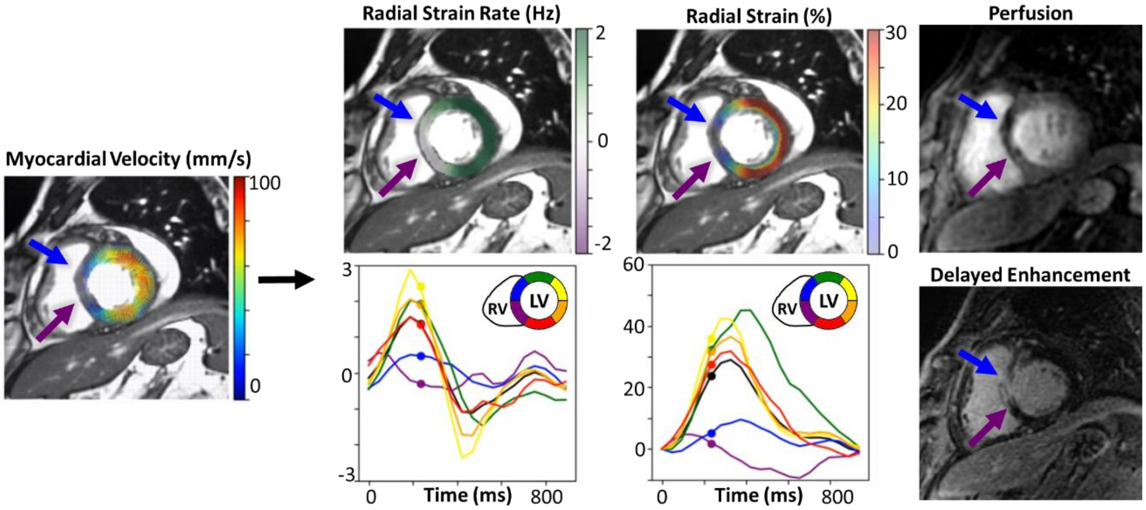

Figure 21: *Exemplar case of a patient with catheter angiogram-proven LAD occlusion.* There is focal wall motion abnormality of the anteroseptal (blue arrow) and inferoseptal (purple arrow) walls with decreased peak radial strain and strain rate. Corresponding strain and strain rate curves show the severity of this abnormality relative to the other myocardial segments in the same slice. Following intravenous contrast administration, the septal wall shows a matching perfusion defect and transmural delayed enhancement, indicating myocardial ischemia and infarction.

Cardiac MRI acquired at 1.5 T showed reduced global function (LVEF 25%). DLSS showed markedly reduced strain rate and strain in the basal anteroseptal and inferoseptal segments in addition to multiple mid-ventricular and apical segments (not shown) corresponding to the left anterior descending (LAD) territory. Peak radial strain of the anteroseptal and inferoseptal segments were 8.4% and -2.2%, respectively, far below the normal range. Peak radial strain of the remaining segments ranged from 32 – 42%, within the normal range. Following administration of intravenous contrast, there is a perfusion defect and transmural delayed enhancement in the septal wall. Catheter angiography confirmed a complete occlusion of the mid LAD.

ROC curves for DLSS detection of segmental wall motion abnormalities are shown in Figure 22. Using fixed thresholds of peak radial strain to identify wall motion abnormalities yielded AUROC = 0.87 (Figure 22A).

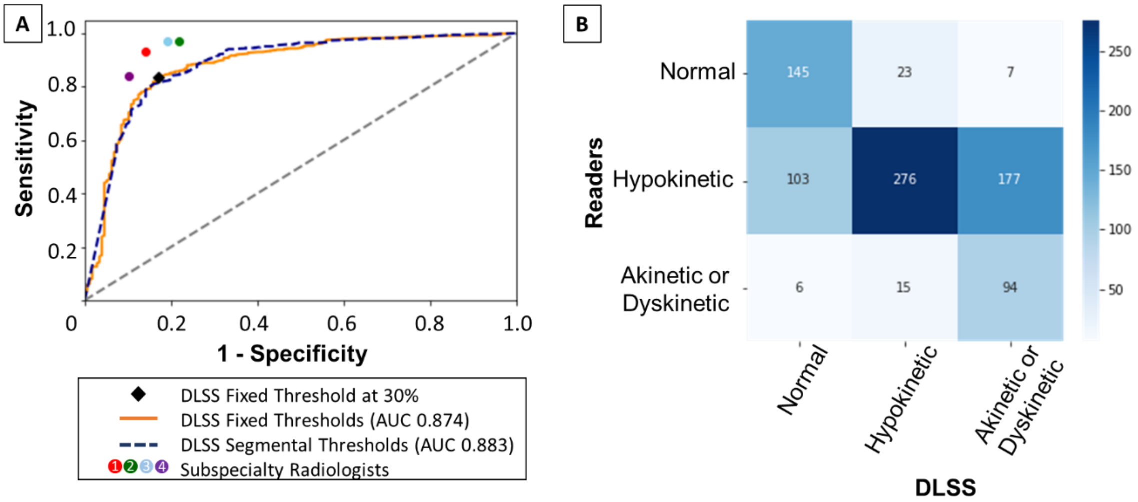

Figure 22: *Performance of DLSS for detecting segmental wall motion abnormalities.* ROC curves for discrimination of normal from abnormal (hypokinetic, akinetic, dyskinetic), relative to the consensus of four subspecialty readers is shown in A. Orange line shows classification performance of DLSS when using fixed peak radial strain values as cutoffs (AUROC = 0.87). Black diamond marks the location of the fixed peak radial strain threshold of 30% on the ROC curve. Dashed blue line shows classification performance of DLSS when using peak radial strain percentiles as cutoffs (AUROC = 0.88). Performance of each reader relative to the average of the other readers are shown in the colored dots. Confusion matrix for the performance of DLSS for discriminating wall motion abnormalities, relative to the average of four readers is shown in B.

Similarly, using segment-specific percentile thresholds of peak strain yielded AUROC = 0.88. At the Youden index, which corresponded to peak radial strain of 30%, DLSS had 84% sensitivity, 83% specificity, and 84% accuracy (Table 14). In comparison, expert reader performance relative to the consensus of the remaining three readers ranged from 84 – 97% for sensitivity, 78 – 90% for specificity, and 85 – 93% for accuracy.

Table 14: *DLSS performance using fixed peak strain cutoffs.* 30% peak radial strain corresponds to 25th percentile of normal population peak radial strain measurements. -30% peak circumferential strain corresponds to 75th percentile of normal population peak circumferential strain measurements.

Task	Metric	Cutoff	Sensitivity	Specificity	Accuracy
Normal vs. Abnormal Segments	Fixed Peak Radial Strain	30%	84%	83%	84%
Hypokinetic vs Akinetic & Dyskinetic Segments	Fixed Peak Radial Strain	15%	86%	61%	66%
Normal vs. Abnormal Segments	Fixed Peak Circumferential Strain	-30%	80%	73%	78%
Hypokinetic vs Akinetic & Dyskinetic Segments	Fixed Peak Circumferential Strain	-15%	65%	67%	67%

A confusion matrix is shown in Figure 22B. For discrimination of hypokinetic vs akinetic/dyskinetic segments using a peak radial strain threshold of 15%, DLSS had 86% sensitivity, 61% specificity, and 66% accuracy. Peak circumferential strain was generally less reliable for detection of wall motion abnormalities relative to peak radial strain. For identification of any wall motion abnormalities, DLSS-derived peak circumferential strain had 80% sensitivity, 73% specificity, and 78% accuracy. For discrimination of hypokinetic vs akinetic/dyskinetic segments, fixed peak circumferential strain cutoffs yielded 65% sensitivity, 67% specificity, and 67% accuracy.

5.5.4 Potential Applications of DLSS Beyond Ischemic Heart Disease

To further assess the potential of DLSS for detecting abnormal wall motion beyond the cohort of patients with ischemic heart disease, we executed the algorithm on two additional patients.

A 55-year-old male who presented with cardiac arrest was diagnosed with viral myocarditis 4 months prior to cardiac MRI. The patient was referred to MRI to assess scar for potential implantable cardioverter defibrillator placement, and initially assessed to have normal cardiac MRI with no delayed enhancement or edema. However, DLSS detected global hypokinesis with marked hypokinesis at the mid anteroseptal and anterior segments with peak radial strain 15% and 19%, respectively (Figure 23).

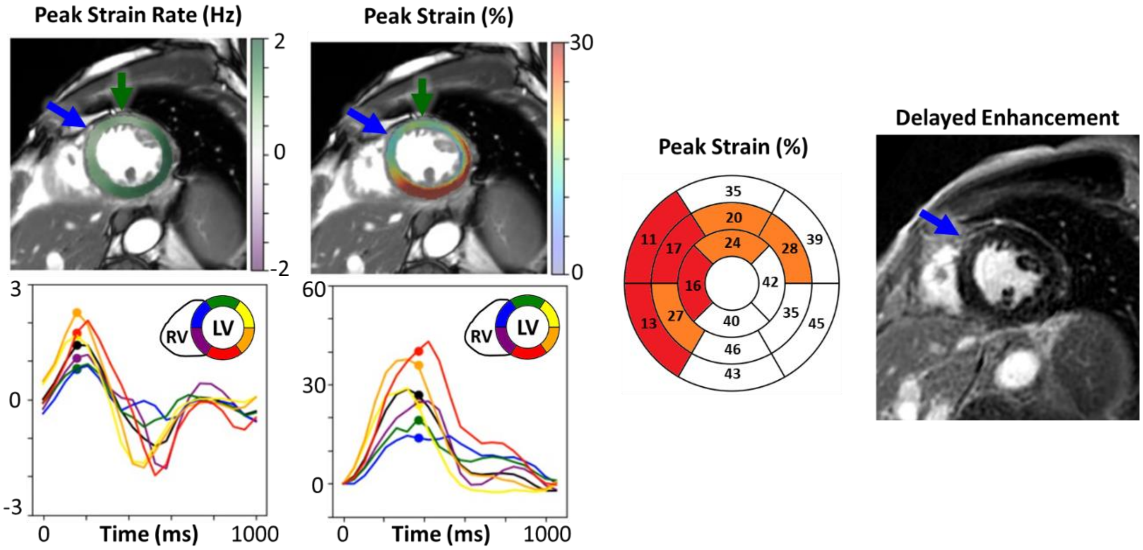

Figure 23: *Patient with cardiac arrest 4 months prior with viral prodrome and presumed myocarditis with negative myocardial biopsy.* There is hypokinesis of the mid anteroseptal (blue arrow) and anterior (green arrow) wall evident on DLSS-derived peak radial strain rate and strain maps. Following administration of intravenous contrast, there is only subtle mesocardial enhancement of the mid anteroseptal wall. Without DLSS strain maps, this was initially interpreted clinically as a normal cardiac MRI. Peak segmental radial strain shown in bullseye plot.

Subsequent review of the delayed enhancement images showed subtle mesocardial delayed enhancement at the mid anteroseptal wall. When requested to perform a second review of short-axis cine SSFP images from this patient without clinical history, readers 1, 2, and 3 interpreted the mid ventricular slices as globally hypokinetic without perceiving additional focal wall motion abnormality. Reader 4 noted additional focal hypokinesis of the mid anterior wall, corresponding with reduced strain detected by DLSS.

A 54-year-old male who presented with cardiac arrest was referred for cardiac MRI to evaluate for myocardial scar and viability. The cardiac MRI was initially interpreted with no wall motion abnormalities or delayed enhancement. Catheter angiography was also unremarkable. However, DLSS detected marked dissociation between contraction of the septal and lateral walls (Figure 24).

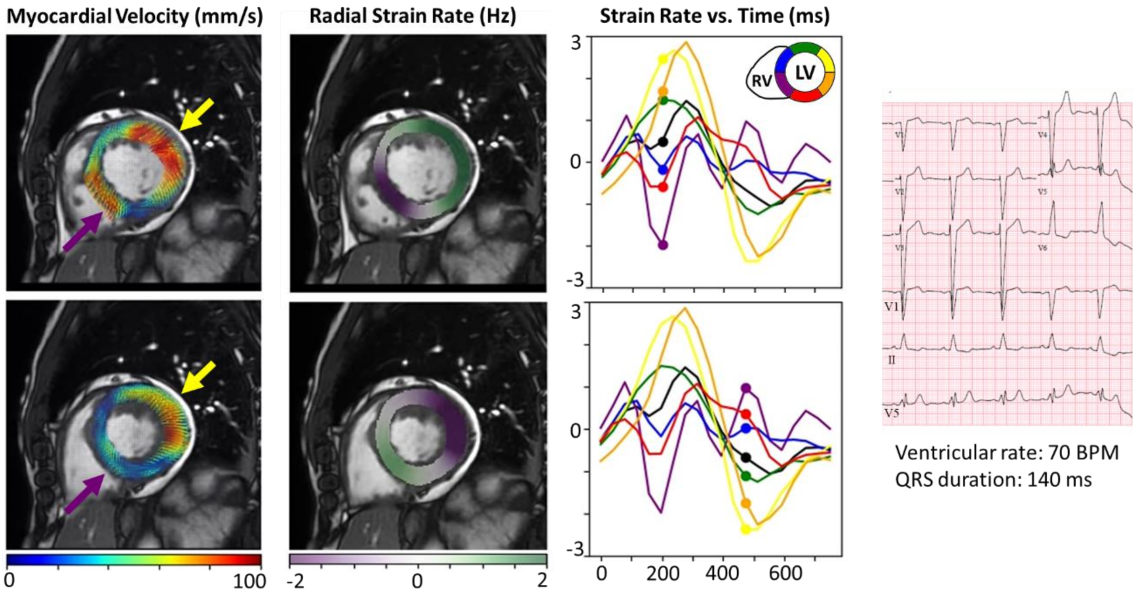

Figure 24: *Ventricular dyssynchrony with dissociation of contraction of the septal and lateral walls due to left bundle branch block, visualized and quantified with DLSS*. In the top row early in the cardiac cycle, while the anterolateral wall (yellow arrow) contracts, the inferoseptal wall (purple arrow) relaxes. In the bottom row, the inferoseptal wall then contracts while the anterolateral wall relaxes. Strain rate curves highlight the dissociation between these segments. EKG from this patients showed a left bundle branch block.

While the lateral wall contracted, the septal wall showed dyssynchronous relaxation with negative radial strain rate; while the lateral wall relaxed, the septal wall showed dyssynchronous contraction with positive radial strain rate. ECG confirmed the presence of a complete left bundle branch block (LBBB), which explains the pattern of dyssynchronous myocardial wall motion.

5.6 Discussion

In this study, we show the potential of a deep learning algorithm to quantify strain and strain rate from routine short-axis cine SSFP MRI acquired at both 1.5 T and 3.0 T. To establish normal ranges for segmental radial and circumferential strain, we analyzed segmental strain in 16 AHA segments in 40 subjects without known cardiac disease. We then showed the potential of the deep learning algorithm to detect wall motion abnormalities in 53 patients with catheter angiography-proven ischemic heart disease, based on thresholds of segmental myocardial strain. We observed high agreement (Cohen's κ 0.60–0.78) between four expert subspecialty radiologists for visual assessment of segmental wall motion abnormalities, who formed a consensus ground truth for evaluation of the deep learning algorithm. These values are comparable or slightly higher than those reported in previous studies which assessed expert interobserver agreement for assessment of wall motion abnormalities[162,163]. DLSS to identified wall motion abnormalities with performance comparable to expert readers, with AUROC of 0.87 and accuracy of 84%. We further demonstrated the clinical potential of DLSS through visual analysis of two example cases of viral myocarditis and LBBB.

We have demonstrated the ability of DLSS to automatically quantify and detect regional wall motion abnormalities at a segmental level. Additionally, our normal ranges of strain, are comparable to those of previous studies, which assessed performance of traditional strain quantification methods. A large meta-analysis comparing DENSE, feature tracking, and feature tracking found mean global radial strain in normal subjects to be 24.3% (95% CI: 16.2 – 32.3%), 34.1% (95% CI: 28.5 – 39.7%), and 47.3% (95% CI: 43.6 – 51.0%), respectively [149]. Given that DLSS and feature tracking both use cine SSFP images as inputs, it is perhaps unsurprising that they have very similar normal ranges of strain. However, feature tracking requires expert manual segmentation of the endocardium and epicardium[164] and is known to suffer from considerable inter-vendor variability[52]. Our DLSS method requires no segmentations or manual interventions, permitting rapid and user-independent strain measurements. Additionally, while feature tracking has shown good reproducibility and interobserver agreement for global metrics of strain, it is less reliable for segmental metrics of strain[165,166]. We hypothesize that DLSS, trained using pixelwise velocity fields derived from 4D Flow MRI, is better equipped to infer segmental myocardial strain.

Several limitations should be considered. All training data were acquired at 3.0-T using an MRI scanner from a single vendor at our institution, which may be considered a limitation. However, we established normal ranges for the DLSS algorithm and evaluated its performance in a relatively broad population of normal subjects and clinical patients from a patients scanned on multiple 3.0 T and 1.5 T MRIs. This is evidence of that the method exhibited broader generalizability than might be expected. Prior works have similarly observed broader generalizability of image segmentation[10]and image enhancement[125] algorithms. Further work may be necessary to show broad generalizability to MRIs from multiple vendors. Additionally, we did not directly compare head-to-head performance of DLSS performance against other retrospective methods of assessing myocardial strain in this study. Although we did not compare to existing feature tracking methods, we felt it was more important to benchmark against expert radiologists, which to date has not been performed for other strain methods. Finally, we have only shown results for using DLSS to compute in-plane strain in short-axis cine SSFP images. Future work may include extension of the deep learning approach to long axis images for automated measurement of regional longitudinal strain and extension to the right ventricle.

In conclusion, computation of myocardial strain from cardiac MRI has traditionally required either dedicated acquisitions of strain imaging pulse sequences and/or significant manual post-processing. Furthermore, we observe that there have been few comparisons between existing methods and the clinical reference standard of visual assessment of focal wall motion abnormalities. DLSS is unique from previous approaches in that no fiducial markers or manual segmentations are required—instead, it performs the complex visual tasks of inferring myocardial velocity solely from anatomic image data over an entire cardiac cycle. DLSS performs fully-automated analysis of myocardial strain from historical imaging data, and may enable larger scale studies to study regional myocardial strain in many other disease states beyond ischemic heart disease.

5.7 Acknowledgements

We acknowledge Microsoft Azure and Oracle Cloud for their computational resources used to train our algorithms. Evan M. Masutani would like to acknowledge training grant funding from RSNA Medical Student Research Grant RMS2120, the American Heart Association Pre-Doctoral Fellowship 20PRE35180166, NIH T32GM007198, and NHLBI T32 HL105373. Rahul Chandrupatla is supported by the Altman Clinical and Translational Research Institute MedGap Program.

This chapter was adapted, in part, from “Feasibility of Deep Learning to Synthesize Outflow Hemodynamics from Cardiac MRI” in preparation for submission to Radiology. The author list is: Masutani, Evan; Chandrupatla, Rahul; Hahn, Lewis; Horowitz, Misha; Jacobs, Kathleen; Kligerman, Seth; Hsiao, Albert. The dissertation author was the primary investigator and author of this paper.

5.8 Appendix

5.8.1 DLSS Architecture

The DLSS CNN is a novel, bifurcated architecture designed by the lead-author to synthesize spatiotemporal myocardial velocity fields from short-axis cine SSFP images. Broadly, the CNN architecture comprises an encoder-decoder block based on the 3D UNet[61] which bifurcates into branches comprising a squeeze-excitation module[133] followed by 3D SRNet[84] block to generate myocardial segmentations and the velocity field. The encoder-decoder block receives as input 20 time frames with shape 192 x 192 pixels, which encompass the entire cardiac cycle. To integrate the periodic nature of the cardiac cycle into our CNN architecture, we introduce periodic 3D convolutional layers (pConv3D), which entail padding the temporal dimension with feature maps, rather than zero-padding, prior to convolution. For example, given a 3x3x3 convolutional kernel, we concatenate the feature maps from the 20th timepoint upstream of the feature maps from the 1st timepoint; likewise, we concatenate the feature maps from the 1st timepoint downstream of the feature maps from the 20th timepoint. Following each pConv3D layer, we employ Batch Normalization (BN) [167]. To account for varying temporal spacing between time frames, we multiply the output feature map of the encoder-decoder block by the patient heart rate. We then bifurcate our CNN using two squeeze-excitation blocks (SE Blocks) [133] followed by periodic 3D SRNet blocks (pSR Blocks) [84]. The first branch generates segmentations of the myocardium, and the second branch generates the velocity field. We then multiply these intermediate branches to obtain the myocardial velocity field. Subsequently, the DLSS CNN internally subtracts any pixelwise net displacement over the cardiac cycle to yield the corrected myocardial velocity field (Myocardial Correction Block).

5.8.2 Neural Network Training

We trained our DLSS CNN for 300 epochs using the Adam optimizer with a learning rate of 3e-5. For training, we employed an Oracle Cloud virtual machine equipped with eight A100 graphics cards with 40 GB of VRAM (Nvidia, Santa Clara, California). We used TensorFlow-GPU 2.4.3 (Google, Mountain View, California) with mixed-precision for all deep-learning experiments.

5.8.3 Loss Functions

For the following mathematical expressions, we denote each prong's output inference as $\hat{y}$ and its corresponding ground truth as y.

5.8.4 Segmentation Loss

For cardiac chamber segmentation, we employed the Dice loss function with a smoothing factor of 1[81].

5.8.5 Velocity Synthesis Loss

For myocardial velocity field synthesis, we built a custom loss function incorporating the structural similarity index (SSIM)[87] at each timepoint, piecewise linear regression for each component of velocity, and physical constraints. We first define our piecewise linear regression function:

Given 1D vectors of inferred, $\hat{x}$, and ground truth, x, values, solution of the normal equation yields coefficients defining the best-fit linear regression[134]: For example:

We first generate a matrix $A = \begin{bmatrix} 1 & x_1 \\ \vdots & \vdots \\ 1 & x_N \end{bmatrix}$ and a column vector $\hat{x} = \begin{bmatrix} \hat{x}_1 \\ \vdots \\ \hat{x}_N \end{bmatrix}$

Solving $(A^TA)^{-1}A^T\hat{x}$ yields the coefficient matrix, $\hat{\theta} = \begin{bmatrix}\hat{m}_0 \\ \hat{m}_1\end{bmatrix}$, such that $\hat{m}_1 x + \hat{m}_0$ defines the least-squares best-fit line. Given objective coefficients, $\theta = \begin{bmatrix}m_0 \\ m_1\end{bmatrix}$, the loss function takes the form of $\sum\left(\theta - \hat{\theta}\right)^2$. We set our objective coefficient matrix to be $\theta = \begin{bmatrix}0 \\ 1\end{bmatrix}$ such that we approach $\hat{x} = x$.

We then incorporate two physical constraints into our loss function: 1) net-zero displacement over the cardiac cycle, and 2) net-zero strain over the cardiac cycle. We define pixelwise net displacement as:

$$d_i = \sum_0^T v_i\,(t)$$

Where i denotes direction, d is displacement over the cardiac cycle, v is velocity, t is time, and T is the total number of time frames. We enforce net-zero displacement, summed over all pixels, via:

$$Displacement\ Loss = \sum |d_i|$$

To approximate strain, we apply the Sobel operator to our net displacement. We enforce non-zero net strain over the cardiac cycle, summed over all pixels, via:

$$Strain\ Loss = \sum |\varepsilon_i|$$

Where i denotes direction and ε is net strain over the cardiac cycle

Thus, our velocity loss function took the general form of:

$$Velocity\ Loss = a_1 \sum |d_i| + \ a_2 \sum |\varepsilon_i| + a_3 \sum_i^c (1 - SSIM(y_i, \hat{y}_i)) + a_4 \sum_i^c \left(\theta_i - \hat{\theta}_i\right)^2$$

Where c comprises the row and column components of velocity, with weighing factors:

$a_1 = a_2 = 1.356 * 10^{-6},\ a_3 = 0.05,\ a_4 = 10^{-2}$. Note that a_1 and a_2 are equal to $\frac{1}{Rows*Columns*Time}$, where $Rows$ are the number of pixels in the row dimension, $Columns$ are the number of pixels in the column dimension, and $Time$ are the number of time frames.

5.8.6 Loss Function Weighing

For training, we scaled each component loss function such that their values were of similar scale. We weighed segmentation loss and velocity synthesis loss by factors of 1 and 0.05, respectively. Our final loss function is, therefore:

$$Loss = Segmentation\ Loss + 0.05(Velocity\ Loss)$$

5.8.7 Calculation of Strain-Rate and Strain

Myocardial velocity ($\vec{v}$), myocardial strain rate (SR), and myocardial strain (ε) are related in the following manner[168]:

$$(1)\ SR(t) = \frac{\partial \vec{v}_x(t)}{\partial x}$$

$$(2)\ \varepsilon(t) = \int_{t_0}^{t} SR\ dt$$

Where x is the direction of interest e.g., radial or circumferential, t is an arbitrary timepoint, and t_0 is the end-diastolic timepoint. Solving equations (1) and (2) numerically using second-order finite differences and Riemann sums, respectively, yielded strain rate and strain fields, which were then averaged over each AHA segment[169]. Global radial strain (GRS) represents the average of all 16 non-apex AHA segments; GRS was not reported for acquisitions missing any segment.

5.9 Supplemental Tables, Figures, and Videos

Supplemental Table 1: *Data for short axis cine SSFP parameters presented as means with ranges in parentheses.*

Imaging Parameter	Normal Volunteer MRI (n=21)	Normal Clinical MRI (n=19)	Ischemic Heart Disease (n=53)
Temporal resolution (msec)	43 (40 to 50)	54 (27 to 68)	57 (42 to 92)
Spatial resolution (mm)			
Frequency	1.84 (1.61 to 1.98)	1.60 (1.25 to 2.30)	1.60 (1.33 to 2.38)
Phase	1.86 (1.61 to 1.98)	1.83 (1.60 to 2.30)	1.82 (1.70 to 2.13)
Slice	8 (8 to 8)	8.95 (8 to 10)	8.19 (8 to 10)

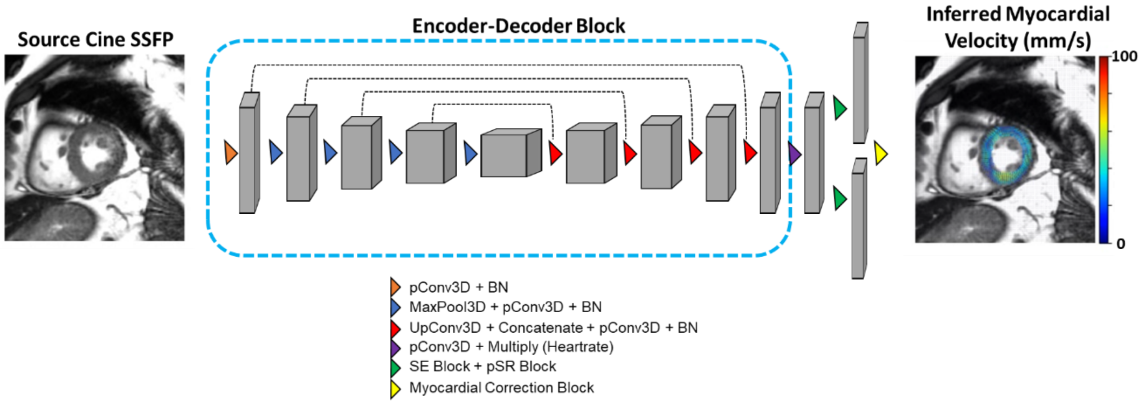

Supplemental Figure 4: *Details of the DLSS CNN Architecture.* The DLSS CNN is a deep multi-prong convolutional neural network which synthesizes myocardial velocity fields from input cine SSFP images. Refer to Supporting Information Text for in-depth details.

Supplemental Video 4: *Overview of the deep learning synthetic strain (DLSS) approach*. A CNN was trained to infer myocardial velocities from a series of cine SSFP images. Training data included co-registered myocardial velocities from cardiac MRIs from 219 patients who underwent 4D Flow as part of their clinical exam. The inferred myocardial velocities are then used to calculate myocardial strain rate and strain maps, which are superimposed on the source SSFP images for quantification and visual interpretation.

Supplemental Video 5: *Exemplar case of a patient with catheter angiogram-proven LAD occlusion.* There is focal wall motion abnormality of the anteroseptal (blue arrow) and inferoseptal (purple arrow) walls with decreased peak radial strain and strain rate. Corresponding strain and strain rate curves show the severity of this abnormality relative to the other myocardial segments in the same slice. Following intravenous contrast administration, the septal wall shows a matching perfusion defect and transmural delayed enhancement, indicating myocardial ischemia and infarction.

Supplemental Video 6: *Patient with cardiac arrest 4 months prior with viral prodrome and presumed myocarditis with negative myocardial biopsy.* There is hypokinesis of the mid anteroseptal (blue arrow) and anterior (green arrow) wall evident on DLSS-derived peak radial strain rate and strain maps. Following administration of intravenous contrast, there is only subtle mesocardial enhancement of the mid anteroseptal wall. Without DLSS strain maps, this was initially interpreted clinically as a normal cardiac MRI.

Supplemental Video 7: *Ventricular dyssynchrony with dissociation of contraction of the septal and lateral walls due to left bundle branch block, visualized and quantified with DLSS.* Early in the cardiac cycle, while the anterolateral wall contracts, the inferoseptal wall relaxes. Strain rate curves highlight the dissociation between these segments.

Chapter 6. Conclusions and Future Directions

6.1 Summary

With this dissertation, I have shown that deep learning can perform image synthesis for cardiac MRI. Additionally, I have demonstrated the necessary CNN architectural modifications required to progressively synthesize scalar fields, static vector fields, spatiotemporal vector fields, and finally spatiotemporal tensor fields.

In my first chapter, I hypothesized that existing CNNs, commonly used for simpler computer vision tasks, could be adapted to perform image super-resolution of medical images. I found that all tested CNNs, when trained to specifically enhance spatial resolution using synthetically generated datasets, significantly outperformed conventional methods of image upscaling. Clinically, I demonstrated that CNNs could super-resolve small matrix short-axis cine SSFP MRI acquisitions and that the resulting volumetric measurements were not significantly different than volumetric measurements of full-resolution images. Finally, I demonstrated that I could super-resolve full-resolution MR images and further enhance spatial detail beyond what is typically acquired. I have therefore shown that CNNs can effectively perform image synthesis of scalar fields and have specifically established the UNet and SRNet as candidate architectures to iteratively improve to tackle more complex image synthesis problems.

In my second chapter, I aimed to improve the kt-UNet from my first chapter to perform background phase error correction of 4D Flow MRI. By incorporating hyperbolic tangent activation functions and multiple output channels, I could now predict negative values and multiple vector components, respectively, which together permit synthesis of static vector fields. Flow measurements from CNN-corrected datasets significantly and very strongly correlated with manually corrected measurements. Furthermore, CNN-correction significantly reduced inflow-outflow bias and variance. I have therefore shown that CNNs can effectively perform image synthesis of static vector fields through modification of the kt-UNet architecture.

In my third chapter, I aimed to incorporate spatiotemporal information into the phase error correction CNN architecture to synthesize dynamic blood flow fields from cine SSFP timeseries. Blood flow is the biomechanical consequence of ventricular contraction. Therefore, I reasoned that a multi-task CNN which also learned cardiac morphology would stand a better chance of inferring blood flow. To achieve this, I developed a trifurcated multi-task architecture I named Triton-Net, which simultaneously localized anatomical landmarks, segmented cardiac chambers, and synthesized blood flow fields from input adjacent cine SSFP timeframes. Notably, I combined both UNet and SRNet architectures from my first aim to execute the trifurcation. I also introduced the concept of using the Moore-Penrose inverse as a component of the loss function to give greater weight to pixels with higher velocity. Overall, I found moderate and significant correlation between Triton-Net synthesized velocities and acquired 4D Flow MRI velocities. Clinically, I sought to use the synthesized blood flow velocities to calculate the pressure gradient at the left ventricular outflow tract to detect obstructive disease. I found that Triton-Net could detect outflow obstruction with an AUROC of 0.830 based on these pressure gradient measurements. I have therefore shown that CNNs can effectively perform image synthesis of dynamic vector fields through extensive modifications of the phase error correction CNN.

Finally, in my fourth chapter, I aimed to further refine Triton-Net with additional physical constraints to synthesize myocardial velocities, strain rate, and strain fields from cine SSFP timeseries. Realizing that the cardiac cycle is inherently periodic, with no net displacement or strain over successive heartbeats, I sought to integrate these physical constraints into the Triton-Net architecture. To accomplish this, I connected the segmentation and flow synthesis prongs of Triton-Net via multiplication to yield myocardial velocity fields. I then modified the convolutional layers themselves to allow processing of the entire cardiac cycle, which enabled me to subtract any net myocardial displacement within the CNN architecture. Lastly, I added net-zero displacement and strain as components of the overall loss function; together, these substantial upgrades yielded the DLSS architecture. To establish segmental and global normal ranges for DLSS, I measured radial and circumferential strain in a normal population of 21 healthy volunteers and 19 patients with normal cardiac MRI. To demonstrate clinical utility, I sought to detect wall motion abnormalities in an ischemic heart disease population using the DLSS technique. After generating a consensus ground truth for each segment based on ratings from four cardiothoracic radiologists, I determined that DLSS could detect wall motion abnormalities with performance comparable to expert readers. I have therefore shown that CNNs can effectively perform image synthesis of dynamic tensor fields by incorporating physical constraints into the Triton-Net framework.

6.2 Future Directions

6.2.1 Overview

Over the course of my dissertation, I have progressively upgraded my CNN armamentarium to tackle more complex clinical problems, beginning with image super-resolution and ending with inference of cardiac biomechanics. Broadly, I envision expanding this work in the following domains: 1) refinement of CNN architecture to improve the results of the discussed aims, 2) application of image synthesis to other complementary imaging modalities and additional organs, and 3) characterization of the biomechanics of healthy and diseased tissues to augment clinical diagnosis and management.

6.2.2 Technical Innovations

We could potentially use variants of the final DLSS architecture in the previous aims to yield more accurate results and further augment analysis of cardiac MRI. In super-resolution, we previously restricted our task to recovering high spatial frequency detail in k-space. With a multi-pronged CNN, we could super-resolve low-resolution cine SSFP images, generate myocardial segmentations, and synthesize myocardial velocity and strain fields. Learning the implicit biomechanical relationships required to perform segmentation and flow synthesis would likely improve the sharpness of super-resolved myocardial edges. Perhaps more importantly, we would automate two vital components of cardiac MRI analysis: quantification of volumetry via ventricular segmentation and evaluation of wall motion abnormalities via strain synthesis.

We could apply a similar approach for improving phase error correction. As mentioned in aim 2, we typically employ manual segmentation of 4D Flow acquisition to locate static tissue voxels from which we may model background phase error. While we opted for a purely image synthesis approach to estimate pixelwise background, generating segmentations of static tissue may further improve results. Specifically, we could first integrate the polynomial regression of the synthesized phase error maps into the CNN architecture, similar to how I incorporated weighted linear regression into the loss function of aim 3. An additional static tissue segmentation output could then provide weights for this polynomial regression: we would explicitly encode the CNN to avoid non-static tissue. The segmentation output would also aid explainability of the outputs, as poor segmentations of static tissue would imply unreliable phase error results. Extending this idea further, we could also generate segmentations of the relevant vasculature, from which we may perform automated flow measurements. Thus, a DLSS-type CNN would simultaneously correct background phase error and automate hemodynamic analyses of large 4D Flow MRI datasets.

While we have immediate potential to incrementally augment cardiac MRI by slightly modifying the DLSS architecture, we will likely realize larger gains by incorporating additional physical constraints, particularly conservation laws, into model design, as exemplified by aim 4. However, the heart is naturally a spatiotemporal object, which means accurate modeling of biomechanics requires four dimensions. In all aims we have only analyzed, at most, three dimensions largely due to technical limitations. First, while 4D convolutions are a straightforward extension of 3D convolutions, only a few studies have examined their use[170,171]. This may be partly due to their relatively large memory consumption: the number of model weights scale exponentially with increasing dimensionality. While one valid approach is to simply wait for computational hardware to meet this intense memory demand, there are architectural innovations in the literature which may make these higher-dimensional neural networks viable.

Often, the anatomy of interest comprises a relatively small fraction of the field of view e.g., myocardial voxels within the entire short-axis cine SSFP stack for inference of myocardial strain. One method to reduce memory overhead is to leverage this inherent data sparsity: after an initial segmentation, we could isolate voxels of interest for convolution and ignore the remainder. Previous work by Ren, et al.[172] suggests this may be possible in a CNN framework they named Sparse Block Network (SBNet). These authors demonstrated that, given an input image and affiliated binary mask, they could leverage gather and scatter operations which would isolate blocks of relevant voxels for convolution, then replace the outputs into a sparse tensor, respectively. A drawback of this method is the requirement to subdivide any masks into uniform rectangular chunks *a priori*, which could be problematic for highly irregular anatomy. Another approach to reduce memory overhead is to apply compression; rather than ignoring regions, methods like octree compression effectively pool similar voxels into larger voxels, thereby reducing both the number of operations required and the memory consumption of inputs and feature maps[173]. Work by Gupta, et al.[174] has shown that combining octree compression in the CNN architecture (OctNet) for segmentation of cardiac CT significantly outperformed conventional image downsampling while consuming a fraction of GPU memory. A potential limitation of OctNet is that the octree compression method is lossy: the pooling operation reduces the local spatial resolution depending on the degree of compression.

Another promising method to reduce memory overhead is the graph convolutional neural network (GCNN). GCNNs do not operate on Cartesian grids; instead, they operate on graphs, which comprise multiple nodes and a map of their k-nearest neighbor connectivity. Effectively, GCNNs perform convolution on unstructured data e.g., point clouds[175,176]. Given a starting cardiac cine SSFP series and affiliated myocardial segmentation, we could potentially isolate the myocardial voxels and represent them as an unstructured point cloud for input to an image synthesis GCNN. Similar to the SBNet approach, we would substantially reduce memory overhead by discarding irrelevant voxels from analysis while maintaining full spatiotemporal resolution. While previous work has shown good performance of GCNNs to perform 3D segmentation[175,176], their extension to image synthesis and analysis of four-dimensional objects remains unknown.

6.2.3 Generalizability to Other Modalities and Organs

While my dissertation has specifically focused on image synthesis for cardiac MRI, it is possible that we may achieve similar results across modalities and organ systems. While cardiac MRI is the gold standard for evaluation of morphology, flow, and function, echocardiography and computed tomography (CT) are more widely available and are often first-line clinically for evaluating cardiac disease.

Echocardiography, a form of ultrasound, emits sound waves and measures how long it takes echoes, reflected off tissues, to return to the probe. The distances between the probe and tissues are then calculated, which permits image formation. Additionally, we can also evaluate hemodynamics through color Doppler ultrasound[4]. As a result, ultrasound may produce analogous images, from which volumetry, blood flow, and regional function are calculated clinically. Indeed, CNNs have been applied with great effect for classification of echocardiogram views[177], segmentation of cardiac chambers[178], and regression of ventricular function[123]. I hypothesize that we could use the same Triton-Net and DLSS architectures to infer blood flow and myocardial motion from echocardiograms, using color Doppler velocimetry as ground truth. However, it is known that color Doppler velocities are significantly less-reliable than those obtained by phase-contrast MRI[90]; therefore, to generate a stronger ground truth, we could re-slice and co-register patient-matched 4D Flow-derived vector fields onto echocardiograms.

We may use a similar approach for CT. Like MRI and echocardiography, CT can also produce spatiotemporal images of cardiac morphology. As a modality, CT measures the local tissue attenuation coefficient to incident x-ray radiation[4]. However, there are currently no methods to directly quantify blood or myocardial motion; additionally, CT employs carcinogenic, ionizing radiation, limiting the amount of data which may be acquired during a given scan[179]. As with echocardiography, we could simply re-slice and co-register patient-matched 4D Flow MRI data with the CT scans to serve as ground truth for direct synthesis of blood and myocardial velocity fields. We could also attempt to limit the radiation dose via image synthesis, where we simulate low-dose CT from existing scans by synthesizing noise and train a CNN to synthesize the uncorrupted image.

In addition to cross-modality application, we could easily apply the same image synthesis pipeline to other organ systems. Already, we have seen that we can apply background phase-error correction to the abdominopelvic vasculature in aim 2. We could apply the same CNN to removal of phase error from 4D Flow scans of the brain, heart, pulmonary vasculature, and peripheral vasculature. Similarly, we may apply the super-resolution concept across many MRI scans, which, in conjunction with a segmentation output, could be crucial for demarcating tumors with poorly visualized boundaries, such as pancreatic adenocarcinoma[180].

6.2.4 Image Synthesis for Biomechanical Discovery

In aims 3 and 4, I demonstrated the ability of Triton-Net and DLSS to identify disease based on peak outflow gradient and peak radial segmental strain, respectively.

While these metrics may be calculated manually, annotation is a time-consuming process which severely limits the throughput of population-based analyses. Our fully automated image synthesis methods permit the rapid characterization of various biomechanical characteristics such as peak strain, mean strain, time to peak strain, etc. Therefore, the immediate applicability of image synthesis networks is to tabulate meaningful biomechanical metrics in healthy and diseased populations and determine their value in diagnosis, management, and prognostication. For example, in Tetralogy of Fallot (ToF), individuals are born with a ventricular septal defect, pulmonary stenosis, overriding aorta, and right ventricular hypertrophy, and typically receive corrective surgery shortly after birth. However, despite surgical correction, these patients are at increased risk for right ventricular failure and potentially fatal ventricular arrythmia[181]. While conventional global volumetric metrics like increased right ventricular end-diastolic and end-systolic volumes are important for prognosis[182], recent studies have identified right ventricular akinesis as an even stronger predictor of ventricular arrythmia[183]. Therefore, DLSS characterization of segmental strain in a ToF population could permit automated stratification of at-risk patients based on right ventricular strain metrics. In previous analyses, we have largely relied on peak segmental radial strain to detect disease. It is possible that related metrics e.g., relative dyssynchrony between segments and time to peak strain[184], may provide even better prognostication value. As we gain a better understanding of biomechanics in healthy and diseased populations, we will be able to build more robust statistical models to sub-classify and manage patients with congenital heart disease.

6.3 Conclusion

In conclusion, I have demonstrated broad applicability of deep learning image synthesis in cardiovascular MRI. We have seen the ability of image synthesis CNNs to infer data of progressively higher dimensionality, from scalars to tensor fields. Current limitations of this approach are partly due to computational constraints: full analysis of volumetric, time-varying systems requires some form of 4D analysis, which are currently difficult to implement. Furthermore, as with all forms of deep learning, the training process is inherently data intensive. While we may achieve high performance with relatively small, but highly curated and annotated dataset[64], highly specialized datasets, such as 4D Flow MRI, may be rare outside of academic clinical settings[62]. Nevertheless, research institutions with access to these datasets can train these image synthesis CNNs to maximally extract biomechanical and, ultimately, clinically useful data from routine scans. Distributing these CNNs to the greater medical community could therefore augment clinical interpretation of routine scans without necessitating increased acquisition times, advanced pulse sequences, or additional manual annotation. It is the author's sincere hope that this and related works will increase the quality of patient care and lead to a brighter and healthier future.

WORKS CITED:

1. Lauterbur PC. Image Formation by Induced Local Interactions: Examples Employing Nuclear Magnetic Resonance. *Nature 1973 242:5394*. 1973;242(5394):190-191. doi:10.1038/242190a0

2. Mansfield P. Multi-planar image formation using NMR spin echoes. *Journal of Physics C: Solid State Physics*. 1977;10(3):L55. doi:10.1088/0022-3719/10/3/004

3. Damadian R. Tumor detection by nuclear magnetic resonance. *Science (New York, NY)*. 1971;171(3976):1151-1153. doi:10.1126/SCIENCE.171.3976.1151

4. Prince JL, Links JM. *Medical Imaging Signals and Systems*. 2nd ed. Pearson Prentice Hall; 2014.

5. Feng L, Srichai MB, Lim RP, Harrison A, King W, Adluru G, Dibella EVR, Sodickson DK, Otazo R, Kim D. Highly accelerated real-time cardiac cine MRI using *k - t* SPARSE-SENSE. *Magnetic Resonance in Medicine*. 2013;70(1):64-74. doi:10.1002/mrm.24440

6. Moran PR, Moran RA, Karstaedt N. Verification and evaluation of internal flow and motion. True magnetic resonance imaging by the phase gradient modulation method. *Radiology*. 1985;154(2):433-441. doi:10.1148/RADIOLOGY.154.2.3966130

7. Markl M, Chan FP, Alley MT, Wedding KL, Draney MT, Elkins CJ, Parker DW, Wicker R, Taylor CA, Herfkens RJ, Pelc NJ. Time-resolved three-dimensional phase-contrast MRI. *J Magn Reson Imaging*. 2003;17(4):499-506. doi:10.1002/jmri.10272

8. Carr JC, Simonetti O, Bundy J, Li D, Pereles S, Finn JP. Cine MR angiography of the heart with segmented true fast imaging with steady-state precession. *Radiology*. 2001;219(3):828-834. doi:10.1148/RADIOLOGY.219.3.R01JN44828

9. Gerche A la, Claessen G, van de Bruaene A, Pattyn N, van Cleemput J, Gewillig M, Bogaert J, Dymarkowski S, Claus P, Heidbuchel H. Cardiac MRI. *Circulation: Cardiovascular Imaging*. 2013;6(2):329-338. doi:10.1161/CIRCIMAGING.112.980037

10. Tao Q, Yan W, Wang Y, Paiman EHM, Shamonin DP, Garg P, Plein S, Huang L, Xia L, Sramko M, Tintera J, de Roos A, Lamb HJ, van der Geest RJ. Deep Learning–based Method for Fully Automatic Quantification of Left Ventricle Function from Cine MR Images: A Multivendor, Multicenter Study. *Radiology*. 2019;290(1):81-88. doi:10.1148/radiol.2018180513

11. Dyverfeldt P, Bissell M, Barker AJ, Bolger AF, Carlhäll CJ, Ebbers T, Francios CJ, Frydrychowicz A, Geiger J, Giese D, Hope MD, Kilner PJ, Kozerke S, Myerson S, Neubauer S, Wieben O, Markl M. 4D cardiovascular magnetic resonance velocity

mapping of alterations of right heart flow patterns and main pulmonary artery hemodynamics in tetralogy of Fallot. Published online 2012. doi:10.1186/s12968-015-0174-5

12. Hsiao A, Alley MT, Massaband P, Herfkens RJ, Chan FP, Vasanawala SS. Improved cardiovascular flow quantification with time-resolved volumetric phase-contrast MRI. *Pediatric Radiology*. 2011;41(6):711-720. doi:10.1007/s00247-010-1932-z

13. Koch R, Lang RM, Garcia MJ, Weinert L, Bednarz J, Korcarz C, Coughlan B, Spiegel A, Kaji E, Spencer KT, Mor-Avi V. Objective evaluation of regional left ventricular wall motion during dobutamine stress echocardiographic studies using segmental analysis of color kinesis images. *Journal of the American College of Cardiology*. 1999;34(2):409-419. doi:10.1016/S0735-1097(99)00233-8

14. Salerno M, Sharif B, Arheden H, Kumar A, Axel L, Li D, Neubauer S. Recent Advances in Cardiovascular Magnetic Resonance Techniques and Applications. *Circulation Cardiovascular imaging*. 2017;10(6). doi:10.1161/CIRCIMAGING.116.003951

15. Fryar CD, Chen TC, Li X. Prevalence of uncontrolled risk factors for cardiovascular disease; United States, 1999-2010. *NCHS data brief*. 2012;(103):1-8. Accessed February 15, 2022. https://stacks.cdc.gov/view/cdc/13600

16. Teng EL, Masutani EM, Yeoman B, Fung J, Lian R, Ngo B, Kumar A, Placone JK, lo Sardo V, Engler AJ. High shear stress enhances endothelial permeability in the presence of the risk haplotype at 9p21.3. *APL Bioengineering*. 2021;5(3):036102. doi:10.1063/5.0054639

17. lo Sardo V, Chubukov P, Ferguson W, Kumar A, Teng EL, Duran M, Zhang L, Cost G, Engler AJ, Urnov F, Topol EJ, Torkamani A, Baldwin KK. Unveiling the Role of the Most Impactful Cardiovascular Risk Locus through Haplotype Editing. *Cell*. 2018;175(7):1796-1810.e20. doi:10.1016/j.cell.2018.11.014

18. Sirajuddin A, Mirmomen SM, Kligerman SJ, Groves D, Burke AP, Kureshi F, White CS, Arai AE. Ischemic heart disease: Noninvasive imaging techniques and findings. *Radiographics*. 2021;41(4):990-1021. doi:10.1148/RG.2021200125/ASSET/IMAGES/LARGE/RG.2021200125.FIG26.JPEG

19. Retson TA, Masutani EM, Golden D, Hsiao A. Clinical Performance and Role of Expert Supervision of Deep Learning for Cardiac Ventricular Volumetry: A Validation Study. *Radiology: Artificial Intelligence*. 2020;2(4):e190064. doi:10.1148/ryai.2020190064

20. West AM, Kramer CM. Cardiovascular Magnetic Resonance Imaging of Myocardial Infarction, Viability, and Cardiomyopathies. *Current problems in cardiology*. 2010;35(4):176. doi:10.1016/J.CPCARDIOL.2009.12.002

21. Coelho-Filho OR, Rickers C, Kwong RY, Jerosch-Herold M. MR myocardial perfusion imaging. *Radiology*. 2013;266(3):701-715. doi:10.1148/RADIOL.12110918/ASSET/IMAGES/LARGE/110918FIG05B.JPEG

22. Allman KC, Shaw LJ, Hachamovitch R, Udelson JE. Myocardial viability testing and impact of revascularization on prognosis in patients with coronary artery disease and left ventricular dysfunction: a meta-analysis. *Journal of the American College of Cardiology*. 2002;39(7):1151-1158. doi:10.1016/S0735-1097(02)01726-6

23. Gutberlet M, Fröhlich M, Mehl S, Amthauer H, Hausmann H, Meyer R, Siniawski H, Ruf J, Plotkin M, Denecke T, Schnackenburg B, Hetzer R, Felix R. Myocardial viability assessment in patients with highly impaired left ventricular function: Comparison of delayed enhancement, dobutamine stress MRI, end-diastolic wall thickness, and TI201-SPECT with functional recovery after revascularization. *European Radiology*. 2005;15(5):872-880. doi:10.1007/S00330-005-2653-9/FIGURES/5

24. Minette MS, Sahn DJ. Ventricular septal defects. *Circulation*. 2006;114(20):2190-2197. doi:10.1161/CIRCULATIONAHA.106.618124

25. Vasanawala SS, Hanneman K, Alley MT, Hsiao A. Congenital heart disease assessment with 4D flow MRI. *Journal of Magnetic Resonance Imaging*. 2015;42(4):870-886. doi:10.1002/jmri.24856

26. Backer CL, Winters RC, Zales VR, Takami H, Muster AJ, Benson DW, Mavroudis C. Restrictive ventricular septal defect: How small is too small to close? *The Annals of Thoracic Surgery*. 1993;56(5):1014-1019. doi:10.1016/0003-4975(95)90006-3

27. Xue H, Kellman P, LaRocca G, Arai AE, Hansen MS. High spatial and temporal resolution retrospective cine cardiovascular magnetic resonance from shortened free breathing real-time acquisitions. *Journal of Cardiovascular Magnetic Resonance*. 2013;15(1):102. doi:10.1186/1532-429X-15-102

28. Yanhua Wang, Ying L. Compressed Sensing Dynamic Cardiac Cine MRI Using Learned Spatiotemporal Dictionary. *IEEE Transactions on Biomedical Engineering*. 2014;61(4):1109-1120. doi:10.1109/TBME.2013.2294939

29. Kocaoglu M, Pednekar AS, Wang H, Alsaied T, Taylor MD, Rattan MS. Breath-hold and free-breathing quantitative assessment of biventricular volume and function using compressed SENSE: A clinical validation in children and young adults. *Journal of Cardiovascular Magnetic Resonance*. 2020;22(1):1-11. doi:10.1186/S12968-020-00642-Y/FIGURES/4

30. Setser RM, Fischer SE, Lorenz CH. Quantification of left ventricular function with magnetic resonance images acquired in real time. *Journal of Magnetic Resonance Imaging*. 2000;12(3):430-438. doi:10.1002/1522-2586(200009)12:3<430::AID-JMRI8>3.0.CO;2-V

31. Hope MD, Sedlic T, Dyverfeldt P. Cardiothoracic magnetic resonance flow imaging. *Journal of Thoracic Imaging*. 2013;28(4):217-230. doi:10.1097/RTI.0B013E31829192A1

32. Dyvorne H, Knight-Greenfield A, Jajamovich G, Besa C, Cui Y, Stalder A, Markl M, Taouli B. Abdominal 4D flow MR imaging in a breath hold: Combination of spiral sampling and dynamic compressed sensing for highly accelerated acquisition. *Radiology*. 2015;275(1):245-254. doi:10.1148/RADIOL.14140973/ASSET/IMAGES/LARGE/RADIOL.14140973.FIG4.JPEG

33. Pereira VM, Delattre B, Brina O, Bouillot P, Vargas MI. 4D flow MRI in neuroradiology: Techniques and applications. *Topics in Magnetic Resonance Imaging*. 2016;25(2):81-87. doi:10.1097/RMR.0000000000000082

34. Callaghan FM, Burkhardt B, Geiger J, Valsangiacomo Buechel ER, Kellenberger CJ. Flow quantification dependency on background phase correction techniques in 4D-flow MRI. *Magnetic Resonance in Medicine*. 2020;83(6):2264-2275. doi:10.1002/MRM.28085

35. Viola F, Dyverfeldt P, Carlhäll CJ, Ebbers T. Data Quality and Optimal Background Correction Order of Respiratory-Gated k-Space Segmented Spoiled Gradient Echo (SGRE) and Echo Planar Imaging (EPI)-Based 4D Flow MRI. *Journal of Magnetic Resonance Imaging*. 2020;51(3):885-896. doi:10.1002/JMRI.26879

36. Gatehouse P, Rolf M, Graves M, Hofman M, Totman J, Werner B, Quest R, Liu Y, von Spiczak J, Dieringer M, Firmin D, van Rossum A, Lombardi M, Schwitter J, Schulz-Menger J, Kilner P. Flow measurement by cardiovascular magnetic resonance: a multi-centre multi-vendor study of background phase offset errors that can compromise the accuracy of derived regurgitant or shunt flow measurements. *Journal of cardiovascular magnetic resonance : official journal of the Society for Cardiovascular Magnetic Resonance*. 2010;12(1). doi:10.1186/1532-429X-12-5

37. Hofman MBM, Rodenburg MJA, Markenroth Bloch K, Werner B, Westenberg JJM, Valsangiacomo Buechel ER, Nijveldt R, Spruijt OA, Kilner PJ, van Rossum AC, Gatehouse PD. In-vivo validation of interpolation-based phase offset correction in cardiovascular magnetic resonance flow quantification: A multi-vendor, multi-center study. *Journal of Cardiovascular Magnetic Resonance*. 2019;21(1):1-13. doi:10.1186/S12968-019-0538-3/FIGURES/6

38. Jehenson P, Westphal M, Schuff N. Analytical method for the compensation of eddy-current effects induced by pulsed magnetic field gradients in NMR systems. *Journal of Magnetic Resonance (1969)*. 1990;90(2):264-278. doi:10.1016/0022-2364(90)90133-T

39. Markl M, Bammer R, Alley MT, Elkins CJ, Draney MT, Barnett A, Moseley ME, Glover GH, Pelc NJ. Generalized reconstruction of phase contrast MRI: Analysis

and correction of the effect of gradient field distortions. *Magnetic Resonance in Medicine*. 2003;50(4):791-801. doi:10.1002/MRM.10582

40. Bernstein MA, Zhou XJ, Polzin JA, King KF, Ganin A, Pelc NJ, Glover GH. Concomitant gradient terms in phase contrast MR: Analysis and correction. *Magnetic Resonance in Medicine*. 1998;39(2):300-308. doi:10.1002/MRM.1910390218

41. Busch J, Giese D, Kozerke S. Image-based background phase error correction in 4D flow MRI revisited. *Journal of Magnetic Resonance Imaging*. 2017;46(5):1516-1525. doi:10.1002/JMRI.25668

42. Hsiao A, Lustig M, Alley MT, Murphy MJ, Vasanawala SS. Evaluation of Valvular Insufficiency and Shunts with Parallel-imaging Compressed-sensing 4D Phase-contrast MR Imaging with Stereoscopic 3D Velocity-fusion Volume-rendered Visualization. *Radiology*. 2012;265(1):87-95. doi:10.1148/radiol.12120055

43. Stankovic Z, Allen BD, Garcia J, Jarvis KB, Markl M. 4D PC flow. *Cardiovascular*. 2014;4(2):173-192. doi:10.3978/j.issn.2223-3652.2014.01.02

44. Sharir T, Berman DS, Waechter PB, Areeda J, Kavanagh PB, Gerlach J, Kang X, Germano G. Quantitative Analysis of Regional Motion and Thickening by Gated Myocardial Perfusion SPECT: Normal Heterogeneity and Criteria for Abnormality. *THE JOURNAL OF NUCLEAR MEDICINE •*. 2001;42(11):1630-1638.

45. Lang RM, Bierig M, Devereux RB, Flachskampf FA, Foster E, Pellikka PA, Picard MH, Roman MJ, Seward J, Shanewise JS, Solomon SD, Spencer KT, St John Sutton M, Stewart WJ. Recommendations for Chamber Quantification: A Report from the American Society of Echocardiography’s Guidelines and Standards Committee and the Chamber Quantification Writing Group, Developed in Conjunction with the European Association of Echocardiography, a Branch of the European Society of Cardiology. *Journal of the American Society of Echocardiography*. 2005;18(12):1440-1463. doi:10.1016/J.ECHO.2005.10.005

46. Flachskampf FA, Schmid M, Rost C, Achenbach S, Demaria AN, Daniel WG. Cardiac imaging after myocardial infarction. *European Heart Journal*. 2011;32(3):272-283. doi:10.1093/EURHEARTJ/EHQ446

47. Zerhouni EA, Parish DM, Rogers WJ, Yang A, Shapiro EP. Human heart: tagging with MR imaging--a method for noninvasive assessment of myocardial motion. *Radiology*. 1988;169(1):59-63. doi:10.1148/RADIOLOGY.169.1.3420283

48. Auger DA, Zhong X, Epstein FH, Spottiswoode BS. Mapping right ventricular myocardial mechanics using 3D cine DENSE cardiovascular magnetic resonance. *Journal of Cardiovascular Magnetic Resonance*. 2012;14(1):1-9. doi:10.1186/1532-429X-14-4/FIGURES/7

49. Korosoglou G, Gitsioudis G, Voss A, Lehrke S, Riedle N, Buss SJ, Zugck C, Giannitsis E, Osman NF, Katus HA. Strain-encoded cardiac magnetic resonance during high-dose dobutamine stress testing for the estimation of cardiac outcomes: comparison to clinical parameters and conventional wall motion readings. *Journal of the American College of Cardiology*. 2011;58(11):1140-1149. doi:10.1016/J.JACC.2011.03.063

50. Osman NF, Prince JL. Visualizing myocardial function using HARP MRI. *Physics in medicine and biology*. 2000;45(6):1665-1682. doi:10.1088/0031-9155/45/6/318

51. Maret E, Todt T, Brudin L, Nylander E, Swahn E, Ohlsson JL, Engvall JE. Functional measurements based on feature tracking of cine magnetic resonance images identify left ventricular segments with myocardial scar. *Cardiovascular Ultrasound*. 2009;7(1):1-14. doi:10.1186/1476-7120-7-53/TABLES/5

52. Backhaus SJ, Metschies G, Zieschang V, Erley J, Mahsa Zamani S, Kowallick JT, Lapinskas T, Pieske B, Lotz J, Kutty S, Hasenfuß G, Kelle S, Schuster A. Head-to-head comparison of cardiovascular MR feature tracking cine versus acquisition-based deformation strain imaging using myocardial tagging and strain encoding. *Magnetic Resonance in Medicine*. 2021;85(1):357-368. doi:10.1002/MRM.28437

53. Vo HQ, Marwick TH, Negishi K. MRI-Derived Myocardial Strain Measures in Normal Subjects. *JACC Cardiovascular imaging*. 2018;11(2 Pt 1):196-205. doi:10.1016/J.JCMG.2016.12.025

54. Bucius P, Erley J, Tanacli R, Zieschang V, Giusca S, Korosoglou G, Steen H, Stehning C, Pieske B, Pieske-Kraigher E, Schuster A, Lapinskas T, Kelle S. Comparison of feature tracking, fast-SENC, and myocardial tagging for global and segmental left ventricular strain. *ESC heart failure*. 2020;7(2):523-532. doi:10.1002/EHF2.12576

55. Wu L, Germans T, Güçlü A, Heymans MW, Allaart CP, van Rossum AC. Feature tracking compared with tissue tagging measurements of segmental strain by cardiovascular magnetic resonance. *Journal of Cardiovascular Magnetic Resonance*. 2014;16(1):1-11. doi:10.1186/1532-429X-16-10/TABLES/6

56. Retson TA, Besser AH, Sall S, Golden D, Hsiao A. Machine Learning and Deep Neural Networks in Thoracic and Cardiovascular Imaging. *Journal of Thoracic Imaging*. 2019;34(3):192-201. doi:10.1097/RTI.0000000000000385

57. Lecun Y, Bengio Y, Hinton G. Deep learning. *Nature 2015 521:7553*. 2015;521(7553):436-444. doi:10.1038/nature14539

58. Krizhevsky A, Sutskever I, Hinton GE. ImageNet Classification with Deep Convolutional Neural Networks. Accessed February 16, 2022. http://code.google.com/p/cuda-convnet/

59. Zhou DX. Universality of Deep Convolutional Neural Networks. Published online 2018.

60. Gelenbe E, Mao ZH, Li Y da. Function approximation with spiked random networks. *IEEE Transactions on Neural Networks*. 1999;10(1):3-9. doi:10.1109/72.737488

61. Ronneberger O, Fischer P, Brox T. U-Net: Convolutional Networks for Biomedical Image Segmentation. In: *Medical Image Computing and Computer-Assisted Intervention – MICCAI 2015. MICCAI 2015. Lecture Notes in Computer Science*. Vol 9351. ; 2015:234-241. doi:10.1007/978-3-319-24574-4_28

62. Blansit K, Retson T, Masutani E, Bahrami N, Hsiao A. Deep Learning–based Prescription of Cardiac MRI Planes. *Radiology: Artificial Intelligence*. 2019;1(6):e180069. doi:10.1148/ryai.2019180069

63. LeCun Y, Bottou L, Bengio Y, Haffner P. Gradient-based learning applied to document recognition. *Proceedings of the IEEE*. 1998;86(11):2278-2323. doi:10.1109/5.726791

64. Hurt B, Rubel MA, Masutani EM, Jacobs K, Hahn L, Horowitz M, Kligerman S, Hsiao A. Radiologist-supervised Transfer Learning: Improving Radiographic Localization of Pneumonia and Prognostication of Patients With COVID-19. *Journal of thoracic imaging*. Published online 2021. doi:10.1097/RTI.0000000000000618

65. Wehbe RM, Sheng J, Dutta S, Chai S, Dravid A, Barutcu S, Wu Y, Cantrell DR, Xiao N, Allen BD, MacNealy GA, Savas H, Agrawal R, Parekh N, Katsaggelos AK. DeepCOVID-XR: An artificial intelligence algorithm to detect COVID-19 on chest radiographs trained and tested on a large U.S. Clinical data set. *Radiology*. 2021;299(1):E167-E176. doi:10.1148/RADIOL.2020203511/ASSET/IMAGES/LARGE/RADIOL.2020203511.FIG6C.JPEG

66. Xue H, Artico J, Fontana M, Moon JC, Davies RH, Kellman P. Landmark detection in cardiac MRI by using a convolutional neural network. *Radiology: Artificial Intelligence*. 2021;3(5). doi:10.1148/RYAI.2021200197/ASSET/IMAGES/LARGE/RYAI.2021200197.FIG5.JPEG

67. Chen Z, Rigolli M, Vigneault DM, Kligerman S, Hahn L, Narezkina A, Craine A, Lowe K, Contijoch F. Automated cardiac volume assessment and cardiac long- and short-axis imaging plane prediction from electrocardiogram-gated computed tomography volumes enabled by deep learning. *European Heart Journal - Digital Health*. 2021;2(2):311-322. doi:10.1093/EHJDH/ZTAB033

68. Ashikaga H, Estner HL, Herzka DA, Mcveigh ER, Halperin HR. Quantitative Assessment of Single-Image Super-Resolution in Myocardial Scar Imaging. *IEEE journal of translational engineering in health and medicine*. 2014;2. doi:10.1109/JTEHM.2014.2303806

69. Bernstein MA, Fain SB, Riederer SJ. Effect of windowing and zero-filled reconstruction of MRI data on spatial resolution and acquisition strategy. *Journal of Magnetic Resonance Imaging*. 2001;14(3):270-280. doi:10.1002/jmri.1183

70. Semmlow JL, Griffel B. *Biosignal and Medical Image Processing*. 3rd ed. CRC Press; 2014.

71. van Reeth E, Tham IWK, Tan CH, Poh CL. Super-resolution in magnetic resonance imaging: A review. *Concepts in Magnetic Resonance Part A*. 2012;40A(6):306-325. doi:10.1002/cmr.a.21249

72. Irani M, Peleg S. Motion Analysis for Image Enhancement: Resolution, Occlusion, and Transparency. *Journal of Visual Communication and Image Representation*. 1993;4(4):324-335. doi:10.1006/JVCI.1993.1030

73. Greenspan H. Super-Resolution in Medical Imaging. *The Computer Journal*. 2008;52(1):43-63. doi:10.1093/comjnl/bxm075

74. Scheffler K. Superresolution in MRI? *Magnetic Resonance in Medicine*. 2002;48(2):408-408. doi:10.1002/mrm.10203

75. Greenspan H, Oz G, Kiryati N, Peled S. MRI inter-slice reconstruction using super-resolution. *Magnetic Resonance Imaging*. 2002;20(5):437-446. doi:10.1016/S0730-725X(02)00511-8

76. Uecker M, Sumpf TJ, Frahm J. Reply to: MRI resolution enhancement: How useful are shifted images obtained by changing the demodulation frequency? *Magnetic Resonance in Medicine*. 2011;66(6):1511-1512. doi:10.1002/mrm.22989

77. Peled S, Yeshurun Y. Superresolution in MRI: Application to human white matter fiber tract visualization by diffusion tensor imaging. *Magnetic Resonance in Medicine*. 2001;45(1):29-35. doi:10.1002/1522-2594(200101)45:1<29::AID-MRM1005>3.0.CO;2-Z

78. Tieng QM, Cowin GJ, Reutens DC, Galloway GJ, Vegh V. MRI resolution enhancement: How useful are shifted images obtained by changing the demodulation frequency? *Magnetic Resonance in Medicine*. 2011;65(3):664-672. doi:10.1002/mrm.22653

79. McCann MT, Jin KH, Unser M. Convolutional Neural Networks for Inverse Problems in Imaging: A Review. *IEEE Signal Processing Magazine*. 2017;34(6):85-95. doi:10.1109/MSP.2017.2739299

80. Bahrami N, Retson T, Blansit K, Wang K, Hsiao A. Automated selection of myocardial inversion time with a convolutional neural network: Spatial temporal ensemble myocardium inversion network (STEMI-NET). *Magnetic Resonance in Medicine*. 2019;81(5):3283-3291. doi:10.1002/mrm.27680

81. Wang K, Mamidipalli A, Retson T, Bahrami N, Hasenstab K, Blansit K, Bass E, Delgado T, Cunha G, Middleton MS, Loomba R, Neuschwander-Tetri BA, Sirlin CB, Hsiao A. Automated CT and MRI Liver Segmentation and Biometry Using a Generalized Convolutional Neural Network. *Radiology: Artificial Intelligence*. 2019;1(2):180022. doi:10.1148/ryai.2019180022

82. Chartrand G, Cheng PM, Vorontsov E, Drozdzal M, Turcotte S, Pal CJ, Kadoury S, Tang A. Deep Learning: A Primer for Radiologists. *RadioGraphics*. 2017;37(7):2113-2131. doi:10.1148/rg.2017170077

83. Zhu G, Jiang B, Tong L, Xie Y, Zaharchuk G, Wintermark M. Applications of deep learning to neuro-imaging techniques. *Frontiers in Neurology*. 2019;10(AUG). doi:10.3389/fneur.2019.00869

84. Dong C, Loy CC, He K, Tang X. Image Super-Resolution Using Deep Convolutional Networks. *IEEE Transactions on Pattern Analysis and Machine Intelligence*. 2016;38(2):295-307. doi:10.1109/TPAMI.2015.2439281

85. Zhao H, Gallo O, Frosio I, Kautz J. Loss Functions for Image Restoration With Neural Networks. *IEEE Transactions on Computational Imaging*. 2017;3(1):47-57. doi:10.1109/TCI.2016.2644865

86. Wang Z, Simoncelli EP, Bovik AC. Multiscale structural similarity for image quality assessment. In: *The Thrity-Seventh Asilomar Conference on Signals, Systems & Computers, 2003*. IEEE; :1398-1402. doi:10.1109/ACSSC.2003.1292216

87. Wang Z, Bovik AC, Rahim Sheikh H, Simoncelli EP. Image Quality Assessment: From Error Visibility to Structural Similarity. *IEEE TRANSACTIONS ON IMAGE PROCESSING*. 2004;13(4). doi:10.1109/TIP.2003.819861

88. Deshmane A, Gulani V, Griswold MA, Seiberlich N. Parallel MR imaging. *Journal of Magnetic Resonance Imaging*. 2012;36(1):55-72. doi:10.1002/jmri.23639

89. Lustig M, Donoho D, Pauly JM. Sparse MRI: The application of compressed sensing for rapid MR imaging. *Magnetic Resonance in Medicine*. 2007;58(6):1182-1195. doi:10.1002/mrm.21391

90. Dyverfeldt P, Bissell M, Barker AJ, Bolger AF, Carlhäll CJ, Ebbers T, Francios CJ, Frydrychowicz A, Geiger J, Giese D, Hope MD, Kilner PJ, Kozerke S, Myerson S, Neubauer S, Wieben O, Markl M. 4D flow cardiovascular magnetic resonance consensus statement. *Journal of Cardiovascular Magnetic Resonance*. 2015;17(1):72. doi:10.1186/s12968-015-0174-5

91. Rafailidis V, Fang C, Yusuf GT, Huang DY, Sidhu PS. Contrast-enhanced ultrasound (CEUS) of the abdominal vasculature. *Abdominal radiology (New York)*. 2018;43(4):934-947. doi:10.1007/S00261-017-1329-7

92. Nicolau C, Ripollés T. Contrast-enhanced ultrasound in abdominal imaging. *Abdominal Imaging 2011 37:1*. 2011;37(1):1-19. doi:10.1007/S00261-011-9796-8

93. Brkic A, Terslev L, Møller Døhn U, Torp-Pedersen S, Schmidt WA, Diamantopoulos AP. Clinical Applicability of Ultrasound in Systemic Large Vessel Vasculitides. *Arthritis & Rheumatology*. 2019;71(11):1780-1787. doi:10.1002/ART.41039

94. Li KCP, Whitney WS, McDonnell CH, Fredrickson JO, Pelc NJ, Dalman RL, Jeffrey RB. Chronic mesenteric ischemia: evaluation with phase-contrast cine MR imaging. *https://doi.org/101148/radiology19018259400*. 1994;190(1):175-179. doi:10.1148/RADIOLOGY.190.1.8259400

95. Pelc NJ, Herfkens RJ, Shimakawa A, Enzmann DR. Phase contrast cine magnetic resonance imaging. *Magnetic Resonance Quarterly*. 1991;7(4):229-254. Accessed February 19, 2022. https://europepmc.org/article/med/1790111

96. Roldán-Alzate A, Francois CJ, Wieben O, Reeder SB. Emerging Applications of Abdominal 4D Flow MRI. *AJR American journal of roentgenology*. 2016;207(1):58. doi:10.2214/AJR.15.15995

97. Markl M, Frydrychowicz A, Kozerke S, Hope M, Wieben O. 4D flow MRI. *Journal of Magnetic Resonance Imaging*. 2012;36(5):spcone-spcone. doi:10.1002/JMRI.23556

98. Chernobelsky A, Shubayev O, Comeau CR, Wolff SD. Baseline correction of phase contrast images improves quantification of blood flow in the great vessels. *Journal of Cardiovascular Magnetic Resonance*. 2007;9(4):681-685. doi:10.1080/10976640601187588

99. Gatehouse PD, Rolf MP, Bloch KM, Graves MJ, Kilner PJ, Firmin DN, Hofman MBM. A multi-center inter-manufacturer study of the temporal stability of phase-contrast velocity mapping background offset errors. *Journal of Cardiovascular Magnetic Resonance*. 2012;14(1):1-7. doi:10.1186/1532-429X-14-72/FIGURES/5

100. Walker PG, Cranney GB, Scheidegger MB, Waseleski G, Pohost GM, Yoganathan AP. Semiautomated method for noise reduction and background phase error correction in MR phase velocity data. *Journal of Magnetic Resonance Imaging*. 1993;3(3):521-530. doi:10.1002/JMRI.1880030315

101. Soffer S, Ben-Cohen A, Shimon O, Amitai MM, Greenspan H, Klang E. Convolutional Neural Networks for Radiologic Images: A Radiologist's Guide. *Radiology*. 2019;290(3):590-606. doi:10.1148/RADIOL.2018180547/ASSET/IMAGES/LARGE/RADIOL.2018180547.TBL5.JPEG

102. Cheng JY, Zhang T, Ruangwattanapaisarn N, Alley MT, Uecker M, Pauly JM, Lustig M, Vasanawala SS. Free-breathing pediatric MRI with nonrigid motion correction

and acceleration. *Journal of Magnetic Resonance Imaging*. 2015;42(2):407-420. doi:10.1002/JMRI.24785

103. Cheng JY, Hanneman K, Zhang T, Alley MT, Lai P, Tamir JI, Uecker M, Pauly JM, Lustig M, Vasanawala SS. Comprehensive motion-compensated highly accelerated 4D flow MRI with ferumoxytol enhancement for pediatric congenital heart disease. *Journal of Magnetic Resonance Imaging*. 2016;43(6):1355-1368. doi:10.1002/JMRI.25106

104. Winkelmann S, Schaeffter T, Koehler T, Eggers H, Doessel O. An optimal radial profile order based on the golden ratio for time-resolved MRI. *IEEE Transactions on Medical Imaging*. 2007;26(1):68-76. doi:10.1109/TMI.2006.885337

105. Cheng JY, Alley MT, Cunningham CH, Vasanawala SS, Pauly JM, Lustig M. Nonrigid motion correction in 3D using autofocusing withlocalized linear translations. *Magnetic Resonance in Medicine*. 2012;68(6):1785-1797. doi:10.1002/MRM.24189

106. Lim TS, Loh WY. A comparison of tests of equality of variances. *Computational Statistics & Data Analysis*. 1996;22(3):287-301. doi:10.1016/0167-9473(95)00054-2

107. Shrout PE, Fleiss JL. Intraclass correlations: Uses in assessing rater reliability. *Psychological Bulletin*. 1979;86(2):420-428. doi:10.1037/0033-2909.86.2.420

108. Saranathan M, Rettmann DW, Hargreaves BA, Clarke SE, Vasanawala SS. DIfferential subsampling with cartesian ordering (DISCO): A high spatio-temporal resolution dixon imaging sequence for multiphasic contrast enhanced abdominal imaging. *Journal of Magnetic Resonance Imaging*. 2012;35(6):1484-1492. doi:10.1002/JMRI.23602

109. Keller EJ, Collins JD, Rigsby C, Carr JC, Markl M, Schnell S. Superior Abdominal 4D Flow MRI Data Consistency with Adjusted Preprocessing Workflow and Noncontrast Acquisitions. *Academic Radiology*. 2017;24(3):350-358. doi:10.1016/J.ACRA.2016.10.007

110. Pennell DJ. Cardiovascular magnetic resonance. *Circulation*. 2010;121(5):692-705. doi:10.1161/CIRCULATIONAHA.108.811547

111. Grothues F, Smith GC, Moon JCC, Bellenger NG, Collins P, Klein HU, Pennell DJ. Comparison of interstudy reproducibility of cardiovascular magnetic resonance with two-dimensional echocardiography in normal subjects and in patients with heart failure or left ventricular hypertrophy. *American Journal of Cardiology*. 2002;90(1):29-34. doi:10.1016/S0002-9149(02)02381-0

112. Markl M, Chan FP, Alley MT, Wedding KL, Draney MT, Elkins CJ, Parker DW, Wicker R, Taylor CA, Herfkens RJ, Pelc NJ. Time-resolved three-dimensional

phase-contrast MRI. *J Magn Reson Imaging*. 2003;17(4):499-506. doi:10.1002/jmri.10272

113. Elbaz MSM, Scott MB, Barker AJ, McCarthy P, Malaisrie C, Collins JD, Bonow RO, Carr J, Markl M. Four-dimensional Virtual Catheter: Noninvasive Assessment of Intra-aortic Hemodynamics in Bicuspid Aortic Valve Disease. *Radiology*. 2019;293(3):541-550. doi:10.1148/radiol.2019190411

114. Bogaert J, Olivotto I. MR imaging in hypertrophic cardiomyopathy: From magnet to bedside. *Radiology*. 2014;273(2):329-348. doi:10.1148/radiol.14131626

115. Katus HA, Frey N, Luedde M, Katus HA. Mechanisms of disease: hypertrophic cardiomyopathy. *Nature Publishing Group*. 2011;9:91-100. doi:10.1038/nrcardio.2011.159

116. Maron BJ. Hypertrophic cardiomyopathy: A systematic review. *Journal of the American Medical Association*. 2002;287(10):1308-1320. doi:10.1001/jama.287.10.1308

117. Gersh BJ, Maron BJ, Bonow RO, Dearani JA, Fifer MA, Link MS, Naidu SS, Nishimura RA, Ommen SR, Rakowski H, Seidman CE, Towbin JA, Udelson JE, Yancy CW; American College of Cardiology Foundation/American Heart Association Task Force on Practice Guidelines; American Association for Thoracic Surgery; American Society of Echocardiography; American Society of Nuclear Cardiology; Heart Failure Society of America; Heart Rhythm Society; Society for Cardiovascular Angiography and Interventions; Society of Thoracic Surgeons. 2011 ACCF/AHA guideline for the diagnosis and treatment of hypertrophic cardiomyopathy: executive summary: a report of the American College of Cardiology Foundation/American Heart Association Task Force on Practice Guidelines. *Circulation*. 2011 Dec 13;124(24):2761-96. doi: 10.1161/CIR.0b013e318223e230.

118. Otto CM, Prendergast B. Aortic-Valve Stenosis — From Patients at Risk to Severe Valve Obstruction. *New England Journal of Medicine*. 2014;371(8):744-756. doi:10.1056/nejmra1313875

119. Leiner T, Rueckert D, Suinesiaputra A, Baeßler B, Nezafat R, Išgum I, Young AA. Machine learning in cardiovascular magnetic resonance: basic concepts and applications. *Journal of Cardiovascular Magnetic Resonance 2019 21:1*. 2019;21(1):1-14. doi:10.1186/S12968-019-0575-Y

120. Juluru K, Shih HH, Keshava Murthy KN, Elnajjar P, El-Rowmeim A, Roth C, Genereaux B, Fox J, Siegel E, Rubin DL. Integrating Al Algorithms into the Clinical Workflow. Radiol Artif Intell. 2021 Aug 4;3(6):e210013. doi: 10.1148/ryai.2021210013.

121. Bartoli A, Fournel J, Bentatou Z, Habib G, Lalande A, Bernard M, Boussel L, Pontana F, Dacher JN, Ghattas B, Jacquier A. Deep Learning–based Automated

Segmentation of Left Ventricular Trabeculations and Myocardium on Cardiac MR Images: A Feasibility Study. *Radiology: Artificial Intelligence*. 2021;3(1):e200021. doi:10.1148/ryai.2020200021

122. Xue H, Artico J, Fontana M, Moon JC, Davies RH, Kellman P. Landmark Detection in Cardiac MRI by Using a Convolutional Neural Network. *Radiol Artif Intell.* 2021 Jul 14;3(5):e200197. doi: 10.1148/ryai.2021200197.

123. Ouyang D, He B, Ghorbani A, Yuan N, Ebinger J, Langlotz CP, Heidenreich PA, Harrington RA, Liang DH, Ashley EA, Zou JY. Video-based AI for beat-to-beat assessment of cardiac function. *Nature*. 2020;580(7802):252-256. doi:10.1038/s41586-020-2145-8

124. Ghorbani A, Ouyang D, Abid A, He B, Chen JH, Harrington RA, Liang DH, Ashley EA, Zou JY. Deep learning interpretation of echocardiograms. *npj Digital Medicine*. 2020;3(1):1-10. doi:10.1038/s41746-019-0216-8

125. Masutani EM, Bahrami N, Hsiao A. Deep Learning Single-Frame and Multiframe Super-Resolution for Cardiac MRI. *Radiology*. 2020;295(3):552-561. doi:10.1148/radiol.2020192173

126. Lagemann C, Lagemann K, Mukherjee S, Schröder W. Deep recurrent optical flow learning for particle image velocimetry data. *Nature Machine Intelligence 2021 3:7*. 2021;3(7):641-651. doi:10.1038/s42256-021-00369-0

127. Cheng JY, Hanneman K, Zhang T, Alley MT, Lai P, Tamir JI, Uecker M, Pauly JM, Lustig M, Vasanawala SS. Comprehensive motion-compensated highly accelerated 4D flow MRI with ferumoxytol enhancement for pediatric congenital heart disease. *Journal of Magnetic Resonance Imaging*. 2016;43(6):1355-1368. doi:10.1002/jmri.25106

128. Shi W, Caballero J, Huszar F, Totz J, Aitken AP, Bishop R, Rueckert D, Wang Z. Real-Time Single Image and Video Super-Resolution Using an Efficient Sub-Pixel Convolutional Neural Network. In: *Proceedings of the IEEE Conference on Computer Vision and Pattern Recognition (CVPR)*. ; 2016:1874-1883.

129. Kim T, Hedayat M, Vaitkus V v., Belohlavek M, Krishnamurthy V, Borazjani I. Automatic segmentation of the left ventricle in echocardiographic images using convolutional neural networks. *Quantitative Imaging in Medicine and Surgery*. 2021;11(5):1763781-1761781. doi:10.21037/QIMS-20-745

130. Saber NR, Gosman AD, Wood NB, Kilner PJ, Charrier CL, Firmin DN. Computational flow modeling of the left ventricle based on in vivo MRI data: Initial experience. *Annals of Biomedical Engineering*. 2001;29(4):275-283. doi:10.1114/1.1359452

131. Lantz J, Gupta V, Henriksson L, Karlsson M, Persson A, Carlhäll CJ, Ebbers T. Intracardiac flow at 4D CT: Comparison with 4D flow MRI. *Radiology*. 2018;289(1):51-58. doi:10.1148/radiol.2018173017

132. Hurt B, Yen A, Kligerman S, Hsiao A. Augmenting Interpretation of Chest Radiographs With Deep Learning Probability Maps. *Journal of Thoracic Imaging*. 2020;35(5):285-293. doi:10.1097/RTI.0000000000000505

133. Hu J, Shen L, Sun G. Squeeze-and-Excitation Networks. In: *Proceedings of the IEEE Conference on Computer Vision and Pattern Recognition (CVPR)*. ; 2018:7132-7141.

134. Penrose R. A generalized inverse for matrices. *Mathematical Proceedings of the Cambridge Philosophical Society*. 1955;51(3):406-413. doi:10.1017/S0305004100030401

135. Rose MJ, Jarvis K, Chowdhary V, Barker AJ, Allen BD, Robinson JD, Markl M, Rigsby CK, Schnell S. Efficient method for volumetric assessment of peak blood flow velocity using 4D flow MRI. *Journal of Magnetic Resonance Imaging*. 2016;44(6):1673-1682. doi:10.1002/JMRI.25305

136. Malayeri AA, Johnson WC, Macedo R, Bathon J, Lima JAC, Bluemke DA. Cardiac cine MRI: Quantification of the relationship between fast gradient echo and steady-state free precession for determination of myocardial mass and volumes. *Journal of Magnetic Resonance Imaging*. 2008;28(1):60-66. doi:10.1002/JMRI.21405

137. Jahnke C, Nagel E, Gebker R, Kokocinski T, Kelle S, Manka R, Fleck E, Paetsch I. Prognostic value of cardiac magnetic resonance stress tests: Adenosine stress perfusion and dobutamine stress wall motion imaging. *Circulation*. 2007;115(13):1769-1776. doi:10.1161/CIRCULATIONAHA.106.652016

138. Roditi GH, Hartnell GG, Cohen MC. MRI Changes in Myocarditis — Evaluation with Spin Echo, Cine MR Angiography and Contrast Enhanced Spin Echo Imaging. *Clinical Radiology*. 2000;55(10):752-758. doi:10.1053/CRAD.2000.0519

139. Gandjbakhch E, Redheuil A, Pousset F, Charron P, Frank R. Clinical Diagnosis, Imaging, and Genetics of Arrhythmogenic Right Ventricular Cardiomyopathy/Dysplasia: JACC State-of-the-Art Review. *Journal of the American College of Cardiology*. 2018;72(7):784-804. doi:10.1016/J.JACC.2018.05.065

140. Zerhouni EA, Parish DM, Rogers WJ, Yang A, Shapiro EP. Human heart: Tagging with MR imaging - A new method for noninvasive assessment of myocardial motion. *Radiology*. 1988;169(1):59-63. doi:10.1148/radiology.169.1.3420283

141. Auger DA, Zhong X, Epstein FH, Spottiswoode BS. Mapping right ventricular myocardial mechanics using 3D cine DENSE cardiovascular magnetic resonance.

Journal of Cardiovascular Magnetic Resonance. 2012;14(1):1-9. doi:10.1186/1532-429X-14-4

142. Korosoglou G, Gitsioudis G, Voss A, Lehrke S, Riedle N, Buss SJ, Zugck C, Giannitsis E, Osman NF, Katus HA. Strain-encoded cardiac magnetic resonance during high-dose dobutamine stress testing for the estimation of cardiac outcomes: Comparison to Clinical Parameters and Conventional Wall Motion Readings. *Journal of the American College of Cardiology*. 2011;58(11):1140-1149. doi:10.1016/j.jacc.2011.03.063

143. Osman NF, Kerwin WS, McVeigh ER, Prince JL. Cardiac Motion Tracking Using CINE Harmonic Phase (HARP) Magnetic Resonance Imaging. *Magnetic resonance in medicine : official journal of the Society of Magnetic Resonance in Medicine / Society of Magnetic Resonance in Medicine*. 1999;42(6):1048. doi:10.1002/(SICI)1522-2594(199912)42:6<1048::AID-MRM9>3.0.CO;2-M

144. Ruh A, Sarnari R, Berhane H, Sidoryk K, Lin K, Dolan R, Li A, Rose MJ, Robinson JD, Carr JC, Rigsby CK, Markl M. Impact of age and cardiac disease on regional left and right ventricular myocardial motion in healthy controls and patients with repaired tetralogy of fallot. *International Journal of Cardiovascular Imaging*. 2019;35(6):1119-1132. doi:10.1007/s10554-019-01544-6

145. Arai AE, Gaither CC, Epstein FH, Balaban RS, Wolff SD. Myocardial velocity gradient imaging by phase contrast MRI with application to regional function in myocardial ischemia. *Magnetic Resonance in Medicine*. 1999;42(1):98-109. doi:10.1002/(SICI)1522-2594(199907)42:1<98::AID-MRM14>3.0.CO;2-H

146. Mirea O, Pagourelias ED, Duchenne J, Bogaert J, Thomas JD, Badano LP, Voigt JU; EACVI-ASE-Industry Standardization Task Force. Intervendor Differences in the Accuracy of Detecting Regional Functional Abnormalities: A Report From the EACVI-ASE Strain Standardization Task Force. *JACC Cardiovasc Imaging*. 2018 Jan;11(1):25-34. doi: 10.1016/j.jcmg.2017.02.014.

147. Popović ZB, Benejam C, Bian J, Mal N, Drinko J, Lee K, Forudi F, Reeg R, Greenberg NL, Thomas JD, Penn MS. Speckle-tracking echocardiography correctly identifies segmental left ventricular dysfunction induced by scarring in a rat model of myocardial infarction. *American Journal of Physiology - Heart and Circulatory Physiology*. 2007;292(6):2809-2816. doi:10.1152/ajpheart.01176.2006

148. Roes SD, Mollema SA, Lamb HJ, van der Wall EE, de Roos A, Bax JJ. Validation of Echocardiographic Two-Dimensional Speckle Tracking Longitudinal Strain Imaging for Viability Assessment in Patients With Chronic Ischemic Left Ventricular Dysfunction and Comparison With Contrast-Enhanced Magnetic Resonance Imaging. *American Journal of Cardiology*. 2009;104(3):312-317. doi:10.1016/j.amjcard.2009.03.040

149. Vo HQ, Marwick TH, Negishi K. MRI-Derived Myocardial Strain Measures in Normal Subjects. *JACC: Cardiovascular Imaging*. 2018;11(2P1):196-205. doi:10.1016/J.JCMG.2016.12.025

150. Bucius P, Erley J, Tanacli R, Zieschang V, Giusca S, Korosoglou G, Steen H, Stehning C, Pieske B, Pieske-Kraigher E, Schuster A, Lapinskas T, Kelle S. Comparison of feature tracking, fast-SENC, and myocardial tagging for global and segmental left ventricular strain. *ESC Heart Failure*. 2020;7(2):523-532. doi:10.1002/EHF2.12576

151. Wu L, Germans T, Güçlü A, Heymans MW, Allaart CP, van Rossum AC. Feature tracking compared with tissue tagging measurements of segmental strain by cardiovascular magnetic resonance. *Journal of Cardiovascular Magnetic Resonance*. 2014;16(1):1-11. doi:10.1186/1532-429X-16-10/TABLES/6

152. Fries JA, Varma P, Chen VS, Xiao K, Tejeda H, Saha P, Dunnmon J, Chubb H, Maskatia S, Fiterau M, Delp S, Ashley E, Ré C, Priest JR. Weakly supervised classification of aortic valve malformations using unlabeled cardiac MRI sequences. *Nature Communications 2019 10:1*. 2019;10(1):1-10. doi:10.1038/s41467-019-11012-3

153. Zotti C, Luo Z, Lalande A, Jodoin PM. Convolutional Neural Network with Shape Prior Applied to Cardiac MRI Segmentation. *IEEE Journal of Biomedical and Health Informatics*. 2019;23(3):1119-1128. doi:10.1109/JBHI.2018.2865450

154. Lieman-Sifry J, Le M, Lau F, Sall S, Golden D. FastVentricle: Cardiac Segmentation with ENet. *Lecture Notes in Computer Science (including subseries Lecture Notes in Artificial Intelligence and Lecture Notes in Bioinformatics)*. 2017;10263 LNCS:127-138. doi:10.1007/978-3-319-59448-4_13

155. You S, Masutani EM, Alley MT, Vasanawala SS, Taub PR, Liau J, Roberts AC, Hsiao A. Deep Learning Automated Background Phase Error Correction for Abdominopelvic 4D Flow MRI. *https://doi.org/101148/radiol2021211270*. Published online November 30, 2021. doi:10.1148/RADIOL.2021211270

156. Ghadimi S, Auger DA, Feng X, Sun C, Meyer CH, Bilchick KC, Cao JJ, Scott AD, Oshinski JN, Ennis DB, Epstein FH. Fully-automated global and segmental strain analysis of DENSE cardiovascular magnetic resonance using deep learning for segmentation and phase unwrapping. *Journal of Cardiovascular Magnetic Resonance*. 2021;23(1):1-13. doi:10.1186/S12968-021-00712-9/TABLES/3

157. Ferdian E, Suinesiaputra A, Fung K, Aung N, Lukaschuk E, Barutcu A, Maclean E, Paiva J, Piechnik SK, Neubauer S, Petersen SE, Young AA. Fully automated myocardial strain estimation from cardiovascular MRI–Tagged images using a deep learning framework in the UK biobank. *Radiology: Cardiothoracic Imaging*. 2020;2(1).

doi:10.1148/RYCT.2020190032/ASSET/IMAGES/LARGE/RYCT.2020190032.TBL3.JPEG

158. Koo TK, Li MY. A Guideline of Selecting and Reporting Intraclass Correlation Coefficients for Reliability Research. *Journal of Chiropractic Medicine*. 2016;15(2):155. doi:10.1016/J.JCM.2016.02.012

159. Zou KH, Yu CR, Liu K, Carlsson MO, Cabrera J. Optimal Thresholds by Maximizing or Minimizing Various Metrics via ROC-Type Analysis. *Academic Radiology*. 2013;20:807-815. doi:10.1016/j.acra.2013.02.004

160. Landis JR, Koch GG. The Measurement of Observer Agreement for Categorical Data. *Biometrics*. 1977;33(1):159. doi:10.2307/2529310

161. Cicchetti D v. Guidelines, Criteria, and Rules of Thumb for Evaluating Normed and Standardized Assessment Instruments in Psychology. *Psychological Assessment*. 1994;(4):284-290.

162. Hoffmann R, von Bardeleben S, ten Cate F, Borges AC, Kasprzak J, Firschke C, Lafitte S, Al-Saadi N, Kuntz-Hehner S, Engelhardt M, Becher H, Vanoverschelde JL. Assessment of systolic left ventricular function: A multi-centre comparison of cineventriculography, cardiac magnetic resonance imaging, unenhanced and contrast-enhanced echocardiography. *European Heart Journal*. 2005;26(6):607-616. doi:10.1093/eurheartj/ehi083

163. Paetsch I, Jahnke C, Ferrari VA, Rademakers FE, Pellikka PA, Hundley WG, Poldermans D, Bax JJ, Wegscheider K, Fleck E, Nagel E. Determination of interobserver variability for identifying inducible left ventricular wall motion abnormalities during dobutamine stress magnetic resonance imaging. *European Heart Journal*. 2006;27(12):1459-1464. doi:10.1093/EURHEARTJ/EHI883

164. Schuster A, Stahnke VC, Unterberg-Buchwald C, Kowallick JT, Lamata P, Steinmetz M, Kutty S, Fasshauer M, Staab W, Sohns JM, Bigalke B, Ritter C, Hasenfuß G, Beerbaum P, Lotz J. Cardiovascular magnetic resonance feature-tracking assessment of myocardial mechanics: Intervendor agreement and considerations regarding reproducibility. *Clinical Radiology*. 2015;70(9):989. doi:10.1016/J.CRAD.2015.05.006

165. Morton G, Schuster A, Jogiya R, Kutty S, Beerbaum P, Nagel E. Inter-study reproducibility of cardiovascular magnetic resonance myocardial feature tracking. *Journal of Cardiovascular Magnetic Resonance*. 2012;14(1):1-8. doi:10.1186/1532-429X-14-43/TABLES/4

166. Mangion K, Burke NMM, McComb C, Carrick D, Woodward R, Berry C. Feature-tracking myocardial strain in healthy adults- a magnetic resonance study at 3.0 tesla. *Scientific Reports 2019 9:1*. 2019;9(1):1-9. doi:10.1038/s41598-019-39807-w

167. Ioffe S, Szegedy C. Batch Normalization: Accelerating Deep Network Training by Reducing Internal Covariate Shift.

168. Edvardsen T, Gerber BL, Garot J, Bluemke DA, Lima JAC, Smiseth OA. Quantitative assessment of intrinsic regional myocardial deformation by Doppler strain rate echocardiography in humans: Validation against three-dimensional tagged magnetic resonance imaging. *Circulation*. 2002;106(1):50-56. doi:10.1161/01.CIR.0000019907.77526.75

169. Cerqueira MD, Weissman NJ, Dilsizian V, Jacobs AK, Kaul S, Laskey WK, Pennell DJ, Rumberger JA, Ryan T, Verani MS. Standardized Myocardial Segmentation and Nomenclature for Tomographic Imaging of the Heart. *Circulation*. 2002;105(4):539-542. doi:10.1161/HC0402.102975

170. Bengs M, Gessert N, Schlaefer A. 4D spatio-temporal convolutional networks for object position estimation in OCT volumes. *Current Directions in Biomedical Engineering*. 2020;6(1). doi:10.1515/CDBME-2020-0001/MACHINEREADABLECITATION/RIS

171. Choy C, Gwak J, Savarese S. 4D Spatio-Temporal ConvNets: Minkowski Convolutional Neural Networks. Accessed February 16, 2022. https://github.com/StanfordVL/MinkowskiEngine

172. Ren M, Pokrovsky A, Yang B, Urtasun R. SBNet: Sparse Blocks Network for Fast Inference. Accessed February 16, 2022. https://github.com/uber/sbnet

173. Riegler G, Osman Ulusoy A, Geiger A. OctNet: Learning Deep 3D Representations at High Resolutions. Accessed February 16, 2022. https://3dwarehouse.sketchup.com

174. Gupta K, Sekhar N, Vigneault DM, Scott AR, Colvert B, Craine A, Raghavan A, Contijoch FJ. Octree Representation Improves Data Fidelity of Cardiac CT Images and Convolutional Neural Network Semantic Segmentation of Left Atrial and Ventricular Chambers. *Radiology Artificial intelligence*. 2021;3(6). doi:10.1148/RYAI.2021210036

175. Yuan W. Point Cloud Semantic Segmentation using Graph Convolutional Network. Accessed February 16, 2022. https://github.com/TonythePlaneswalker/pcd_seg.

176. Wang L, Huang Y, Hou Y, Zhang S, Shan J. Graph Attention Convolution for Point Cloud Semantic Segmentation.

177. Zhang J, Gajjala S, Agrawal P, Tison GH, Hallock LA, Beussink-Nelson L, Lassen MH, Fan E, Aras MA, Jordan CR, Fleischmann KE, Melisko M, Qasim A, Shah SJ, Bajcsy R, Deo RC. Fully automated echocardiogram interpretation in clinical practice: Feasibility and diagnostic accuracy. *Circulation*. 2018;138(16):1623-1635. doi:10.1161/CIRCULATIONAHA.118.034338

178. Leclerc S, Smistad E, Pedrosa J, Ostvik A, Cervenansky F, Espinosa F, Espeland T, Berg EAR, Jodoin PM, Grenier T, Lartizien C, Dhooge J, Lovstakken L, Bernard O. Deep Learning for Segmentation Using an Open Large-Scale Dataset in 2D Echocardiography. *IEEE transactions on medical imaging*. 2019;38(9):2198-2210. doi:10.1109/TMI.2019.2900516

179. Rehani MM, Berry M. Radiation doses in computed tomography : The increasing doses of radiation need to be controlled. *BMJ : British Medical Journal*. 2000;320(7235):593. doi:10.1136/BMJ.320.7235.593

180. Chun J, Lewis B, Ji Z, Shin JI, Park JC, Kim JS, Kim T. Evaluation of super-resolution on 50 pancreatic cancer patients with real-time cine MRI from 0.35T MRgRT. *Biomedical physics & engineering express*. 2021;7(5). doi:10.1088/2057-1976/AC1C51

181. van der Ven JPG, van den Bosch E, Bogers AJCC, Helbing WA. Current outcomes and treatment of tetralogy of Fallot. *F1000Research*. 2019;8. doi:10.12688/F1000RESEARCH.17174.1

182. Rizk J, Shehu N, Latus H, Martinoff S, Ewert P, Stern H, Meierhofer C. Magnetic Resonance Imaging Risk Factors for Ventricular Arrhythmias in Tetralogy of Fallot. *Pediatric cardiology*. 2020;41(5):862-868. doi:10.1007/S00246-020-02323-0

183. Bonello B, Kempny A, Uebing A, Li W, Kilner PJ, Diller GP, Pennell DJ, Shore DF, Ernst S, Gatzoulis MA, Babu-Narayan S v. Right atrial area and right ventricular outflow tract akinetic length predict sustained tachyarrhythmia in repaired tetralogy of Fallot. *International Journal of Cardiology*. 2013;168(4):3280. doi:10.1016/J.IJCARD.2013.04.048

184. Bertola B, Rondano E, Sulis M, Sarasso G, Piccinino C, Marti G, Devecchi P, Magnani A, Francalacci G, Marino PN. Cardiac Dyssynchrony Quantitated by Time-to-Peak or Temporal Uniformity of Strain at Longitudinal, Circumferential, and Radial Level: Implications for Resynchronization Therapy. *Journal of the American Society of Echocardiography*. 2009;22:665-671. doi:10.1016/j.echo.2009.03.010